

THERMAL TRANSPORT IN SYSTEMS
WITH HIERARCHICAL BIFURCATING
GEOMETRIES

by

DAVID CALAMAS

DR. JOHN BAKER, COMMITTEE CHAIR

DR. K. CLARK MIDKIFF
DR. PAUL S. RAY
DR. WILLARD C. SCHREIBER
DR. ROBERT P. TAYLOR

A DISSERTATION

Submitted in partial fulfillment of the requirements
for the degree of Doctor of Philosophy
in the Department of Mechanical Engineering
in the Graduate School of
The University of Alabama

TUSCALOOSA, ALABAMA

2013

Copyright David Calamas 2013

ALL RIGHTS RESERVED

ABSTRACT

This work investigates enhanced thermal transport through the use of hierarchical bifurcating geometries. An extensive literature review was performed regarding the use of biologically-inspired geometries to enhance heat transfer. If hierarchical bifurcating, or tree-like, geometries are considered, significant gains in the available surface area for heat transfer can be achieved as the geometric pattern is space-filling. As compared with parallel straight channel heat sinks, hierarchical bifurcating internal flow passages offer the advantages of reduced pressure drop as well as enhanced thermal mixing and increased surface temperature uniformity. In an initial investigation, the effect of scaling on flow networks with hierarchical bifurcating flow passages was examined. It was concluded microscale and mesoscale flow networks offer similar thermal performance while mesoscale flow networks have the additional advantage of reduced pressure drop.

When compared to traditional rectangular extended surfaces, fins with tree-like geometries offer an increase in surface area per mass. In a second investigation, the thermal performance of tree-like fins thermally radiating to free space was examined. The tree-like fins were found to be more effective than rectangular fins of equal mass, volume, and base area. Similarly, in a third investigation, the thermal performance of tree-like fins in a naturally convecting environment was examined. The tree-like fins were again found to be more effective at dissipating heat when compared with traditionally employed rectangular fins.

In the fourth investigation, hierarchical bifurcating flow passages were utilized in a single-fluid solid-liquid compact heat exchanger. System performance was experimentally

investigated and subsequently characterized in a manner similar to traditional compact heat exchangers. The experimental results were non-dimensionalized in order for system performance to be compared with traditional compact heat exchangers as a second fluid stream was absent. In the fifth and final investigation, the effect of bifurcation angle, porosity, and pore size on the fluid behavior through a porous disk with hierarchical bifurcating flow passages was computationally examined. It was concluded that varying bifurcation angles only impacted the flow behavior through, and pressure drop across, porous disks with tree-like flow passages at relatively low porosities and small pore sizes.

LIST OF ABBREVIATIONS AND SYMBOLS

A	area, m^2
Bi	Biot number
$c_{f,app}$	apparent friction factor
c_p	specific heat, J/kgK
d	hydraulic diameter, m
Eu	Euler number
F	view factor
f	friction factor
Gr	Grashof number
G	exchanger mass velocity, kg/sm^2
g	gravitational acceleration, m/s^2
H	height, m
h	heat transfer coefficient, W/m^2K
I_p^*	polar moment of inertia
i	inlet, incident
j	Colburn factor
k	branch level, thermal conductivity, W/mK
L	length, m
m	mass, kg

Nu	Nusselt number
N	Stark number
n	number of bifurcations per channel
Pr	Prandtl Number
p	pressure, Pa
Q	volumetric flow rate, m ³ /s, heat rate, W
q"	heat flux, W/m ²
Re	Reynolds number
St	Stanton number
T	temperature, K
u	velocity, m/s
V	volume, m ³
w	width, m
X	non-dimensional axial distance
x	axial distance
Z	ratio of fin base temperature to fin tip temperature
α	absorptivity, thermal diffusivity, m ² /s
β	diameter scale ratio, width scale ratio
Γ	ratio of fin width to fin thickness
Λ	area ratio
γ	length scale ratio
Δ	difference
δ	thickness

ε	effectiveness, emissivity, porosity
η	efficiency
θ	dimensionless temperature, bifurcation angle
Λ	surface area ratio
M	non-dimensional mass flow
ν	kinematic viscosity, m^2/s
ρ	density, kg/m^3 , reflectivity,
σ	Stefan-Boltzmann constant, $\text{W}/\text{m}^2\text{K}^4$
τ	shear stress, Pa
Ω	non-dimensional heat rate

Subscripts

b	base, bulk
c	characteristic
e	exit
f	face
i	inlet, local node identifier
n	normal
R	relative
r	thermally radiating
s	surface
T	total
t	tip
w	wall

∞ ambient

Materials

Al aluminum

Au gold

Ag silver

Cu copper

ACKNOWLEDGEMENTS

I would like to acknowledge the faculty of The University of Alabama for their assistance and support with research and education both in and out of the classroom. I would also like to thank Dr. John Baker for his dedicated support in research, education, and in personal matters. I would also like to thank the additional members of my dissertation committee: Dr. Clark Midkiff, Dr. Paul Ray, Dr. Will Schreiber, and Dr. Robert Taylor.

Portions of this work were funded by the National Science Foundation, GK-12 Grant 0742504 and the von Braun Center for Science and Innovation.

CONTENTS

ABSTRACT.....	ii
LIST OF ABBREVIATIONS AND SYMBOLS	iv
ACKNOWLEDGEMENTS	viii
LIST OF TABLES	xiii
LIST OF FIGURES	xiv
CHAPTER 1 – INTRODUCTION.....	1
Background.....	1
Motivation	15
Objectives	16
References	18
CHAPTER 2 – PERFORMANCE OF A BIOLOGICALLY-INSPIRED HEAT EXCHANGER WITH HIERARCHICAL BIFURCATING FLOW PASSAGES	28
Abstract.....	28
Introduction	28
Method of Analysis	34
Computational Model	36
Validation and Verification	38
Results and Discussions.....	44
Conclusions	61

Acknowledgments	62
References	63
CHAPTER 3 – BEHAVIOR OF THERMALLY RADIATING TREE-LIKE FINS	67
Abstract.....	67
Introduction	67
Tree-like Fins.....	72
Computational Model	74
Validation and Verification	76
Results and Discussions.....	78
Correlation	88
Conclusion	90
Acknowledgement	91
References	92
CHAPTER 4 – TREE-LIKE BRANCHING FINS: PERFORMANCE AND NATURAL CONVECTIVE HEAT TRANSER BEHAVIOR	96
Abstract.....	96
Introduction	96
Tree-Like Fins	100
Computational Model	102
Validation and Verification	104
Results and Discussions.....	106
Correlation	125
Conclusion	126
Acknowledgements	127

References	128
CHAPTER 5 – EXPERIMENTAL PERFORMANCE OF A SOLID HEAT EXCHANGER WITH TREE-LIKE FLOW PASSAGES	131
Abstract.....	131
Introduction	131
Experimental Investigation.....	135
Experimental Methods.....	139
Experimental Uncertainty.....	141
Calculations	142
Results and Discussion	143
Conclusions	149
Acknowledgements	150
References	151
CHAPTER 6 – FLOW BEHAVIOR AND PRESSURE DROP IN POROUS DISKS WITH BIFURCATING FLOW PASSAGES	154
Abstract.....	154
Introduction	154
Method of Analysis	159
Computational Methods	162
Validation and Verification	166
Results and Discussions.....	168
Conclusion.....	177
Acknowledgements	178
References	179

CHAPTER 7	183
CONCLUSION	183

LIST OF TABLES

Table 2.1. Channel Dimensions for Tree-Like	36
Table 2.2. Channel Dimensions for Zeroth-Order Branch	43
Table 2.3. Mass Flow Rate Ratios and Bulk Fluid Exit Temperatures.....	50
Table 2.4. Branch Level Performance Characteristics.....	59
Table 2.5. Flow Network Performance Characteristics	61
Table 3.2. Tree-Like And Rectangular Fin Dimensions and Mass Properties	74
Table 3.3. Validation Model Dimensions	77
Table 3.4. Fin Material Mass Properties.....	80
Table 3.5 Varying Fin Thickness Area and Mass Properties.....	82
Table 4.1. Tree-Like Fin Dimensions	101
Table 4.2. Tree-Like and Rectangular Fin Dimensions and Mass Properties	102
Table 4.3. Validation Model Dimensions	104
Table 4.4. Fin Material Mass Properties.....	108
Table 4.5. Varying Fin Thickness Area and Mass Properties.....	110
Table 4.6. Varying Length and Width Scale Ratios for the 90 ° Tree-Like Fin.....	111
Table 5.1. Heat Exchanger Tree-Like Disk Geometry	137
Table 6.1. Disk Geometry	160

LIST OF FIGURES

Figure 2.1. Nomenclature and Coordinate System for Branching Flow Networks	34
Figure 2.2. Three-Dimensional Computational Model Validation	39
Figure 2.3. Three-Dimensional Computational Model Validation with Experimental Results ...	42
Figure 2.4. Nomenclature and Coordinate System for Single Channel	42
Figure 2.5. Centerline Pressure Distributions	45
Figure 2.6. Centerline Euler Number Distributions	46
Figure 2.7. Centerline Reynolds Number Distributions	47
Figure 2.8. Mid-Depth Fluid Velocity Isolines at the First Bifurcation	48
Figure 2.9. Mid-Depth Fluid Velocity Isolines at the Second Bifurcation	48
Figure 2.10. Mass Flow Distribution at Outlets	49
Figure 2.11. Nomenclature for Wall Temperature Distributions	51
Figure 2.12. Wall Temperature Distributions along Path 1	51
Figure 2.13. Wall Temperature Distributions along Path 2	52
Figure 2.14. Inner and Bottom Wall Nusselt Number Distributions along Path 1	53
Figure 2.15. Inner and Bottom Wall Nusselt Number Distributions along Path 2	54
Figure 2.16. Flow Trajectories at the First Bifurcation	55
Figure 2.17. Flow Trajectories at the Second Bifurcation	55
Figure 2.18. Outer Wall Temperature Distributions along Path 1	56
Figure 2.19. Outer Wall Temperature Distributions along Path 2	56
Figure 2.20. Outer Wall Nusselt Number Distributions along Path 1	57

Figure 2.21. Outer Wall Nusselt Number Distributions along Path 2	57
Figure 2.22. Mid-Depth Fluid Temperature Isolines at the First Bifurcation.....	58
Figure 2.23. Mid-Depth Fluid Temperature Isolines at the Second Bifurcation	59
Figure 3.1. Tree-Fin Nomenclature and Coordinate system.....	72
Figure 3.2. 30, 60, and 90 ° Bifurcation Angle Tree-Like Fins.....	74
Figure 3.3. Computational Model Validation Nomenclature and Coordinate System	76
Figure 3.4. Computational Model Validation	78
Figure 3.5. Fin Effectiveness with Varying Heat Rate	79
Figure 3.6. Fin Effectiveness with Varying Material for the 90 ° Tree-Like Fin.....	81
Figure 3.7. Fin Effectiveness per unit Mass With Varying Material for the 90 ° Tree-Like fin ..	81
Figure 3.8. Fin Effectiveness with Varying Width-to-Thickness Ratio for the 90 ° Tree-Like Fin	82
Figure 3.9. Tree-Like Fin Temperature Isolines.....	83
Figure 3.10. Fin Efficiency with Varying Heat Rate	84
Figure 3.11. Fin Efficiency with Varying Material for the 90 ° Tree-Like Fin.....	84
Figure 3.12. Fin Efficiency with Varying Width-to-Thickness Ratio for the 90 ° Tree-Like Fin	85
Figure 3.13. Fin Base Temperatures with Varying Heat Rate	86
Figure 3.14. Fin Base Temperature for Varying Fin Material for the 90 ° Tree-Like Fin	87
Figure 3.15. Fin Base Temperature for Varying Width-to-Thickness Ratio for the 90 ° Tree-Like Fin	88
Figure 3.16. Tree-Like Fin Effectiveness Correlation	89
Figure 4.1. Tree-Fin Nomenclature and Coordinate System	101
Figure 4.2. 90, 60, and 30 ° Bifurcation Angle Tree-Like Fins.....	102
Figure 4.3. Computational Model Validation Nomenclature and Coordinate System	104
Figure 4.4. Computational Model Validation	106

Figure 4.5. Fin Effectiveness with Varying Heat Flux	107
Figure 4.6. Fin Effectiveness with Varying Material for the 90 ° Tree-Like Fin.....	108
Figure 4.7. Fin Effectiveness per Unit Mass with Varying Material for the 90 ° Tree-Like Fin	109
Figure 4.8. Fin Effectiveness with Varying Width-to-Thickness Ratio for the 90 ° Tree-Like Fin	110
Figure 4.9. Fin Effectiveness with Varying Scales for the 90 ° Tree-Like Fin	111
Figure 4.10. Varying Length Scale Ratio for the 90 ° Tree-Like Fin ($\beta = 2^{-1/2}$; $\gamma = 2^{-1/4}$, $\gamma = 2^{-1/3}$, $\gamma = 2^{-1/2}$, $\gamma = 2^{-2/3}$, and $\gamma = 2^{-3/4}$)	112
Figure 4.11. Varying Width Scale Ratio for the 90 ° Tree-Like Fin ($\gamma = 2^{-1/2}$; $\beta = 2^{-1/4}$, $\beta = 2^{-1/3}$, $\beta = 2^{-1/2}$, $\beta = 2^{-2/3}$, and $\beta = 2^{-3/4}$).....	112
Figure 4.12. Fin Effectiveness as a Function of Length Scale Ratio for the 90 ° Tree-Like Fin	113
Figure 4.13. Fin Effectiveness as a Function of Width Scale Ratio for the 90 ° Tree-Like Fin.	113
Figure 4.14. Fin Efficiency with Varying Heat Flux	114
Figure 4.15. Tree-Like Fin Solid Temperature Isolines as a Function of Bifurcation Angle.....	115
Figure 4.16. Tree-Like Fin Fluid Velocity Isolines as a Function of Bifurcation Angle	115
Figure 4.17. Fin Efficiency with Varying Material for the 90 ° Tree-Like Fin.....	116
Figure 4.18. Fin Efficiency with Varying Width-to-Thickness Ratio for the 90 ° Tree-Like Fin	117
Figure 4.19. Tree-Like Fin Fluid Velocity Isolines with Varying Width-to-Thickness Ratio ...	117
Figure 4.20. Fin Efficiency with Varying Scales for the 90 ° Tree-Like Fin	118
Figure 4.21 Scaled Tree-Like Fin Fluid Velocity Isolines	118
Figure 4.22. Fin Efficiency as a Function of Length Scale Ratio for The 90 ° Tree-Like Fin...	120
Figure 4.23. Fin Efficiency as a Function of Length Scale Ratio for the 90 ° Tree-Like Fin	120
Figure 4.24. Fin Base Temperatures with Varying Heat Flux	121
Figure 4.25. Fin Base Temperature for Varying Fin Material for the 90 ° Tree-Like Fin	122

Figure 4.26. Fin Base Temperature for Varying Width-to-Thickness Ratio for the 90 ° Tree-Like Fin	122
Figure 4.27. Fin Effectiveness with Varying Scales for the 90 ° Tree-Like Fin	123
Figure 4.28. Fin Base Temperature as a Function of Length Scale Ratio for the 90 ° Tree-Like Fin	124
Figure 4.29. Fin Efficiency as a Function of Width Scale Ratio for the 90 ° Tree-Like Fin.....	124
Figure 4.30. Tree-Like Fin Effectiveness Correlation	126
Figure 5.1. Single Tree-Like Disk	135
Figure 5.2. Nomenclature Describing Tree-Like Flow Passages	136
Figure 5.3. Exploded View of Heat Exchanger	137
Figure 5.4. Exploded View of Single Disk Enclosure	139
Figure 5.5. Experimental Schematic	139
Figure 5.6. Pressure Drop across Heat Exchanger (4 tree-like disks)	144
Figure 5.7. Pressure Drop across Single Tree-Like Disk.....	144
Figure 5.8. Heat Exchanger Euler Number (4 tree-like disks)	145
Figure 5.9. Single Tree-Like Disk Euler Number.....	146
Figure 5.10. Heat Exchanger Temperature Increase (4 tree-like disks)	147
Figure 5.11. Heat Exchanger Nusselt Number (4 tree-like disks)	147
Figure 5.12. Heat Exchanger Colburn Factor (4 tree-like disks).....	148
Figure 5.13. Heat Exchanger Friction Factor (4 tree-like disks)	149
Figure 6.1. Nomenclature and Coordinate System for Branching Flow Networks	160
Figure 6.2. 15, 30, 45, 60, 75, and 90 ° Porous Disks.	161
Figure 6.3. Computational Model Exploded View and Assembly	162
Figure 6.4. Computational Model Geometry Validation	166
Figure 6.5. Computational Model Porous Material Validation	167

Figure 6.6. Pressure Drop as a Function of Bifurcation Angle and Pore size ($\epsilon = 0.03$).....	169
Figure 6.7. Pressure Drop as a Function of Bifurcation Angle, and Pore Size ($\epsilon = 0.25$)	170
Figure 6.8. Pressure Drop as a Function of Flow Rate and Bifurcation Angle ($\epsilon = 0.5$, 40 PPI).....	170
Figure 6.9. Pressure Drop as a Function of Flow Rate and Pore Size ($\epsilon = 0.03$, 0.25, $\theta = 45^\circ$)	171
Figure 6.10. Pressure Drop as a Function of Flow Rate and Pore Size ($\epsilon = 0.5$, 75 $\theta = 45^\circ$)....	172
Figure 6.11. Pressure Drop as a Function of Flow Rate and Pore Size ($\epsilon = 0.97$, $\theta = 45^\circ$).....	173
Figure 6.12. Pressure Drop as a Function of Flow Rate and Porosity ($\theta = 45^\circ$, 40 PPI).....	174
Figure 6.13. Pressure Drop as a Function of Flow Rate and Porosity ($\theta = 45^\circ$, 20 PPI).....	174
Figure 6.14. Pressure Drop as a Function of Flow Rate and Porosity ($\theta = 45^\circ$, 10 PPI).....	175
Figure 6.15. Fluid Pressure Isolines for the 15 (left) and 90 (right) $^\circ$ Porous Disks ($\epsilon = 0.03$, 40 PPI, $Q = 3$ lpm)	176
Figure 6.16. Fluid Pressure Isolines for the 15 (left) and 90 (right) $^\circ$ Porous Disks ($\epsilon = 0.03$, 40 PPI, $Q = 3$ lpm)	177

CHAPTER 1

INTRODUCTION

Background

Biomimetics is the use of biologically-inspired solutions for engineering applications. In biological systems, hierarchical bifurcating flow passages produce space-filling flow networks, minimize flow resistance, and enhance surface area to volume ratios. These are all desirable characteristics for heat exchangers as well as biological systems. The terms “fractal-like,” and “tree-like” are often employed interchangeably to describe hierarchical bifurcating geometries. There have been numerous studies that have examined physical and mathematical explanations for these complex geometries found in nature [1.1, 1.2]. Mandelbrot [1.2] describes fractals as geometric patterns that fail to be described by classical geometry. Fractal geometries are self-similar as they can be divided into parts that are scaled copies of the whole. Fractal-like branching networks have identical bifurcations at all branch levels that results from fixed bifurcation angles as well as fixed length and width scale ratios between parent and daughter branches.

Fractal patterns can be found in nature and can be seen in coastlines, leaves and clouds [1.3]. Fractal patterns have been employed in heat exchangers to increase the surface area available for heat transfer. Van Der Vyver and Meyer [1.4, 1.5] developed a computational model for a tube-in-tube heat exchanger where the inner tube utilized a fractal pattern known as a quadratic Koch island. Casanova et al. [1.6] investigated a fractal heatsink antenna and concluded it offered greater radiation efficiency and directivity when compared to a patch

antenna and also decreased thermal resistance when compared to a traditional finned heat sink. Baliarda et al. and Vinoy et al. [1.7, 1.8] investigated fractal antennas and found their space-filling characteristics resulted in radiation efficiency that approached the theoretical limits for small antennas. Gonzalez-Arbesu et al. [1.9] utilized Hilbert curves in the design of a fractal antenna and concluded their use was impractical for radiating systems. However, the use of Hilbert curves as loads on top-loaded monopoles yielded higher radiation efficiencies and quality factors. Lee et al. [1.10] investigated the use of a fractal heat sink for application in a laser interferometer. Temperature variations adversely affect the frequency stability and thus measurement precision of laser interferometers. Lee et al. utilized a Hilbert curve to increase the surface area available for heat transfer and found it resulted in increased frequency stability.

There is a large body of literature that details the use of biologically-inspired designs for engineering applications. Tree-like internal flow passages, inspired by the vascular systems of plants and animals have shown to be advantageous as they minimize flow resistance [1.11, 1.12]. Murray [1.11] investigated the principle of minimum work in the vascular system and found there is an optimal change in hydraulic diameter at bifurcations in tree-like flow networks that minimizes flow resistance. This concept is known as Murray's law. Murray's law states that the cube of the radius of a parent branch equals the sum of the cubes of the radii of daughter branches. When Murray's law is obeyed, parent and daughter branches can be connected in a way that theoretically provides maximum bulk fluid transport for the least amount of work. A branching network that obeys Murray's law theoretically minimizes the flow resistance and thus pumping power required for fluid flow. Sherman [1.13], based on the work of Murray [1.11], concluded that when Murray's law is obeyed a functional relationship exists between channel diameters and various flow characteristics such as wall shear stress, velocity profile, and pressure

gradient. Similarly, West et al. [1.14-1.16] developed scaling laws for bulk fluid transport through space-filling fractal networks based on three assumptions: a tree-like branching network is required to supply an entire volume, the final branch level is size invariant, and the energy required to supply the flow network is minimized. Lee and Lee [1.17] measured six branching levels of the arterial bifurcations of chicken embryos and found the measured values closely approximated the theoretical values that Murray's law predicts. Lee and Lee also found that as the parent's diameter decreased the measured values more closely approached the theoretical values predicted by Murray's law. Lee and Lee attributed this trend to Murray's [1.11] use of Poiseuille's formula in his derivation. Bejan [1.18] developed a solution for optimizing conducting paths for application in cooling a heat generating volume and found the paths form a tree-like network. Bejan's optimization technique, known as "Constructal Theory," states that finite-volume systems evolve to afford easier access to the imposed currents that flow through it which explains the natural tendency of flow systems to evolve toward greater flow access [1.19, 1.20]. Bejan and Dan [1.21] utilized two different methods to optimize the geometry of a conducting path between a volume and a point and found the two methods resulted in constructal tree networks. Bejan's constructal theory attempts to theoretically unify structures found in nature while also providing guidelines for the geometric optimization of internal and external flow structures [1.22-1.23]. There are also several critical reviews examining constructal theory [1.24-1.25].

Hierarchical bifurcating geometries have been utilized extensively in the design of internal flow networks. These tree-like flow networks have been found to be advantageous when compared with traditional parallel straight channel flow networks. Pence [1.26] compared a heat sink with a fractal-like flow network to a heat sink with a parallel channel flow network of equal

surface area, pumping power, and flow rate. Pence found the fractal-like network resulted in lower total pressure drop and maximum wall temperature. Pence [1.26] developed a one-dimensional model for predicting the centerline pressure distribution for the fractal-like flow network under hydrodynamically and thermally developing conditions using a correlation provided in White [1.27]. Pence also developed a one-dimensional model for predicting the wall surface temperature along the fractal-like flow network. Pence [1.28] compared a square shaped heat sink with a parallel channel flow network to a disk shaped heat sink with a fractal-like branching flow network of equal surface area for heat transfer and found the fractal-like flow network resulted in increased thermal efficiency. Pence concluded that for a constant heat flux boundary condition, a more uniform surface temperature and lower total pressure drop could be achieved by utilizing a fractal-like flow network. Pence and Enfield [1.29] compared a heat sink with a fractal-like flow network and a heat sink with a parallel channel flow network of equal surface area, applied heat flux, and inlet flow rate and concluded the fractal-like network resulted in a higher maximum wall temperature. It should be noted that Pence and Enfield [1.29] utilized a width scale ratio as an alternative to a diameter scale ratio due to fabrication constraints. Alharbi et al. [1.30] found that the one-dimensional model developed by Pence [1.26] should incorporate temperature dependent fluid properties as assuming constant fluid properties led to an overestimation of pressure drop. Alharbi et al. also found that fractal-like flow networks result in a lower total pressure drop when compared to parallel channel flow networks due to local pressure recovery at bifurcations that result from an increase in flow area.

Alharbi et al. [1.31] similarly found that a fractal-like flow network resulted in a more uniform surface temperature when compared with a parallel channel flow network for the same maximum wall temperature. Wang et al. [1.32] found tree-like microchannel flow networks

resulted in improved temperature uniformity when compared with parallel channel flow networks. Wang et al. [1.32-1.33] also observed tree-like flow networks minimized the effect of channel blockage on fluid flow when compared with serpentine channel flow networks. Wang et al. [1.33] found that an increased number of parent channels emanating from the center of a disk shaped heat sink and an increased number of branch levels resulted in increased temperature uniformity. Kobayashi et al. [1.34] utilized a biologically-inspired evolutionary method to model complex dendritic structures for a fixed area and subject to uniform heat generation and concluded that there is an optimal level of complexity after which thermal performance does not greatly improve. Chen and Cheng [1.35] assessed the pressure drop and heat transfer capacity for a varying number of branch levels and diameter scale ratios while neglecting pressure recovery at bifurcations and assuming fully developed laminar flow. Chen and Cheng concluded a larger number of branch levels resulted in a higher heat transfer capability and lower total pressure drop. Chen and Cheng [1.36] experimentally confirmed that heat sinks with fractal-like flow networks are more thermally efficient than heat sinks with parallel channel flow networks for the same heat transfer rate, temperature difference, and inlet velocity. Enfield et al. [1.37] examined laminar mixing, which relies on molecular diffusion for mass transport, in microscale tree-like merging channel flow networks. Enfield et al. developed a numerical and experimental model for predicting concentration profiles and degree of mixing which allowed the optimal number of branch levels for a fixed initial parent channel width, total path length, and channel depth to be determined.

Senn and Poulikakos [1.38] found a tree-like branching flow network with six branch levels offered almost half the total pressure drop when compared with a serpentine flow pattern of equal surface area and inlet Reynolds number. Senn and Poulikakos also observed secondary

flow motions initiated at bifurcations. Senn and Poulikakos concluded transverse vortices created recirculation at bifurcations that resulted in hot spots at the inner corners of bifurcations and also observed longitudinal vortices resulted in enhanced thermal mixing and a decrease in the required flow rate for heat transfer. Wang et al. [1.39] found that the total pressure drop increased and hot spots became more noticeable as the bifurcation angle increased due to flow recirculation. Wang investigated 6 bifurcation angles ranging from 30° to 180° and found a bifurcation angle of 30° resulted in the lowest total pressure drop. Wang et al. [1.40] found asymmetrical leaf-like flow networks resulted in lower total pressure drop and higher average heat transfer coefficients than symmetric tree-like flow networks. Ghaedamini et al. [1.41] investigated the effect of channel svelteness on the bifurcation angle's role in pressure drop and flow uniformity. Ghaedamini et al. [1.41] concluded that as svelteness increases, flow uniformity increases and the effect of bifurcation angle on pressure drop decreases. Tree-like networks with a bifurcation angle of 30° were found to result in minimum pressure drop.

Conjugate heat transfer has also been examined for extended surfaces with biologically inspired designs. Fins, with biologically inspired, tree-like designs provide larger surface areas for heat transfer for the same mass and base area when compared to traditional employed rectangular fins. Lee and Lin [1.42] performed a second law analysis on fractal-like fins under cross flow and concluded that as the Reynolds number increases the number of optimal branch levels decreases. Lin and Lee [1.43] analytically investigated the thermal performance of branching fins with a power-law heat transfer coefficient. Xu et al. [1.44] investigated the optimal branching ratio for conducting paths and found it to be different from the optimal branching ratio predicted by Murray's law [1.11] for internal flow. Plawsky [1.45, 1.46] investigated the thermal performance of branched extended surfaces and concluded that while

the surface area of branching structures increase with branch level, there is a finite number of branch levels after which fin efficiency and effectiveness fail to increase. Plawsky found that the thermal performance of contracting branching structures was higher than that of expanding structures. The expanding structures studied had a fractal dimension of 1.74 while the contracting structures had a fractal dimension of 1.783. For expanding structures, daughter branches had a radius and length 110% larger than that of parent branches and bifurcated at a distance 25% of the total length of parent branches. For contracting structures, daughter branches had a radius and length 60% smaller than that of parent branches and bifurcated at a distance 75% of the total length of parent branches. Almogbel [1.47] presented a geometric optimization technique for tree-like fins based on fin volume and material and found that the global thermal conductance can be maximized. Almogbel concluded that optimized tree-like fins offer greater thermal performance when compared with longitudinal and optimized T-shaped fins. Lorenzini and Rocha [1.48] presented a numerical optimization of Y-shaped fins based on fin volume and material and through a triple optimization found an optimal structure that minimized the global thermal resistance. Y-shaped fin structures were found to offer increased thermal performance when compared to T-shaped structures.

While Plawsky [1.45, 1.46] examined contracting and expanding tree-like extended surfaces there has not been a significant investigation into the use of hierarchical bifurcating geometries in the design of extended surfaces specifically in natural convection. However, the thermal performance and geometric optimization of extended surfaces in natural convection has been extensively studied in the past for traditional rectangular geometries [1.49-1.50]. Mikk [1.51] developed an optimization method for minimizing the mass of convecting fins and concluded that the mass of an ideal fin differs only slightly from that of a fin with a triangular

profile. Mao and Rooke [1.52] developed an analytical solution for straight fins with convective boundary conditions at the fin tips and compared the results to previously developed solutions for straight fins with an adiabatic boundary condition at the fin tip. Mao and Rooke concluded neglecting tip convection led to significant errors for combinations of small length to width ratios as well as small Biot numbers. Leong and Kooi [1.53] experimentally investigated rectangular fins with varying material and base temperature and concluded that maximum heat transfer coefficients were located at positions between 22 and 45% of the fin height measured from the base. Temperature measurements along the fin were found to be in good agreement with one-dimensional solutions for convective fin tips. Razelos and Georgiou [1.54] presented new design criteria for extended surfaces and recommended the use of the fin removal number instead of fin effectiveness. The fin removal number is defined as the ratio of the heat dissipated by the fin to the heat dissipated from the base area in the absence of the fin. The design criteria presented require a heat transfer increase by an order magnitude of at least 10. A Biot number on the order of 0.01 and an aspect number on the order of 1 were recommended as design guidelines.

As with natural convection, there has not been an investigation into the use of tree-like geometries in the design of fins in thermal radiation heat transfer. However, the thermal performance and mass minimization of extended surfaces has been extensively studied in the past for rectangular and parabolic profiles radiating to free space where the temperature of the surroundings is absolute zero [1.55-1.62]. Geometric optimization of fin geometry to increase heat transfer per unit mass has also been studied. Aziz and Kraus [1.63] presented a thorough review and design reference of optimal geometries for radiating and convecting-radiating longitudinal fins of various profiles. Naumann [1.64] investigated flat and tapered rectangular fins joining circular tubes and developed an analytical expression to determine the maximum

heat radiated per unit mass. Naumann concluded that tapering fins yielded an increase in heat transfer per unit mass. Schnurr et al. [1.65] investigated radiating straight and circular fins of rectangular and triangular profile with varying surface emissivities and concluded that for a given heat rate and base temperature a minimum mass fin array could be achieved through tapering. Krikkis and Razelos [1.66] developed correlations for spacecraft radiators with rectangular and triangular profiles based on the criteria of volume minimization and heat rejection maximization. Krikkis and Razelos concluded optimal minimum mass fin geometries were contingent upon the opening angle between fins, fin surface emissivity, and fin profile. Kumar et al. [1.67] developed correlations for optimizing finned radiators and found an ideal number of fins exists which maximizes fin effectiveness.

There have been numerous studies that examined the effect of radiative interaction between components in spacecraft radiators. Khor et al. [1.68] experimentally investigated the effects of thermal radiation on fin performance and concluded that including thermal radiation without the use of view factors can result in significant error. Shabany [1.69] developed simple analytical correlations, based on the view factor between fins and their surroundings, for radiation heat transfer from diffuse and gray plate-fin heat sinks. Ellison [1.70] computed gray view factors for radiation heat transfer between fins and a nonreflecting ambient surface and concluded that some commonly employed methods for predicting gray body view factors had significant error when projected areas were utilized for fin height-to-spacing ratios greater than 3. Ellison found that fin structures with height-to-spacing ratios greater than 3 behaved as black bodies with surface areas equal to the projected areas. Ellison developed and recommended the use of an equivalent circuit for computing shape factors. Razelos and Krikkis [1.71] investigated the optimum dimensions of minimum volume and maximum heat rejection rectangular fins and

concluded that the radiative interaction between the fin and tube should be incorporated into models. Chung and Zhang [1.72-1.73] investigated the optimization of minimum mass longitudinal fins with mutual irradiation and concluded that radiative interaction at the base significantly impacted optimal fin geometry. Krishnaprakas and Narayana [1.74] investigated the optimal dimensions for rectangular fins with fin-fin radiation as well as diffuse and spectral surface reflection and concluded that an optimized geometry resulted in an array of short, thin fins.

The interaction between the combined conjugate effects of natural convection and radiation heat transfer is often neglected. Through an extensive literature review it can be concluded that thermal radiation comprises a significant amount of heat transfer in heat sinks often assumed to function in natural convection only. Dannelley and Baker [1.75] experimentally examined the use of two fractal geometries, the modified Koch snowflake and the Sierpinski carpet, for extended surface heat transfer enhancement. Dannelley and Baker found the fractal geometries were desirable when a decrease in fin mass is a performance criterion. Rao and Venkateshan [1.76] experimentally studied the effects of natural convection and radiation in horizontal fin arrays and concluded that it is invalid to utilize an additive approach in which losses associated with natural convection and radiation are independently calculated and subsequently combined together. Rao et al. [1.77] experimentally investigated natural convection with surface radiation and concluded that the radiation contribution to the total heat transfer was highly dependent on surface emissivity and varied between 5 and 50%. Rea and West [1.78] analytically investigated thermal radiation heat transfer from finned heat sinks and noted that radiation accounts for 25 to 50% of the heat dissipated by a finned heat sink typically assumed to operate in natural convection only. The range was found to be dependent on the heat sink design,

operating temperature, and ambient environment. Guglielmini, et al. [1.79] studied natural convection and radiation heat transfer from staggered vertical fins and similarly found that surface radiation accounted for 25 to 40% of the total heat dissipated by the extended surfaces under the conditions studied. Sasikumar and Balaji [1.80] investigated the effects of radiation and natural convection in a plate fin heat sink and noted that radiation could amount to 55% of the total heat dissipated. Kobus and Oshio [1.81] performed a theoretical and experimental study that investigated the influence of radiation on the thermal performance of a pin fin array. Kobus and Oshio recommended the use of an effective radiation heat transfer coefficient that could be added to the convective heat transfer coefficient to yield an overall heat transfer coefficient.

Incorporating hierarchical bifurcating flow passages in heat exchangers is a relatively new topic that has not been studied extensively in the past. Bejan [1.82] utilized constructal theory in the geometric optimization of a small-scale crossflow heat exchanger as well as a large-scale counterflow heat exchanger. The tree-like heat exchangers had the advantages of reduced flow resistance and increased heat transfer per unit volume when compared to parallel channel heat exchangers. Azad and Amidpour [1.83] employed constructal theory in the economic optimization of a shell and tube heat exchanger and concluded the constructal design resulted in a 50% reduction in total cost when compared with the traditional method of design. Raja et al. [1.84] utilized constructal theory in the design of a multi-block heat exchanger and concluded the constructal heat exchangers were 20% more effective when compared to conventional crossflow heat exchangers. However, the constructal heat exchangers resulted in a 20-32% increase in pressure drop. Zimparov et al. [1.85] presented a geometric optimization of constructal tree-shaped parallel flow heat exchangers with several different configurations and levels of complexity. Zimparov et al. concluded as the level of complexity increases the performance

curves of different flow structures will eventually converge. Zhang et al. [1.86] presented the conditions where tree vascularization offered smaller global thermal resistance when compared with conventional parallel channels in counterflow heat exchangers. Zhang et al. found fluid outlet temperature uniformity decreased as the level of complexity increased. Zamfirescu and Bejan [1.87] presented optimized flow structures for constructal tree-shaped networks with an evaporating refrigerant as the working fluid. da Silva and Bejan [1.88] experimentally investigated the hydraulic and thermal behavior of a dendritic counterflow heat exchanger. da Silva and Bejan concluded that as the flow rate increased the effect of asymmetric bifurcations on flow division also increased which resulted in decreased temperature uniformity. Bonjour et al. [1.89] compared branched and radial fins in a coaxial two-stream heat exchanger and concluded the benefit of branched fins was highly dependent on the size of the heat exchanger cross-section.

The use of porous media to enhance heat transfer in heat exchangers has been studied in the past. Allouache and Chikh [1.90] investigated the effect of porous layer thickness, permeability, and effective thermal conductivity on the performance of an annular heat exchanger. Allouache and Chikh recommended criteria for porous media to minimize pressure drop and enhance heat transfer. Al-Salem et al. [1.91] experimentally investigated the effects of porosity and thickness of porous sheets over a heated cylinder in cross flow. The addition of the porous layers enhanced heat transfer and was not found to increase the pressure drop across the system. Lan and Khodadadi [1.92] performed a theoretical study of fluid flow and heat transfer through a porous media filled channel with permeable walls and presented Nusselt and Peclet numbers as a function of inlet Reynolds number. Mohamad [1.93] investigated the heat transfer enhancement due to porous media in a pipe and found partially filling the pipe enhanced the rate

of heat transfer and resulted in less pressure drop when compared with a pipe completely filled with porous media. Narasimhan and Raju [1.94] numerically studied porous medium inter-connectors in a compact heat exchanger and concluded the tube-to-tube inter-connectors enhanced the heat transfer from the tubes to the working fluid. Odabae and Hooman [1.95] performed a numerical study on a heat exchanger composed of aluminum tubes wrapped by porous metal foam in crossflow. The porous metal foam resulted in an increase in the area goodness factor when compared with a traditional finned-tube heat exchanger. Pavel and Mohamad [1.96] utilized porous inserts in a heat transfer pipe and found the inserts resulted in a higher heat transfer rate but also increased the pressure drop. Targui and Kahalerras [1.97] performed a numerical study on flow and heat transfer characteristics in a double pipe heat exchanger with porous inserts. Targui and Kahalerras found staggering the inserts in both cylinders yielded the highest heat transfer rates. Yang and Hwang [1.98] investigated turbulent heat transfer enhancement in a heat exchanger pipe filled with porous media and found the porous media improved the heat transfer performance of fluid channels but also increased the pressure drop. Yang and Hwang, like Mohamad [1.96], recommended partially filling conduits with porous media to mitigate the increase in pressure drop. Zhao and Song [1.99] found that for forced convection in porous media heated by a permeable wall the Nusselt number equals the Peclet number.

The use of porous media to enhance heat transfer is not limited to applications in heat exchangers. Bhanja and Kundu [1.100] developed an analytical technique to determine the thermal performance of constructal T-shaped porous fins. Bhanja and Kundu incorporated the effect of thermal radiation on natural convection heat transfer. The thermal performance of the T-shaped fins was found to increase as porosity increased. Kiwan and Al-Nimr [1.101] compared

the thermal performance of porous fins and traditional solid fins. Kiwan and Al-Nimr found the performance of the porous fins increased with the Rayleigh number. Kundu and Bhanja [1.102] performed a parametric analysis to enhance the thermal performance of porous fins and found the optimum heat transfer rate increases with the ambient temperature and decreases with the base temperature. Kundu et al. [1.103] compared porous and solid fins of various profiles and found the porous fins were more effective at all profiles for low porosities. Kiwan [1.104] investigated the effect of radiation heat transfer on natural convection heat transfer from a porous fin and found the effects of thermal radiation decreased as the Rayleigh number increased.

The work here calls for the use of both internal flow passages as well as extended surfaces with hierarchical bifurcating geometries in solid and porous materials. Calamas and Baker [1.105] previously examined the scaling of fractal-like internal flow networks and found microscale and mesoscale flow networks offer similar thermal performance while mesoscale networks have the additional advantage of reduced pressure drop. However, the use of hierarchical bifurcating flow passages for application in compact heat exchangers has not been previously investigated. Similarly, the use of porous media in compact heat exchangers with hierarchical bifurcating flow passages has not been previously investigated. Calamas and Baker [1.106, 1.107] investigated the use of fins with hierarchical bifurcating geometries in natural convection and radiation heat transfer and found the tree-like fins offer improved thermal performance when compared to traditional rectangular extended surfaces. The knowledge obtained from the literature review can be utilized to further understand the advantages that hierarchical bifurcating geometries provide in thermal transport systems.

Motivation

Biomimetics is the use of biologically-inspired solutions for engineering applications. Flow systems have a natural tendency to evolve toward greater flow access which can easily be seen in rivers and the veins of tree leaves. Similarly, the human lungs have a surface area to volume ratio an order of magnitude larger than that of a traditional radiator found in a motor vehicle. These biologically-inspired systems produce space-filling networks, minimize flow resistance, and enhance surface area to volume ratios for heat transfer. Almost all of the National Academy of Engineering Grand Challenges for Engineering have a relation to thermal and fluid transport. For example, heat transfer is critically important in making solar energy economical. Heat transfer is equally important in securing cyberspace infrastructure as data centers must be cooled. Fluid transport is also vital in providing access to clean water and developing carbon sequestration methods. Looking again to nature, mangrove trees have been found to offer excellent carbon capturing, salt filtration and even close the pores on their leaves to reduce sun exposure as well as absorb heat to prevent evaporation of the shallow water that makes up their habitat.

By utilizing hierarchical bifurcating geometries in internal flow passages an increase in surface area for heat transfer yields improved thermal performance. The reduction in pumping power associated with the use of hierarchical bifurcating flow passages reduces the required power input to compact heat exchangers. Similarly, the use of porous materials further enhances the surface area available for heat transfer while simultaneously reducing system mass. When hierarchical bifurcating geometries are utilized in extended surfaces, significant gains in available surface areas can be achieved for the same mass, volume, and base area as traditionally utilized extended surfaces. Biologically-inspired geometries thus have the potential to increase

natural convection heat transfer for a variety of commercial and industrial applications. It is also critically important to optimize the design of extended surfaces utilized by space heat rejection systems to maximize heat rejection while minimizing mass. As thermal radiation is a function of the available surface area it is important to maximize the surface area without increasing the mass or volume of the system. Hierarchical bifurcating geometries can thus be used in extended surfaces utilized by space heat rejection systems to maximize the surface area for thermal radiation heat transfer.

Objectives

The primary objective of the presented work is to better quantify and qualify the heat transfer performance and flow behavior of hierarchical bifurcating geometries utilized in extended surfaces and internal flow networks composed of solid and porous materials. In order to complete the objective for this work, five major tasks were undertaken as listed below:

- 1) A computational model, validated by an analytical solution and experimental data and verified for grid independence, was used to evaluate the effect of scaling on the thermal and fluid behavior of a network with hierarchical bifurcating flow passages. A microscale flow network was compared to a mesoscale flow network. Performance was evaluated across two scales for a fixed flow rate and surface heat flux. Results were non-dimensionalized in order to better compare the thermal and fluid performance of the hierarchical bifurcating flow networks across the two length scales.
- 2) A computational model, validated by an analytical solution and verified for grid independence, was used to evaluate the thermal performance of tree-like extended surfaces thermally radiating to free space. The investigation was conducted for a range of thicknesses, bifurcation angles, materials, and base heat rates. The thermal performance was evaluated on

fin effectiveness, fin efficiency, and fin base temperature. The tree-like extended surfaces were compared to rectangular extended surfaces of equal mass, volume, and base area.

- 3) A computational model, validated by an analytical solution and verified for grid independence, was used to evaluate the thermal performance of tree-like extended surfaces in a naturally convecting environment. The investigation was conducted for a range of scales, thicknesses, bifurcation angles, materials, and base heat rates. The thermal performance was evaluated on fin effectiveness, fin efficiency, and fin base temperature. The tree-like extended surfaces were compared to rectangular extended surfaces of equal mass, volume, and base area.
- 4) An experimental investigation was used to evaluate the system performance of a single fluid solid-liquid compact heat exchanger with hierarchical bifurcating internal flow passages. Heat exchanger disks with hierarchical bifurcating flow passages were manufactured out of aluminum. The experimental investigation was conducted for a range of applied heat rates and flow rates. The results, presented in the form of commonly defined dimensionless parameters, demonstrate that system performance can be characterized in a mode similar to traditional compact heat exchanger designs with two fluid streams.
- 5) A computational model, validated by an analytical solution and experimental data and verified for grid independence, was used to evaluate the effect of bifurcation angle, porosity, and pore size on the fluid behavior of a porous disk with hierarchical bifurcating internal flow passages. The computational investigation was performed for a range of porosities, pore sizes, bifurcation angles, and flow rates. The flow behavior through the hierarchical bifurcating channels as well as through the porous material was examined. The fluid performance was evaluated on pressure drop as a function of flow rate.

References

- [1.1] Thompson, D'A. W., 1942, *On Growth and Form*, Cambridge University Press, Cambridge.
- [1.2] Mandelbrot, B. B., 1982, *The Fractal Geometry of Nature*, Freeman, New York.
- [1.3] Barnsley, M., 1988, *Fractals Everywhere*, Academic Press, San Diego.
- [1.4] Van Der Vyver, H., 2003, "Validation of a CFD Model of a Three-Dimensional Tube-in-Tube Heat Exchanger," *Proceedings of the Third International Conference on CFD in the Minerals and Process Industries*, CSIRO, Melbourne, Australia, pp. 235-240.
- [1.5] Meyer, J., and Van Der Vyver, H., 2005, "Heat Transfer Characteristics of a Quadratic Koch Island Fractal Heat Exchanger," *Heat Transfer Engineering*, 26(9), pp. 22-29.
- [1.6] Casanova, J. J., Taylor, J. A., and Lin, A., 2010, "Design of a 3-D Fractal Heatsink Antenna," *IEEE Antennas and Wireless Propagation Letters*, 9, pp. 1061-1064.
- [1.7] Baliarda, C. P., Romeu, J., and Cardama, A., 2000, "The Koch Monopole: A Small Fractal Antenna," *IEEE Transactions on Antennas and Propagation*, 48, pp. 1773-1781.
- [1.8] Vinoy, K. J., Jose, K.A., Varadan, V. K. and Varadan, V.V., 2001, "Hilbert Curve Fractal Antenna: A Small Resonant Antenna for VHF/UHF Applications," *Microwave and Optical Technology Letters*, 29, pp. 215-219.
- [1.9] Gonzalez-Arbesu, J. M., Blanch, S., and Romeu, J., 2003, "The Hilbert Curve as a Small Self-Resonant Monopole from a Practical point of View," *Microwave and Optical Technology Letters*, 39(1), pp. 45-48.
- [1.10] Lee, S. R., Li, Z. G., Wang, B. G., and Chiou, H. S., 2005, "An Application of the Fractal Theory in the Design of Heat Sink for Precision Measurement Instrument," *Key Engineering Materials*, 295, pp. 717-722.
- [1.11] Murray, C. D., 1926, "The Physiological Principle of Minimum Work. I. The Vascular System and the Cost of Blood Volume", *Journal of Physiology*, 12(3), pp. 207-214.
- [1.12] Cohn, D. L., 1954, "Optimal Systems: The Vascular System," *Bulletin of Mathematical Biophysics*, 16, pp. 59-74.

- [1.13] Sherman, T. F., 1997, "The Meaning of Murray's Law," *Journal of General Physiology*, 78, pp. 431-453.
- [1.14] West, G. B., Brown, J. H., and Enquist, B. J., 1997, "A General Model for the Origin of Allometric Scaling Laws in Biology," *Science*, 276, pp. 122-126.
- [1.15] West, G. B., Brown, J. H., and Enquist, B. J., 1999, "The Fourth Dimension of Life: Fractal Geometry and Allometric Scaling of Organisms," *Science*, 284, pp. 1677-1679.
- [1.16] West, G. B., 1999, "The Origin of Universal Scaling Laws in Biology," *Physica A*, 263, pp. 104-113.
- [1.17] Lee, J. Y., and Lee, S. J., 2010, "Murray's Law and the Bifurcation Angle in the Arterial Micro-Circulation System and Their Application to the Design of Microfluidics," *Journal of Microfluidics and Nanofluidics*, 8(1), pp. 85-95.
- [1.18] Bejan, A., 1997, "Constructal-Theory Network of Conducting Paths for Cooling a Heat Generating Volume," *International Journal of Heat and Mass Transfer*, 40(4), pp. 799-816.
- [1.19] Bejan, A., and Lorente, S., 2010, "The Constructal Law of Design and Evolution in Nature," *Philosophical Transactions of the Royal Society B*, 365(1545), pp. 1335-1347.
- [1.20] Bejan, A., and Lorente, S., 2006, "Constructal Theory of Generation of Configuration in Nature and Engineering," *Journal of Applied Physics*, 100(4), 2006.
- [1.21] Bejan, A., and Dan, N., 1999, "Two Constructal Routes to Minimal Heat Flow Resistance via Greater Internal Complexity," *Journal of Heat Transfer*, 121(1).
- [1.22] Bejan, A., Lorente, S., and Lee, J., 2008, "Unifying Constructal Theory of Tree Roots, Canopies and Forests," *Journal of Theoretical Biology*, 254(3), pp. 529-540.
- [1.23] Rocha, L. A. O., Lorenzini, E., and Biserni, C., 2005, "Geometric Optimization of Shapes on the Basis of Bejan's Constructal Theory," *International Communications in Heat and Mass Transfer*, 32(10), pp. 1281-1288.
- [1.24] Kuddusi, L., and Egrican, N., 2008, "A Critical Review of Constructal Theory," *Energy Conversion and Management*, 49(5), pp. 1283-1294.

- [1.25] Ghodoossi, L., "Conceptual Study on Constructal Theory," *Energy Conversion and Management*, 45(9-10), pp. 1379-1395.
- [1.26] Pence, D. V., 2002, "Reduced Pumping Power and Wall Temperature in Microchannel Heat Sinks with Fractal-Like Branching Channel Networks," *Microscale Thermophysical Engineering*, 6, pp. 319-330.
- [1.27] White, F. M., 1991, *Viscous Fluid Flow*, 2nd ed., McGraw-Hill, New York, pp. 291-293.
- [1.28] Pence, D. V., 2000, "Improved Thermal Efficiency and Temperature Uniformity Using Fractal-Like Branching Channel Networks," *Proc. International Conference on Heat Transfer and Transport Phenomena in Microscale*, edited by G. P. Celesta, New York, pp. 142-148.
- [1.29] Pence, D. V., and Enfield, K. E., 2004, "Inherent Benefits in Microscale Fractal-Like Devices for Enhanced Transport Phenomena," *Design and Nature II*, WIT Press, Boston, pp. 317-327.
- [1.30] Alharbi, A. Y., Pence, D. V., and Cullion, R. N., 2004, "Fluid Flow through Microscale Fractal-Like Branching Channel Networks," *Journal of Fluids Engineering*, 125(6), pp. 1051-1057.
- [1.31] Alharbi, A. Y., Pence, D. V., and Cullion, R. N., 2004, "Thermal Characteristics of Microscale Fractal-Like Branching Channels," *Journal of Heat Transfer*, 126(5), pp. 744-755.
- [1.32] Wang, X. Q., Mujumdar, A. S., and Yap, C., 2006, "Thermal Characteristics of Tree-Shaped Microchannel Nets for Cooling of a Rectangular Heat Sink," *International Journal of Thermal Sciences*, 45(11), pp. 1103-1112.
- [1.33] Wang, X. Q., Mujumdar, A. S., and Yap, C., 2006, "Numerical Analysis of Blockage and Optimization of Heat Transfer Performance of Fractal-Like Microchannel Nets," *Journal of Electronic Packaging*, 128(1), pp. 38-45.
- [1.34] Kobayashi, M. H., Pedro, H. T. C., Coimbra, C. F. M., and da Silva, A. K., 2009, "Formal Evolutionary Development of Low-Entropy Dendritic Thermal Systems," *Journal of Thermophysics and Heat Transfer*, 23(4), pp. 822-827.

- [1.35] Chen, Y., and Cheng, P., 2002, "Heat Transfer and Pressure Drop in Fractal Tree-Like Microchannel Nets," *International Journal of Heat and Mass Transfer*, 45(13), pp. 2643-2648.
- [1.36] Chen, Y., and Cheng, P., 2005, "An Experimental Investigation on the Thermal Efficiency of Fractal Tree-Like Microchannel Nets," *International Communications in Heat and Mass Transfer*, 32(7), pp. 931-938.
- [1.37] Enfield, K. E., Siekas, J. J., and Pence, D. V., 2004, "Laminate Mixing in Microscale Fractal-Like Merging Channel Networks," *Journal of Microscale Thermophysical Engineering*, 8(5), pp. 207-224.
- [1.38] Senn, S. M., and Poulikakos, D., 2004, "Laminar Mixing, Heat Transfer and Pressure Drop in Tree-Like Microchannel Nets and Their Application for Thermal Management in Polymer Electrolyte Fuel Cells," *Journal of Power Sources*, 130(1-2), pp. 178-191.
- [1.39] Wang, X. Q., Mujumdar, A. S., and Yap, C., 2007, "Effect of Bifurcation Angle in Tree-Shaped Microchannel Networks," *Journal of Applied Physics*, 102(7).
- [1.40] Wang, X. Q., Mujumdar, A. S., and Yap, C., 2010, "Flow and Thermal Characteristics of Offset Branching Network," *International Journal of Thermal Sciences*, 49(2), 2010, pp. 272-280.
- [1.41] Ghaedamini, H., Salimpour, M. R., and Mujumdar, A. S., 2011, "The Effect of Sveltiness on the Bifurcation Angles Role in Pressure Drop and Flow Uniformity of Tree-Shaped Microchannels," *Applied Thermal Engineering*, 31(5), pp. 708-716.
- [1.42] Lee, D. J., and Lin, W. W., 1995, "Second Law Analysis on Fractal-Like Fin under Crossflow," *AIChE Journal*, 41(1), pp. 2314-2317.
- [1.43] Lin, W. W., and Lee, D. J., 1997, "Diffusion-Convection Process in a Branching Fin," *Chemical Engineering Communications*, 158(1), pp. 59-70.
- [1.44] Xu, P., Yu, B., Yun, M., and Zou, M., 2006, "Heat Conduction in Fractal Tree-Like Branched Networks," *International Journal of Heat and Mass Transfer*, 49, pp. 3746-3751.
- [1.45] Plawsky, J. L., 1993, "Transport in Branched Systems I: Steady-State Response," *Chemical Engineering Communications*, 123(1), pp. 71-86.

- [1.46] Plawsky, J. L., 1993, "Transport in Branched Systems II: Transient Response," *Chemical Engineering Communications*, 123(1), pp. 87-109.
- [1.47] Almogbel, M. A., 2005, "Constructal Tree-Shaped Fins," *International Journal of Thermal Sciences*, 44(4), pp. 342-348.
- [1.48] Lorenzini, G., and Rocha, L. A. O., 2006, "Constructal Design of Y-Shaped Assembly of Fins," *International Journal of Heat and Mass Transfer*, 49(23-24), pp. 4552-4557.
- [1.49] Aziz, A., 1992, "Optimum Dimensions of Extended Surfaces Operating in a Convective Environment," *Applied Mechanics Reviews*, 45(5), pp. 155-173.
- [1.50] Kraus, A. D., 1999, "Developments in the Analysis of Finned Arrays," *International Journal of Transport Phenomenon*, 1, pp. 141-164.
- [1.51] Mikk, I., 1980, "Convective Fin of Minimum Mass," *International Journal of Heat and Mass Transfer*, 23(5), pp. 707-711.
- [1.52] Mao, J., and Rooke, S., 1994, "Transient Analysis of Extended Surfaces with Convective Tip," *International Communications in Heat and Mass Transfer*, 32(1), pp. 85-94.
- [1.53] Leong, K. C., and Kooi, T. C., 1996, "Natural Convection from a Vertical Rectangular Fin," *Experimental Heat Transfer*, 9(4), pp. 287-303.
- [1.54] Razelos, P., and Georgiou, E., 1992, "Two-Dimensional Effects and Design Criteria for Convective Extended Surfaces," *Journal of Heat Transfer Engineering*, 13(3), pp. 36-48.
- [1.55] Schmidt, E., 1926, "Die Wärmeübertragung durch Rippen, Z.," *Verein. Deutsch. Ing.*, 70, pp. 885-889.
- [1.56] Duffin, R. J., 1959, "A Variational Problem Relating to Cooling Fins," *Journal of Mathematics and Mechanics*, 8, pp. 47-56.
- [1.57] Liu, C., 1962, "A Variational Problem with Applications to Cooling Fins," *Journal of Society for Industrial and Applied Mechanics*, 10(1), pp. 19-29.
- [1.58] Mackay, D. B., and Leventhal, E. L., 1960, "Radiant Heat Transfer from a Flat Plate Uniformly Heated Along the Edge," *AICHE 4th National Heat Transfer Conference*, New York.

- [1.59] Wilkins, J. E., 1960, "Minimum-Mass Thin Fins which Transfer Heat Only by Radiation to Surroundings at Absolute Zero," *Journal of Society for Industrial and Applied Mathematics*, 8(4), pp. 630-639.
- [1.60] Bartas, J. G., and Sellers, W. H., 1960, "Radiation Fin Effectiveness," *Journal of Heat Transfer*, 82C, pp. 73-75.
- [1.61] Sparrow, E. M., and Eckert, E. R. G., 1962, "Radiant Interaction between Fin and Base Surfaces," *Journal of Heat Transfer*, 84(1), pp. 12-18.
- [1.62] Callinan, J. P., and Berggren, W. P., 1959, "Some Radiator Design Criteria for Space Vehicles," *Journal of Heat Transfer*, 81C, pp. 237-238.
- [1.63] Aziz, A., and Kraus, A. D., 1996, "Optimum Design of Radiating and Convecting-Radiating Fins," *Heat Transfer Engineering*, 17(3), pp. 44-78.
- [1.64] Naumann, R. J., 2004, "Optimizing the Design of Space Radiators," *International Journal of Thermophysics*, 25(6), pp. 1929-1941.
- [1.65] Schnurr, N. M., Shapiro, A. B., and Townsend, M. A., 1976, "Optimization of Radiating Fin Arrays With Respect to Weight," *Journal of Heat Transfer*, 98(4), pp. 643-648.
- [1.66] Krikkis, R. N., and Razelos, P., 2002, "Optimum Design of Spacecraft Radiators with Longitudinal Rectangular and Triangular Fins," *Journal of Heat Transfer*, 124(5), pp. 805-812.
- [1.67] Kumar, S. S., Nayak, N., and Venkateshan, S. P., 1993, "Optimum Finned Space Radiators," *International Journal of Heat and Fluid Flow*, 14(2), pp. 191-200.
- [1.68] Khor, Y. K., Hung, Y. M., and Lim, B. K., 2002, "On the Role of Radiation View Factor in Thermal Performance of Straight-Fin Heat Sinks," *International Communications in Heat and Mass Transfer*, 37(8), pp.1087-1095.
- [1.69] Shabany, Y., 2008, "Radiation Heat Transfer from Plate-Fin Heat Sinks," *Semiconductor Thermal Measurement and Management Symposium*, pp. 132-136.
- [1.70] Ellison, G. N., 1979, "Generalized Computations of the Gray Body Shape Factor for Thermal Radiation from a Rectangular U-Channel," *IEEE Transactions on Components, Hybrids and Manufacturing Technology*, 2(4), pp. 517-522.

- [1.71] Razelos, P., and Krikkis, R. N., 2001, "Optimum Design of Longitudinal Rectangular Fins with Base-to-Fin Radiant Interaction," *Heat Transfer Engineering*, 22(4), pp. 3-17.
- [1.72] Chung, B. T. F., and Zhang, B. X., 1991, "Minimum Mass Longitudinal Fins with Radiation Interaction at the Base," *Journal of the Franklin Institute*, 328(1), pp. 143-161.
- [1.73] Chung, B. T. F., and Zhang, B. X., 1991, "Optimization of Radiating Fin Array Including Mutual Irradiation Between Radiator Elements," *Journal of Heat Transfer*, 113(4), pp. 814-822.
- [1.74] Krishnaprakas, C. K., and Narayana, K. B., 1993, "Heat Transfer Analysis of Mutually Irradiating Fins," *International Journal of Heat and Mass Transfer*, 46(5), pp. 761-769.
- [1.75] Dannelley, D., and Baker, J., 2012, "Natural Convection Fin Performance Using Fractal-Like Geometries," *Journal of Thermophysics and Heat Transfer*, Accepted for Publication.
- [1.76] Rao, V., and Venkateshan, S. P., 1996, "Experimental Study of Free Convection and Radiation in Horizontal Fin Arrays," *International Journal of Heat and Mass Transfer*, 39(4), pp. 779-789.
- [1.77] Rao, V., Balaji, C., and Venkateshan, S. P., 1997, "Inferometric Study of Interaction of Free Convection with Surface Radiation in an L Corner," *International Journal of Heat and Mass Transfer*, 40(12), pp. 2941-2947.
- [1.78] Rea, S., and West, S. E., 1976, "Thermal Radiation from Finned Heat Sinks," *IEEE Transactions on Parts, Hybrids, and Packaging*, 12(2), pp. 115-117.
- [1.79] Guglielmini, G., Nannei, E., and Tanda, G., 1987, "Natural Convection and Radiation Heat Transfer from Staggered Vertical Fins," *International Journal of Heat and Mass Transfer*, 30(9), pp. 1941-1948.
- [1.80] Sasikumar, M., and Balaji, C., 2002, "A Holistic Optimization of Convecting-Radiating Fin Systems," *Journal of Heat Transfer*, 124(6), pp. 110-1116.
- [1.81] Kobus, C. J., and Oshio, T., 2005, "Predicting the Thermal Performance Characteristics of Staggered Vertical Pin Fin Array Heat Sinks under Combined Mode Radiation and Mixed Convection with Impinging Flow," *International Journal of Heat and Mass Transfer*, 48, pp. 2684-2696.

- [1.82] Bejan, A., 2002, "Dendritic Constructal Heat Exchanger with Small-Scale Crossflows and Larger-Scales Counterflows," *International Journal of Heat and Mass Transfer*, 45, pp. 4607-4620.
- [1.83] Azad, A. V., and Amidpour, M., 2011, "Economic Optimization of Shell and Tube Heat Exchanger Based on Constructal Theory," *Energy*, 26, pp. 1087-1096.
- [1.84] Raja, V. A. P., Basak, T., and Das, S. K., 2008, "Thermal Performance of a Multi-Block Heat Exchanger Designed on the Basis of Bejan's Constructal Theory," *International Journal of Heat and Mass Transfer*, 51, pp. 3582-3594.
- [1.85] Zimparov, V. D., da Silva, A. K., and Bejan, A., 2006, "Constructal Tree-Shaped Parallel Flow Heat Exchangers," *International Journal of Heat and Mass Transfer*, 49, pp. 4558-4566.
- [1.86] Zhang, H., Lorente, S., and Bejan, A., 2009, "Vascularization with Line-to-Line Trees in Counterflow Heat Exchange," *International Journal of Heat and Mass Transfer*, 52, pp. 4372-4342.
- [1.87] Zamfirescu, C., and Bejan, A., 2003, "Constructal Tree-Shaped Two-Phase Flow for Cooling a Surface," *International Journal of Heat Transfer*, 46, pp. 2785-2797.
- [1.88] da Silva, A. K., and Bejan, A., 2006, "Dendritic Counterflow Heat Exchanger Experiments," *International Journal of Thermal Sciences*, 45, pp. 860-869.
- [1.89] Bonjour, J., Rocha, L. A. O., Bejan, A., and Meunier, F., 2004, "Dendritic Fins Optimization for a Coaxial Two-Stream Heat Exchanger," *International Journal of Heat and Mass Transfer*, 47(1), pp. 111-124.
- [1.90] Allouache, N., Chikh, S., 2004, "Entropy Generation in a Partly Porous Heat Exchanger," *Computer Aided Chemical Engineering*, 18, pp. 139-144.
- [1.91] Al-Salem, K., Oztop, H. F., and Kiwan, S., 2011, "Effects of Porosity and Thickness of Porous Sheets on Heat Transfer Enhancement in a Cross Flow Over Heat Cylinder," *International Communications in Heat and Mass Transfer*, 38, pp. 1279-1282.
- [1.92] Lan, X. K., and Khodadadi, J. M., 1993, "Fluid Flow and Heat Transfer through a Porous Medium Channel with Permeable Walls," *International Journal of Heat and Mass Transfer*, 36(8), pp. 2242-2245.

- [1.93] Mohamad, A. A., 2003, "Heat Transfer Enhancements in Heat Exchangers Fitted with Porous Media Part I: Constant Wall Temperature," *International Journal of Thermal Sciences*, 42, pp. 385-395.
- [1.94] Narasimhan, A., Raju, K. S., 2007, "Effect of Variable Permeability Porous Medium Inter-Connectors on the Thermo-Hydraulics of Heat Exchanger Modeled as Porous Media," *International Journal of Heat and Mass Transfer*, 50, pp. 4052-4062.
- [1.95] Odabae, M., and Hooman, K., 2012, "Metal Foam Heat Exchangers for Heat Transfer Augmentation from a Tube Bank," *Applied Thermal Engineering*, 36, pp. 456-463.
- [1.96] Pavel, B. I., and Mohamad, A. A., 2004, "An Experimental and Numerical Study on Heat Transfer Enhancement for Gas Heat Exchangers Fitted with Porous Media," *International Journal of Heat and Mass Transfer*, 47, pp. 4939-4952.
- [1.97] Targui, N., and Kahalerras, H., 2008, "Analysis of Fluid Flow and Heat Transfer in a Double Pipe Heat Exchanger with Porous Structures," *Energy Conversion and Management*, 49, pp. 3217-3229.
- [1.98] Yang, Y., and Hwang, M., 2009, "Numerical Simulation of Turbulent Fluid Flow and Heat Transfer Characteristics in Heat Exchangers Fitted with Porous Media," *International Journal of Heat and Mass Transfer*, 52, pp. 2956-2965.
- [1.99] Zhao, T. S., and Song, Y. J., 2001, "Forced Convection in a Porous Medium Heated by a Permeable Wall Perpendicular to Flow Direction: Analyses and Measurements," *International Journal of Heat and Mass Transfer*, 44, pp. 1031-1037.
- [1.100] Banja, D., and Kundu, B., 2011, "Thermal Analysis of a Constructal T-Shaped Porous Fin with Radiation Effects," *International Journal of Refrigeration*, 34(6), pp. 1483-1496.
- [1.101] Kiwan, S., and Al-Nimr, M. A., 2001, "Using Porous Fins for Heat Transfer Enhancement," *Journal of Heat Transfer*, 123(4), pp. 790-796.
- [1.102] Kundu, B., and Bhanja, D., 2011, "An Analytical Prediction for Performance and Optimum Design Analysis of Porous Fins," *International Journal of Refrigeration*, 34(1), pp. 337-352.

- [1.103] Kundu, B., Bhanja, D., and Lee, K., 2012, "A Model on the Basis of Analytics for Computing Maximum Heat Transfer in Porous Fins," *International Journal of Heat and Mass Transfer*.
- [1.104] Kiwan, S., 2007, "Effect of Radiative Losses on the Heat Transfer from Porous Fins," *International Journal of Thermal Sciences*, 46(1), pp. 1046-1055.
- [1.105] Calamas, D., and Baker, J., 2013, "Performance of a Biologically-Inspired Heat Exchanger with Hierarchical Bifurcating Flow Passages," *Journal of Thermophysics and Heat Transfer*, 2012, Accepted for Publication.
- [1.106] Calamas, D., and Baker, J., 2013, "Behavior of Thermally Radiating Tree-Like Fins," *Journal of Heat Transfer*, Accepted for Publication.
- [1.107] Calamas, D., and Baker, J., 2013, "Tree-Like Branching Fins: Performance and Natural Convective Heat Transfer Behavior," *International Journal of Heat and Mass Transfer*, 2013, Accepted for Publication.

CHAPTER 2

PERFORMANCE OF A BIOLOGICALLY-INSPIRED HEAT EXCHANGER WITH HIERARCHICAL BIFURCATING FLOW PASSAGES*

Abstract

The performance of a heat exchanger with tree-like flow passages has been examined. The hierarchical bifurcating flow passages in the heat exchanger mimic those seen in the vascular systems of plants and animals. Overall system performance was examined computationally. The results, cast in terms of commonly defined dimensionless parameters, show that system performance can be characterized in a manner similar to traditional compact heat exchanger designs. Previous use of hierarchical bifurcating flow passages for heat exchanger applications has typically been limited to microscale flow networks. The mesoscale flow network examined here resulted in pressure and wall temperature distributions similar to previously studied microscale networks. The mesoscale flow network resulted in a total pressure drop two orders of magnitude smaller and a bulk fluid temperature increase an order of magnitude larger than the microscale flow network under the conditions studied.

Introduction

Biomimetics is the use of biologically-inspired solutions for engineering applications. In biological systems, hierarchical bifurcating flow passages produce space-filling flow networks, minimize flow resistance, and enhance surface area to volume ratios. These are all desirable characteristics for heat exchangers as well as biological systems. Applications for biologically-

* This chapter is based on Calamas, D., and Baker, J., 2012, "Performance of a Biologically-Inspired Heat Exchanger with Hierarchical Bifurcating Flow Passages," Journal of Thermophysics and Heat Transfer, Accepted for Publication.

inspired space-filling flow networks include spacecraft thermal management and the cooling of electronic systems. A fractal is a geometric shape that can be split into parts that are scaled copies of the whole, a property known as self-similarity [2.1]. The terms “fractal-like,” and “tree-like” are often employed interchangeably to describe flow networks with hierarchical bifurcating flow passages. Tree-like flow networks have many advantages when compared to parallel-flow networks. Tree-like flow networks have greater surface area for heat transfer per unit volume when compared with traditional compact parallel flow heat exchangers. Other advantages of tree-like flow networks as compared to parallel flow networks include lower total pressure drop as a consequence of pressure recovery at bifurcations as well as lower, more uniform, maximum wall temperatures.

Tuckerman and Pease [2.2] initially proposed the use of high-performance microchannel heat sinks with a high surface area for convective heat transfer per unit volume for the cooling of planar circuits. Tuckerman and Pease found microscale channels advantageous for laminar flow as the heat transfer coefficient scales inversely with channel width. West et al. [2.3-2.5] developed scaling laws for bulk fluid transport through space-filling fractal networks based on three assumptions: a tree-like branching network is required to supply an entire volume, the final branch level is size invariant, and the energy required to supply the flow network is minimized. Bau [2.6] found that the thermal resistance in flat plate micro heat exchangers can be minimized by optimizing the cross-sectional geometry of channels. Bau recommended employing tapered channels and concluded that the maximum wall temperature can be reduced by using non-uniform channel widths that vary in the axial direction. Bau also found decreasing channel widths in the axial direction resulted in an increase in velocity and thus an increase in pressure drop. Muwanga et al. [2.7] numerically investigated the effect of varying cross-sectional channel

geometry on the thermal performance of a radial microchannel heat exchanger. Muwanga et al. concluded that thermal performance improves by increasing channel-inlet area for a fixed channel-outlet area. Bejan [2.8, 2.9] found that tree-like flow networks are optimal for minimizing flow resistance and presented similar scaling ratios as defined by West et al. [2.3-2.5]. Murray [2.10] investigated the principle of minimum work in the vascular system and found there is an optimal change in hydraulic diameter at bifurcations in tree-like flow networks that minimizes flow resistance. This concept is known as Murray's law. Murray's law states that the cube of the radius of a parent branch equals the sum of the cubes of the radii of daughter branches. When Murray's law is obeyed, parent and daughter branches can be connected in a way that theoretically provides maximum bulk fluid transport for the least amount of work. A branching network that obeys Murray's law theoretically minimizes the flow resistance and thus pumping power required for fluid flow. Sherman [2.11], based on the work of Murray [2.10], concluded that when Murray's law is obeyed a functional relationship exists between channel diameters and various flow characteristics such as wall shear stress, velocity profile, and pressure gradient. Lee and Lee [2.12] measured six branching levels of the arterial bifurcations of chicken embryos and found the measured values closely approximated the theoretical values that Murray's law predicts. Lee and Lee also found that as the parent's diameter decreased the measured values more closely approached the theoretical values predicted by Murray's law. Lee and Lee attributed this trend to Murray's [2.10] use of Poiseuille's formula in his derivation.

Pence [2.13] compared a heat sink with a fractal-like flow network to a heat sink with a parallel channel flow network of equal surface area, pumping power, and flow rate. Pence found the fractal-like network resulted in lower total pressure drop and maximum wall temperature. Pence [2.13] developed a one-dimensional model for predicting the centerline pressure

distribution for the fractal-like flow network under hydrodynamically and thermally developing conditions using a correlation provided in White [2.14]. Pence also developed a one-dimensional model for predicting the wall surface temperature along the fractal-like flow network. Pence [2.15] compared a square shaped heat sink with a parallel channel flow network to a disk shaped heat sink with a fractal-like branching flow network of equal surface area for heat transfer and found the fractal-like flow network resulted in increased thermal efficiency. Pence concluded that for a constant heat flux boundary condition, a more uniform surface temperature and lower total pressure drop could be achieved by utilizing a fractal-like flow network. Pence and Enfield [2.16] compared a heat sink with a fractal-like flow network and a heat sink with a parallel channel flow network of equal surface area, applied heat flux, and inlet flow rate and concluded the fractal-like network resulted in a higher maximum wall temperature. It should be noted that Pence and Enfield [2.16] utilized a width scale ratio as an alternative to a diameter scale ratio due to fabrication constraints. Alharbi et al. [2.17] found that the one-dimensional model developed by Pence [2.13] should incorporate temperature dependent fluid properties as assuming constant fluid properties led to an overestimation of pressure drop. Alharbi et al. also found that fractal-like flow networks result in a lower total pressure drop when compared to parallel channel flow networks due to local pressure recovery at bifurcations that result from an increase in flow area. Alharbi et al. [2.18] similarly found that a fractal-like flow network resulted in a more uniform surface temperature when compared with a parallel channel flow network for the same maximum wall temperature. Wang et al. [2.19] found tree-like microchannel flow networks resulted in improved temperature uniformity when compared with parallel channel flow networks. Wang et al. [2.19, 2.20] also observed tree-like flow networks minimized the effect of channel blockage on fluid flow when compared with serpentine channel flow networks. Wang et al. [2.20] found

that an increased number of parent channels emanating from the center of a disk shaped heat sink and an increased number of branch levels resulted in increased temperature uniformity. Kobayashi et al. [2.21] utilized a biologically-inspired evolutionary method to model complex dendritic structures for a fixed area and subject to uniform heat generation and concluded that there is an optimal level of complexity after which thermal performance does not greatly improve.

Chen and Cheng [2.22] assessed the pressure drop and heat transfer capacity for a varying number of branch levels and diameter scale ratios while neglecting pressure recovery at bifurcations and assuming fully developed laminar flow. Chen and Cheng concluded a larger number of branch levels resulted in a higher heat transfer capability and lower total pressure drop. Chen and Cheng [2.23] experimentally confirmed that heat sinks with fractal-like flow networks are more thermally efficient than heat sinks with parallel channel flow networks for the same heat transfer rate, temperature difference, and inlet velocity. Enfield et al. [2.24] examined laminar mixing, which relies on molecular diffusion for mass transport, in microscale tree-like merging channel flow networks. Enfield et al. developed a numerical and experimental model for predicting concentration profiles and degree of mixing which allowed the optimal number of branch levels for a fixed initial parent channel width, total path length, and channel depth to be determined. Khan and Yovanich [2.25] incorporated first-order velocity slip and temperature jump boundary conditions in an analytical model of fluid flow thorough micro and nanochannel heat sinks and found that heat transfer increases and fluid friction decreases when compared with no-slip conditions. Senn and Poulikakos [2.26] found a tree-like branching flow network with six branch levels offered almost half the total pressure drop when compared with a serpentine flow pattern of equal surface area and inlet Reynolds number. Senn and Poulikakos also observed

secondary flow motions initiated at bifurcations. Senn and Poulikakos concluded transverse vortices created recirculation at bifurcations that resulted in hot spots at the inner corners of bifurcations and also observed longitudinal vortices resulted in enhanced thermal mixing and a decrease in the required flow rate for heat transfer. Muwanga and Hassan [2.27] presented flow and heat transfer characteristics for a cross-linked microchannel heat sink and observed a negligible difference in pressure drop measurements when compared with traditional parallel channel heat sinks. Wang et al. [2.28] found that the total pressure drop increased and hot spots became more noticeable as the bifurcation angle increased due to flow recirculation. Wang investigated 6 bifurcation angles ranging from 30° to 180° and found a bifurcation angle of 30° resulted in the lowest total pressure drop. Wang et al. [2.29] found asymmetrical leaf-like flow networks resulted in lower total pressure drop and higher average heat transfer coefficients than symmetric tree-like flow networks. Ghaedamini et al. [2.30] investigated the effect of channel svelteness on the bifurcation angle's role in pressure drop and flow uniformity. Ghaedamini et al. [2.30] concluded that as svelteness increases, flow uniformity increases and the effect of bifurcation angle on pressure drop decreases. Tree-like networks with a bifurcation angle of 30° were found to result in minimum pressure drop.

The purpose of this paper is to assess the effect of scaling on heat transfer and pressure drop for flow networks with hierarchical bifurcating flow passages. Fluid flow is laminar everywhere in microscale tree-like branching flow networks. In mesoscale flow networks viscous effects are not dominant everywhere as in microscale flow networks. A mesoscale biomimetic heat exchanger has the advantages of an increase in surface area for heat transfer as well as enhanced mixing due to the hierarchical bifurcating flow path. A mesoscale biomimetic heat exchanger potentially offers the advantages of lower pressure drop, improved thermal

efficiency, and increased temperature uniformity when compared to compact parallel flow heat exchangers.

Method of Analysis

The nomenclature and coordinate system describing the tree-like flow networks utilized in the present analysis can be seen in Figure 2.1.

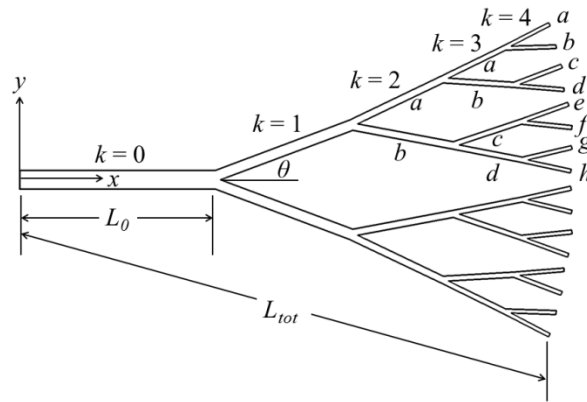


Figure 2.1. Nomenclature and Coordinate System for Branching Flow Networks

The first branch emanating from the inlet plenum is defined as the zeroth-order branch, where $k = 0$, and the last branch is defined as the fourth-order branch, where $k = 4$. The total length is defined as the radial distance between the entrance of the $k = 0$ branch and the exit of the $k = 4$ branch. The branch lengths are measured radially as seen in Figure 2.1. The total length is 16.30 mm for the microscale network and 163.0 mm for the mesoscale network. The flow network is asymmetric as the bifurcation angles are path-dependent. In order to characterize the asymmetric branching two different paths will be defined. Path 1 consists of the branch segments $k = 0, 1, 2a, 3a$, and $4a$. Path 2 consists of the branch segments, $k = 0, 1, 2b, 3c$, and $4f$. Paths 1 and 2 thus share the zeroth and first-order branch level.

The bifurcation angle is defined as the angle from which a higher level branch splits from a lower level branch. For example, the second order branch level, $k = 2$, splits from the first order

branch level, $k = 1$, at an angle of 5.17° along path 1 and 30.89° along path 2. Following West et al. [2.3] and Pence [2.13] the following branch scale ratios were utilized,

$$\beta = \frac{d_{k+1}}{d_k} = n^{-1/3} \quad (2.1)$$

$$\gamma = \frac{L_{k+1}}{L_k} = n^{-1/2} \quad (2.2)$$

For this analysis, $n = 2$ as each parent channel splits into 2 daughter channels. A daughter branch thus has a length that is $2^{-1/2}$ times shorter and a hydraulic diameter $2^{-1/3}$ times smaller than its parent branch. The hydraulic diameters scale in accordance with Murray's law and are thus connected in a way that theoretically provides bulk fluid transport for the least amount of work. The tree-like flow network employed in the present analysis is a scaled version similar to the microscale flow network employed by Alharbi et al. [2.17]. The bifurcation angles chosen in the present analysis are identical to those employed by Alharbi et al. [2.18]. The bifurcation angles utilized allow the effect of bifurcation angle on local pressure recovery at bifurcations, flow swirling after bifurcations, path-dependent mass flow distributions, bulk fluid exit temperatures, and path-dependent wall temperature distributions to be analyzed. The dimensions of the tree-like flow networks employed in the present analysis are provided in Table 2.1. A scaling factor of ten was applied to the microscale network to achieve the mesoscale network. The scaling factor was chosen so that the channel width of the fourth-order branch level, where $k = 4$, would be on the order of microscale. The scaled network is thus denoted as "mesoscale" in the present analysis. It should again be noted that branch segments $k = 3a$ and $k = 3d$ are not tapered as in [2.17].

Table 2.1. Channel Dimensions for Tree-Like

k	Microscale tree-like flow network				Mesoscale tree-like flow network				$\theta_{path 1}$ ($^{\circ}$)	$\theta_{path 2}$ ($^{\circ}$)
	H_k (mm)	w_k (mm)	d_k (mm)	L_k (mm)	H_k (mm)	w_k (mm)	d_k (mm)	L_k (mm)		
0	0.250	0.539	0.342	5.80	2.50	5.39	3.42	58.00	-	-
1	0.250	0.296	0.271	4.10	2.50	2.96	2.71	41.01	20.36	20.36
2	0.250	0.189	0.215	2.90	2.50	1.89	2.15	29.00	30.89	5.17
3	0.250	0.130	0.171	2.05	2.50	1.30	1.71	20.51	28.95	0.38
4	0.250	0.093	0.136	1.45	2.50	0.93	1.36	14.50	24.15	1.42

The fluid enters the tree-like flow network at the entrance of the $k = 0$ branch level and discharges at the exit of the $k = 4$ branch level. At the inlet of the $k = 0$ branch the fluid temperature is fixed and a uniform velocity profile is assumed. The velocity profile was assumed to be uniform as in Alharbi et al. [2.17]. The volumetric flow rate is 0.9 ml/s for the microscale flow network and 9.0 ml/s for the mesoscale flow network. The flow is assumed to be laminar only. The fluid exits the $k = 4$ branch level at environmental pressure. A uniform heat flux of 45 W/cm² is applied to all channel walls for both flow networks. The convective surface area for the microscale flow network is 57.16 mm² and 5716 mm² for the mesoscale flow network. The microscale flow network has a fluid volume of 3.08 mm³ and the mesoscale flow network has a fluid volume of 3080 mm³. The boundary conditions for the microscale and mesoscale tree-like flow networks are identical to the boundary conditions employed by Alharbi et al. [2.18]. The pressure drop across the tree-like flow network is defined as the static pressure difference between the fluid inlet at the entrance of the $k = 0$ branch and the fluid discharge at the exit of the $k = 4a$ branch.

Computational Model

The computational fluid dynamic simulations were performed using commercially available computational fluid dynamics software, employing the finite volume method. The

steady, incompressible form of the three-dimensional continuity, momentum, and energy equations are as follows:

$$\frac{\partial u_i}{\partial x_i} = 0 \quad (2.3)$$

$$\rho \frac{\partial(u_i u_j)}{\partial x_i} = \frac{\partial p}{\partial x_i} + \frac{\partial}{\partial x_i} \left(\mu \frac{\partial u_j}{\partial x_i} \right) \quad (2.4)$$

$$\rho \frac{\partial(u_i c_p T)}{\partial x_i} = \frac{\partial}{\partial x_i} \left(k \frac{\partial T}{\partial x_i} \right) \quad (2.5)$$

The Navier-Stokes equations are accompanied by fluid state equations which define the nature of the fluid as well as by empirical temperature dependencies of fluid properties [2.31]. Temperature dependent fluid properties were incorporated in the present analysis as recommended by Alharbi et al. [2.17]. The assumption of negligible buoyancy effects in the momentum equation was justified by confirming that the Grashoff number divided by the Reynolds squared was much less than 1 at all branch levels. The governing equations are solved with the finite volume method on a spatially rectangular computational mesh with the planes orthogonal to the Cartesian coordinate system axes and refined locally at the solid/fluid interface and in the fluid region. Basic mesh cells intersecting with the solid/fluid interface are split uniformly into smaller cells until a specified cell size is obtained. The mesh is further refined at the solid/fluid interface until the maximum angle between the normal to the surface inside a cell does not exceed a specified value. At the solid/fluid interface additional boundary faces and corresponding mass and heat fluxes that take into account boundary conditions and model geometry are introduced. The governing equations are discretized in a conservative form [2.32]. The numerical model is spatially second-order accurate. The governing equations are integrated over a control volume and then approximated with cell-centered values of the basic variables [2.33]. Second-order upwind approximations of fluxes are based on the implicitly treated

modified Leonard's QUICK [2.34] approximations and the Total Variation Diminishing [2.35] method. An elliptic type discrete pressure equation is derived by algebraic transformations of the derived discrete governing equations and incorporates velocity boundary conditions using the SIMPLE-like [2.36] method. Localized numerical errors at the inner corners of bifurcations for temperature, velocity magnitude, and pressure are on the order of 0.1 K, 0.006 m/s, and 0.2 Pa respectively.

Validation and Verification

Pence [2.13] developed a one-dimensional model for predicting the centerline pressure distribution along rectangular cross-section ducts for hydrodynamically and thermally developing flow based on a correlation developed in White [2.14]. Pence's model, for laminar flow, had three main assumptions: the thermal and hydrodynamic boundary layers instantaneously redevelop after each bifurcation, minor losses, and thus local pressure recovery at bifurcations are neglected, and thermophysical properties are independent of temperature. The pressure distribution was found numerically assuming atmospheric pressure at the exit using the following correlation [2.13, 2.14],

$$p_i = p_{i+1} + \frac{1}{2} \rho u^2 c_{f,app} \frac{4\Delta x}{d} \quad (2.6)$$

The working fluid was water and fluid properties were evaluated at 293 K. The microscale flow network had an inlet flow rate of 0.9 ml/s which corresponded to a Reynolds number on the order of 2000. Results of the one-dimensional model developed by Pence [2.13], and employed by Alharbi et al. [2.17], can be seen in Figure 2.2. The microscale fractal-like flow network employed by Alharbi et al. [2.17] utilizes different bifurcation angles than the fractal-like flow network employed by Alharbi et al. [2.18] and in the present analysis. The one-dimensional predictive model developed by Pence [2.13] was validated for design purposes by

Alharbi et al. [2.17]. Alharbi et al. [2.17] noted that the discrepancy in pressure drop was primarily the result of local pressure recovery at bifurcations and also recommended including temperature dependent properties for high heat flux applications. The assumption that the hydrodynamic boundary layer redeveloped following bifurcations in the one-dimensional model also contributed to the overestimation of total pressure drop. The geometry of the three-dimensional computational fluid dynamics model employed by Alharbi et al. [2.18] was reconstructed as a means of assessing the effect of scaling on heat transfer and fluid flow in flow networks with hierarchical bifurcating flow passages.

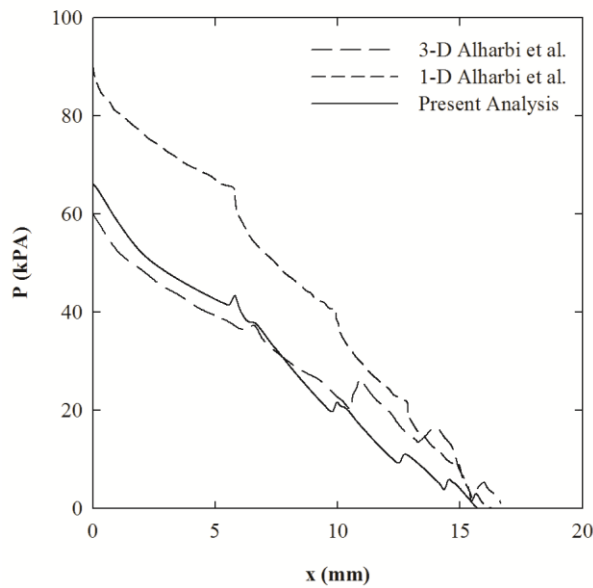


Figure 2.2. Three-Dimensional Computational Model Validation

There is a slight difference in the axial distance for the three-dimensional models attributed to the definition of the path length utilized in the present analysis. Local pressure recovery at bifurcations can be seen in Figure 2.2 for the three-dimensional model utilized in the present analysis as well as the three-dimensional model employed by Alharbi et al. [2.18]. The three-dimensional microscale fractal-like flow network employed by Alharbi et al. [2.17] yielded

a total pressure drop of 63 kPa while the microscale model employed in the present analysis had a total pressure drop of 66 kPa, a 4.76 % difference. The three-dimensional model in the present analysis exhibits similar magnitudes of local pressure recovery at the first and second bifurcation. The difference in the mid-depth centerline pressure distribution between the two models becomes much more pronounced at the third branch level. The difference in the mid-depth centerline pressure distribution is partially attributed to the tapering of the channels recommended by Bau [2.6] and employed by Alharbi et al. [2.17, 2.18] at branch segments $k = 3a$ and $k = 3d$. As previously mentioned, Bau [2.6] found that non-uniform channel widths reduce maximum wall temperatures and increase temperature uniformity. The channels in the present analysis were not tapered due to a lack of information defining the geometry of the flow network used in Alharbi et al [2.17]. The three-dimensional computational model employed by Alharbi et al. [2.17, 2.18] was validated experimentally in [2.17]. The three-dimensional computational model utilized in the present analysis, which is in good agreement with the model employed by Alharbi et al. [2.17], is thus assumed to be validated. The number of cells in the three-dimensional computational model of the microscale tree-like flow network was successively doubled until grid independence was achieved. The grid was refined seven times. The three-dimensional computational mesh consisted of approximately 2,000,000 fluid cells and 1,000,000 partial cells. Partial cells are defined at the solid/fluid interface. The use of approximately 3,000,000 cells, which corresponded to the fifth level of refinement, proved to be sufficient for the analysis.

The tree-like flow network employed in the present analysis was also validated with the experimental data provided by Apreotesi [2.37] for two different fractal-like heat sinks as well as with the results from the three-dimensional fractal heat sink model detailed by Alharbi et al.

[2.18]. The results can be seen in Figure 2.3. The three-dimensional heat sink model utilized for validation in the present analysis consists of 12 branching flow networks (please refer to Figure 2.1) revolved radially to share a single inlet plenum. The 12 flow networks were embedded in a circular copper heat sink with a radius of 18 mm and a thickness of 2 mm. A uniform heat flux of 45 W/cm^2 was applied to the bottom of the heat sink. It should be noted that it would be desirable for the heat source to be located adjacent to the highest order branch level in a disk shaped heat sink as that is where the most surface area available for heat transfer is located. However, Pence [2.15] and Alharbi et al. [2.18] concluded that fractal-like disk shaped heat sinks offer the advantage of increased surface temperature uniformity when compared with rectangular parallel channel heat sinks. The three-dimensional model utilized in the present analysis incorporated an inlet plenum as detailed by Apreotesi [2.37]. A uniform velocity profile was assumed at the inlet plenum. The working fluid, water, was assumed to enter the inlet plenum at a temperature of 293 K and exit the fourth-order branch level at atmospheric pressure. Temperature dependent fluid properties were incorporated in the heat sink model. The number of cells in the three-dimensional computational model of the heat sink was successfully doubled until grid independence was achieved. The grid was refined seven times. The three-dimensional computational mesh consisted of approximately 2,000,000 fluid cells and 1,000,000 partial cells. The use of approximately 3,000,000 cells, which corresponded to the fifth level of refinement, proved to be sufficient for the analysis.

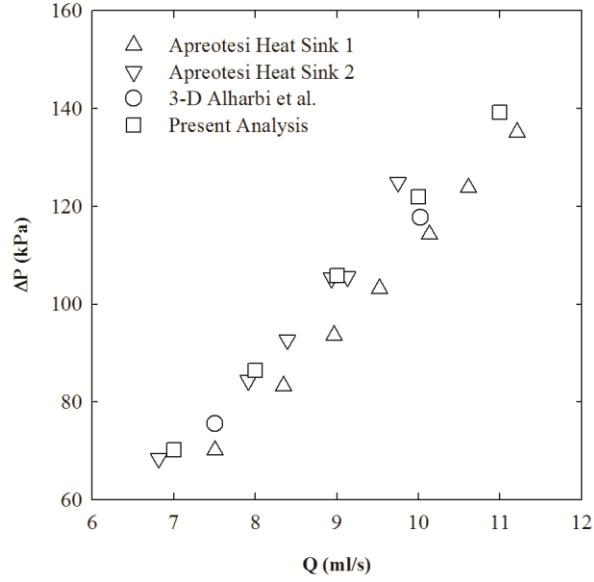


Figure 2.3. Three-Dimensional Computational Model Validation with Experimental Results

As an additional means of validation, a model was created of the zeroth-order branch level of the microscale tree-like flow network previously employed. The nomenclature describing the model can be seen in Figure. 2.4.

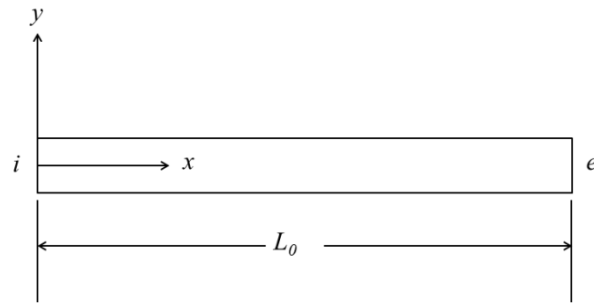


Figure 2.4. Nomenclature and Coordinate System for Single Channel

The dimensions for the computational model can be seen in Table 2.2.

Table 2.2. Channel Dimensions for Zeroth-Order Branch

H (mm)	w (mm)	d (mm)	L (mm)
0.250	0.539	0.342	5.80

The fluid enters the channel at the entrance of the $k = 0$ branch level and discharges at the exit of the $k = 0$ branch. At the inlet of the $k = 0$ branch the fluid temperature was fixed and a fully developed velocity profile was assumed. The volumetric flow rate was 0.9 ml/s. The flow was assumed to be laminar only. The fluid exits the $k = 0$ branch level at environmental pressure. A uniform heat flux of 45 W/cm² was applied to all channel walls. The pressure drop across the channel is defined as the static pressure difference between the fluid inlet at the entrance of the $k = 0$ branch and the fluid discharge at the exit of the $k = 0$ branch.

Bahrami et al. [2.38] developed a model for predicting pressure drop of fully developed, laminar, incompressible flow in microchannels of arbitrary cross-section. The computational model consists of the zeroth-order branch level of the microscale tree-like flow network previously employed and was compared to the pressure drop model developed by Bahrami et al. [2.38] The aspect ratio is defined as,

$$\varepsilon = \frac{H}{w} \quad (2.7)$$

The polar moment of inertia for a rectangular cross-section is defined as,

$$I_p^* = \frac{1+\varepsilon^2}{12\varepsilon} \quad (2.8)$$

The pressure drop across the channel, as defined by Bahrami et al. [2.38], is as follows,

$$\Delta p = \frac{16\pi^2 \mu u}{A} I_p^* L \quad (2.9)$$

The model developed by Bahrabi et al. [2.38] predicted a total pressure drop of 9.53 kPa while the computational model employed in the present analysis resulted in a total pressure drop of 9.72 kPa, a 2.06 % difference. The number of cells in the three-dimensional computational model of the zeroth-order branch level of the microscale tree-like flow network was successively doubled until grid independence was achieved. The grid was refined seven times. The three-dimensional computational mesh consisted of approximately 50,000 fluid cells and 20,000 partial cells at the interface of the solid and fluid. The use of approximately 70,000 cells, which corresponded to the fifth level of refinement, proved to be sufficient for the analysis.

Results and Discussions

As previously mentioned, Path 1 consists of the branch segments $k = 1, 2a, 3a,$ and $4a$. Path 2 consists of the branch segments, $k = 1, 2b, 3c,$ and $4f$. The mid-depth centerline pressure distribution along paths 1 and 2 (refer once again to Figure 2.1) for the microscale and mesoscale tree-like flow networks can be seen in Figure 2.5. Results are presented for an inlet volumetric flow rate of 0.9 ml/s, an inlet fluid temperature of 293 K, and a surface heat flux of 45 W/cm^2 for the microscale flow network. The mesoscale flow network had an inlet volumetric flow rate of 9.0 ml/s. The flow networks exhibit similar flow behavior at bifurcations where local pressure recovery can be observed. For example, the microscale flow network has a 2.7 kPa pressure recovery at the first bifurcation. The mesoscale flow network has a 22.0 Pa pressure recovery at the first bifurcation. The local pressure recovery is a consequence of secondary flow conditions that result from increased cross-sectional areas at bifurcations and subsequent flow deceleration. The microscale and mesoscale flow networks exhibit greater local pressure recovery along path 1 where the bifurcation angles are smaller which is in good agreement with the microscale flow

network studied by Wang et al. [2.28]. The microscale flow network had a total pressure drop of 66.18 kPa while the mesoscale flow network had a total pressure drop of 0.42 kPa.

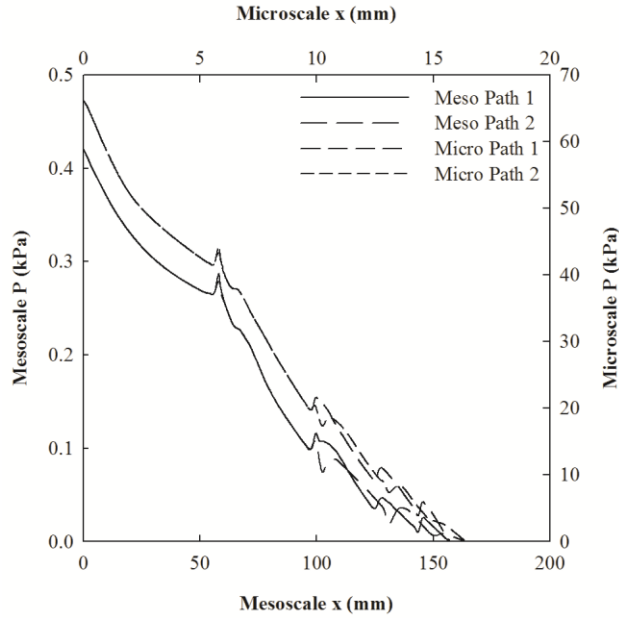


Figure 2.5. Centerline Pressure Distributions

The results were cast in dimensionless form as recommended in [2.39] for ease of scaling comparison. The non-dimensional axial distance is defined as,

$$X = \frac{x}{L_{tot}} \quad (2.10)$$

The Euler number is the ratio of pressure to inertia forces and is defined as,

$$Eu = \frac{\Delta p}{\rho u^2} \quad (2.11)$$

The pressure difference term is defined as the difference between the static pressure along the centerline and environmental pressure at the exit. Similarly, the velocity term is the average fluid velocity along the centerline. The non-dimensional mid-depth centerline pressure distribution along paths 1 and 2 for the microscale and mesoscale flow networks can be seen in Figure 2.6. The microscale and mesoscale flow networks show the greatest local pressure recovery at the first bifurcation along paths 1 and 2. The microscale flow network shows greater

local pressure recovery when compared to the mesoscale flow network at all bifurcations along paths 1 and 2.

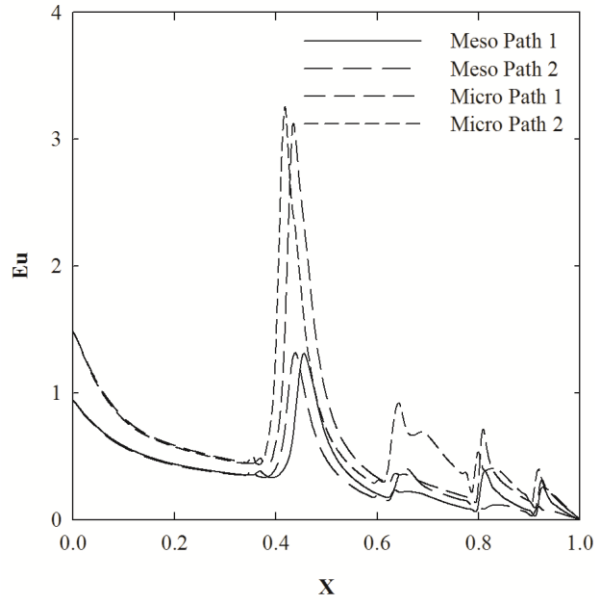


Figure 2.6. Centerline Euler Number Distributions

The Reynolds number is the ratio of inertia to viscous forces and is defined as,

$$\text{Re} = \frac{ud}{\nu} \quad (2.12)$$

The velocity term is the average fluid velocity along the centerline and the hydraulic diameter term is branch level dependent. The mid-depth centerline Reynolds number distributions along paths 1 and 2 for the microscale and mesoscale flow networks can be seen in Figure 2.7. The microscale and mesoscale networks exhibit qualitatively similar behavior at all bifurcations but the first where the mesoscale flow network has an increase in the average mid-depth centerline fluid velocity. The step changes in the Reynolds number distributions correspond to changes in hydraulic diameter as the flow bifurcates from a lower to a higher order branch level.

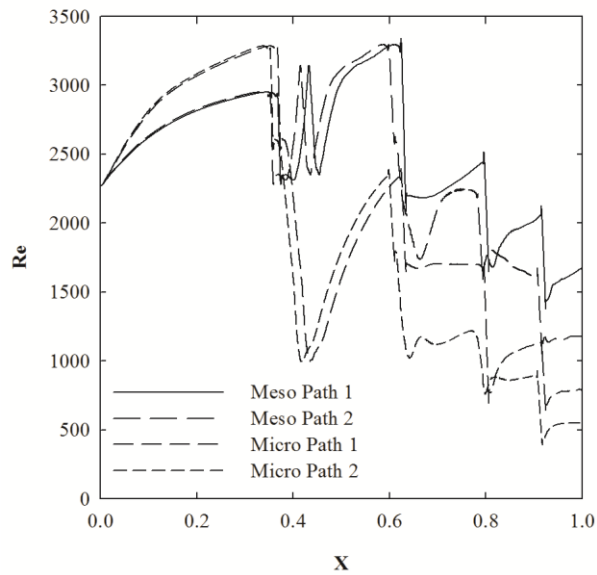


Figure 2.7. Centerline Reynolds Number Distributions

Flow behavior is highly dependent on the path taken due to the asymmetric nature of the flow networks. The flow separates symmetrically at the first bifurcation between the zeroth-order branch and the first-order branch. The flow divides asymmetrically at all subsequent bifurcations. Mid-depth velocity magnitude isolines at the first and second bifurcation can be seen in Figures 2.8, 2.9 for the microscale flow network. The mesoscale flow network's velocity isolines are not presented as they are qualitatively similar to the microscale flow network's isolines. As can be seen in Figures 2.8 and 2.9 flow separation is highly dependent on bifurcation angle. It can also be observed that hydrodynamic boundary layers do not fully redevelop downstream of bifurcations under the conditions considered.

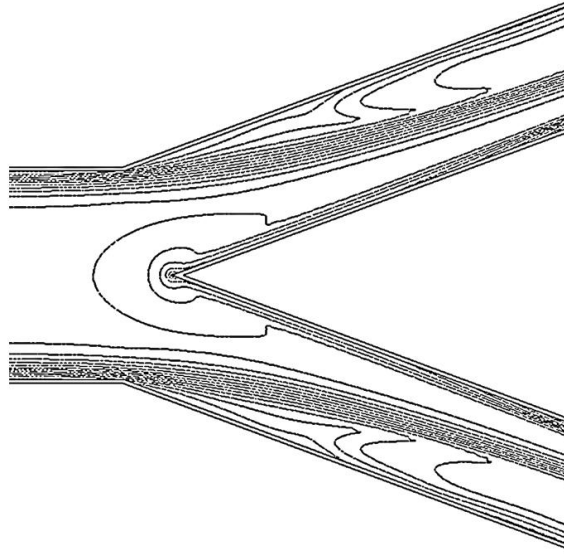


Figure 2.8. Mid-Depth Fluid Velocity Isolines at the First Bifurcation

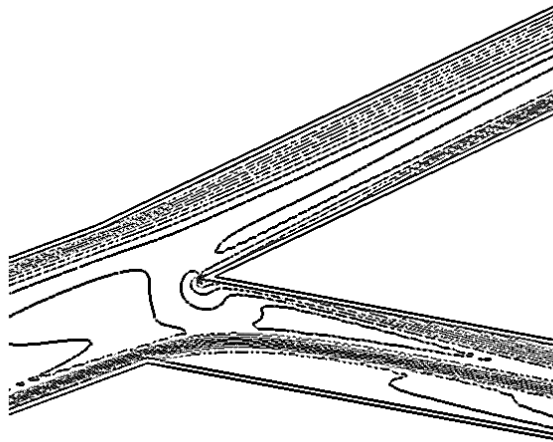


Figure 2.9. Mid-Depth Fluid Velocity Isolines at the Second Bifurcation

The asymmetry of the flow networks also lead to mass flow rates that are path dependent. The mass flow rate at the exit of the $k = 4a$ branch is 0.0698 g/s and at the exit of the $k = 4f$ branch is 0.0462 g/s for the microscale network. The mass flow rate through path 1 is

approximately 1.5 times larger than the mass flow rate through path 2. The mass flow rates were non-dimensionalized as follows,

$$M = \frac{\dot{m}_e}{\dot{m}_i} \quad (2.13)$$

The mass flow rate ratio is defined as the mass flow rate at the exit divided by the inlet mass flow rate. The non-dimensional mass flow rates at the exit of the $k = 4$ branch can be seen in Figure 2.10 and are in good agreement with the results for the microscale flow network employed by Wang et al. [2.28]. The outlet positions 1, 2, 3, 4, 5, 6, 7, and 8 in Figure 2.10 correspond to the outlet positions a, b, c, d, e, f, g, and h in Figure 2.1.

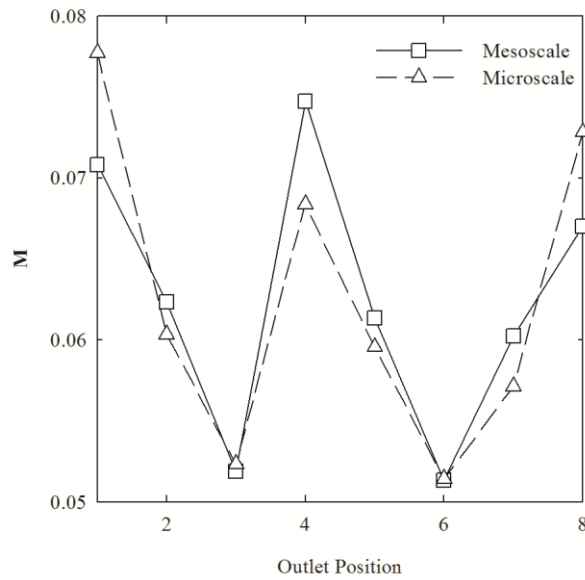


Figure 2.10. Mass Flow Distribution at Outlets

The bulk fluid exit temperature is lower along path 1 when compared with path 2 due to the higher mass flow rate. For the microscale flow network the bulk fluid temperature at the exit of the $k = 4a$ branch is 299.0 K and at the exit of the $k = 4f$ branch is 300.9 K. The average bulk fluid exit temperature for the microscale flow network is 299.8 K. For the mesoscale flow

network the bulk fluid temperature at the exit of the $k = 4a$ branch is 358.8 K and at the exit of the $k = 4f$ branch is 371.1 K. The average bulk fluid exit temperature for the mesoscale flow network is 359.9 K. The non-dimensional mass flow rate ratios and bulk fluid exit temperatures for the microscale and mesoscale networks can be seen in Table 2.3. The average bulk fluid exit temperature was 6.8 K higher than the inlet fluid temperature for the microscale flow network and 67.4 K higher for the mesoscale flow network.

Table 2.3. Mass Flow Rate Ratios and Bulk Fluid Exit Temperatures

k	Microscale		Mesoscale	
	M	$T_{b,e}$ (K)	M	$T_{b,e}$ (K)
0	1.000	293.0	1.000	293.0
4a	0.078	299.0	0.071	358.8
4b	0.060	299.1	0.062	355.7
4c	0.052	300.0	0.052	361.3
4d	0.068	299.2	0.075	351.6
4e	0.060	300.3	0.061	358.9
4f	0.051	300.9	0.051	371.1
4g	0.057	300.5	0.060	369.7
4h	0.073	299.6	0.067	365.4

The asymmetry of the tree-like flow network employed by Alharbi et al. [2.18] and subsequently scaled in the present analysis similarly results in wall temperature distributions that are path dependent. The nomenclature describing what constitutes an inner, outer wall, and top wall can be seen in Figure 2.11. It should be noted that wall temperature distributions along the inner wall will inherently be discontinuous due to the definition of what constitutes an inner wall (refer once again to Figure 2.11).

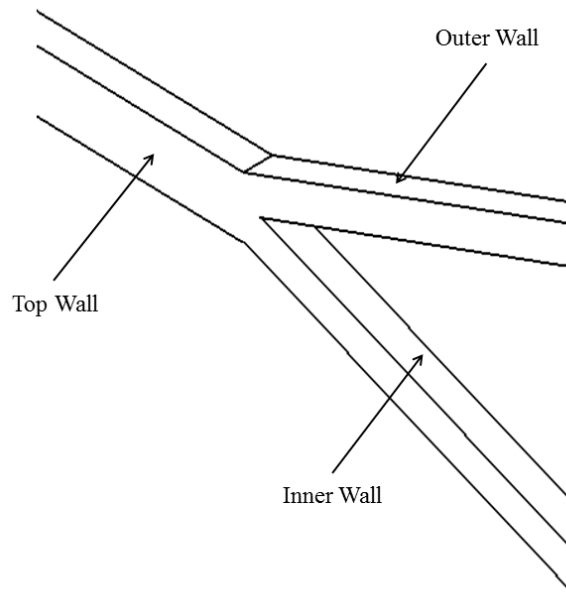


Figure 2.11. Nomenclature for Wall Temperature Distributions

The mid-depth inner and bottom wall temperature distribution along paths 1 and 2 for the microscale and mesoscale tree-like flow networks can be seen in Figures. 2.12-2.13.

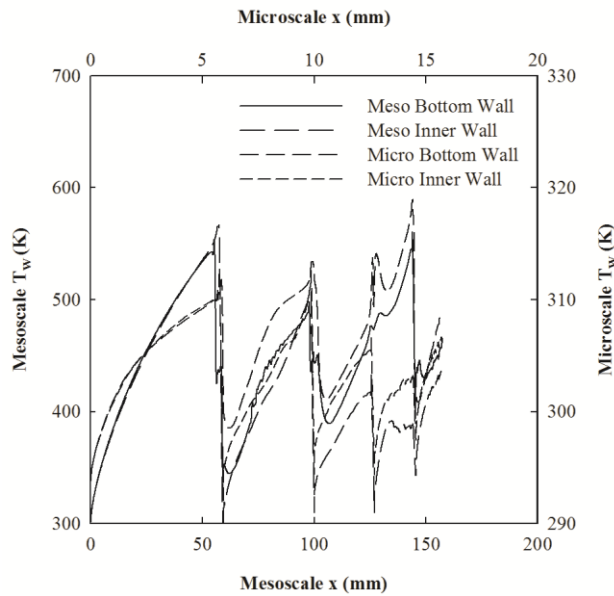


Figure 2.12. Wall Temperature Distributions along Path 1

Due to flow separation following bifurcations where a zone of recirculating fluid is present at the outer wall, temperature distributions will be addressed independently. The wall temperature distribution for the top and bottom walls was found to be almost identical as expected due to the constant channel height. As such, wall temperature distributions are presented for the bottom wall only.

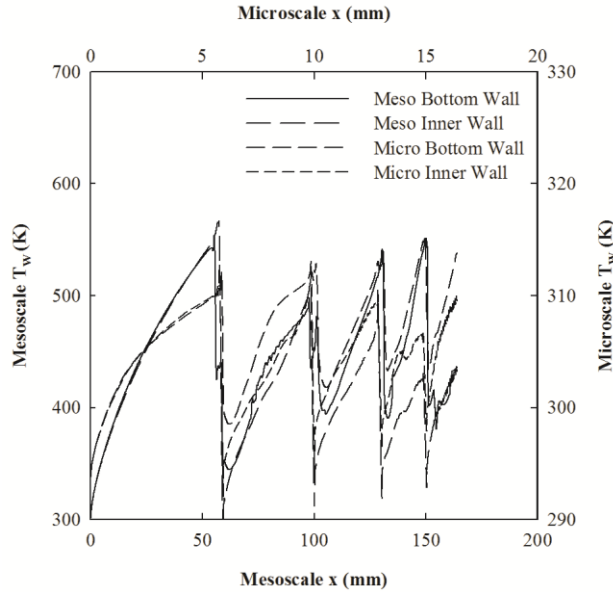


Figure 2.13. Wall Temperature Distributions along Path 2

As previously mentioned, path 2 has a lower mass flow rate and a longer total path length which results in a higher inner wall temperature at the exit of path 2 when compared with path 1. The inner wall temperature at the exit of path 1 is 306.6 K and at the exit of path 2 is 309.5 K for the microscale flow network. Temperature spikes at the inner corner of bifurcations can be observed in good agreement with Senn and Poulikakos [2.26]. The top and bottom walls have temperature spikes at bifurcations due to increased cross-sectional areas and subsequent flow deceleration. The maximum inner wall temperatures along path 2 are greater than that of path 1. For the microscale flow network the inner wall of the $k = 2a$ branch has a maximum temperature

of 311.9 K while the inner wall of the $k = 2b$ branch has a maximum temperature of 313.7 K. Similarly, for the mesoscale flow network the inner wall of the $k = 2a$ branch has a maximum temperature of 470.5 K while the outer wall of the $k = 2b$ branch has a maximum temperature of 525.88 K.

The Nusselt number is the ratio of convection to conduction heat transfer and is defined as,

$$\text{Nu} = \frac{hx}{k} \quad (2.14)$$

The inner and bottom wall Nusselt number distributions along the inner and bottom walls of paths 1 and 2 for the microscale and mesoscale flow networks can be seen in Figures 2.14, 2.15. The microscale and mesoscale flow networks exhibit qualitatively and quantitatively similar inner and bottom wall Nusselt number distributions along paths 1 and 2. Inner wall Nusselt numbers were found to spike at the corners of bifurcations as a result of large increases in the heat transfer coefficient and the discontinuous nature of the inner wall.

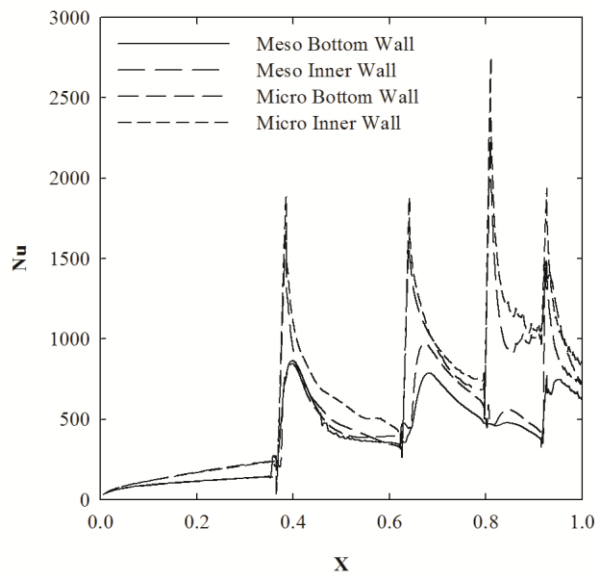


Figure 2.14. Inner and Bottom Wall Nusselt Number Distributions along Path 1

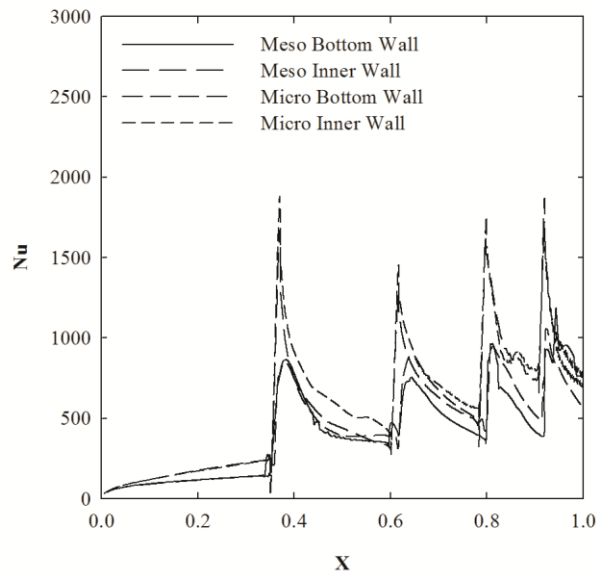


Figure 2.15. Inner and Bottom Wall Nusselt Number Distributions along Path 2

The outer wall temperature distributions are significantly different than the inner wall temperature distributions due to flow behavior at bifurcations. Immediately after each bifurcation the outer wall temperature increases significantly as a result of flow separation. The flow separation causes a zone of recirculating fluid which is followed by a downstream decrease in temperature. For example at the first bifurcation of the microscale flow network the temperature spikes approximately 11 K. The flow swirling that occurs following the first and second bifurcation in the microscale flow network can be seen in Figures 2.16, 2.17. The level of flow swirling is highly path dependent as can be seen in Figure 2.17 where the flow bifurcates at an angle of 5.17° along path 1 and 30.89° along path 2. The flow swirling results in higher heat transfer coefficients at the inner walls immediately following bifurcations.

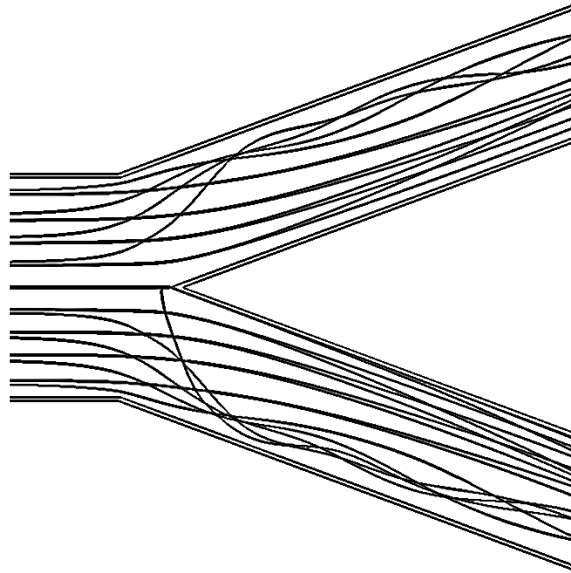


Figure 2.16. Flow Trajectories at the First Bifurcation

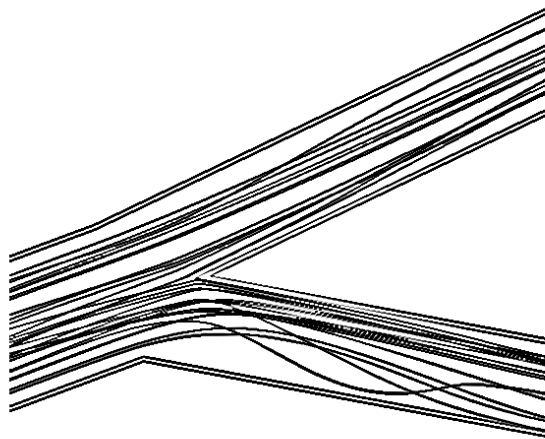


Figure 2.17. Flow Trajectories at the Second Bifurcation

The mesoscale flow network exhibits outer wall temperature behavior that is not qualitatively different than the microscale flow network along path 1. Along path 2 the mesoscale flow network exhibits larger temperature spikes following bifurcations. The temperature spikes are considerably more pronounced along path 2 where the bifurcation angles

are larger. The outer wall temperature distributions along paths 1 and 2 for the microscale and mesoscale flow networks can be seen in Figures 2.18, 2.19.

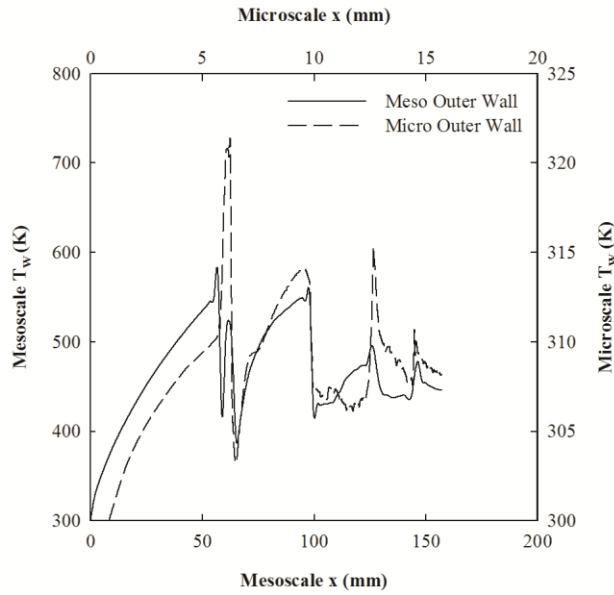


Figure 2.18. Outer Wall Temperature Distributions along Path 1

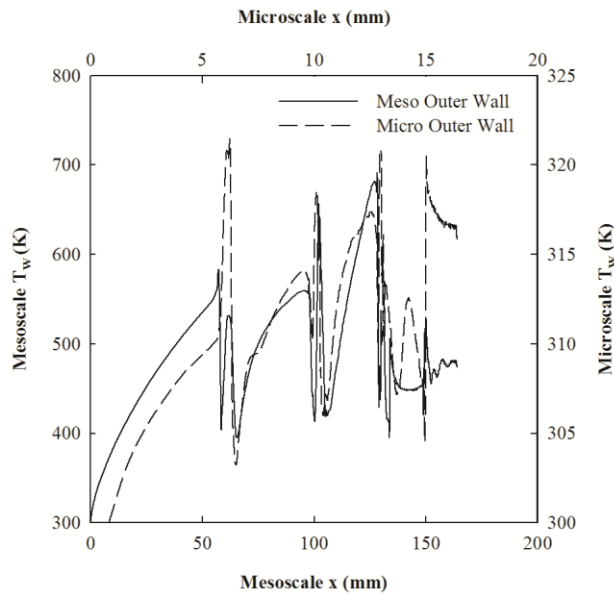


Figure 2.19. Outer Wall Temperature Distributions along Path 2

Outer wall Nusselt number distributions along paths 1 and 2 for the microscale and mesoscale flow networks can be seen in Figures 2.20, 2.21. Spikes in the heat transfer

coefficient, and subsequently Nusselt number, are more prominent along path 2 where the bifurcation angles are larger. While the microscale and mesoscale flow networks exhibit qualitatively similar outer wall Nusselt number distributions the mesoscale network resulted in lower outer wall Nusselt numbers along paths 1 and 2.

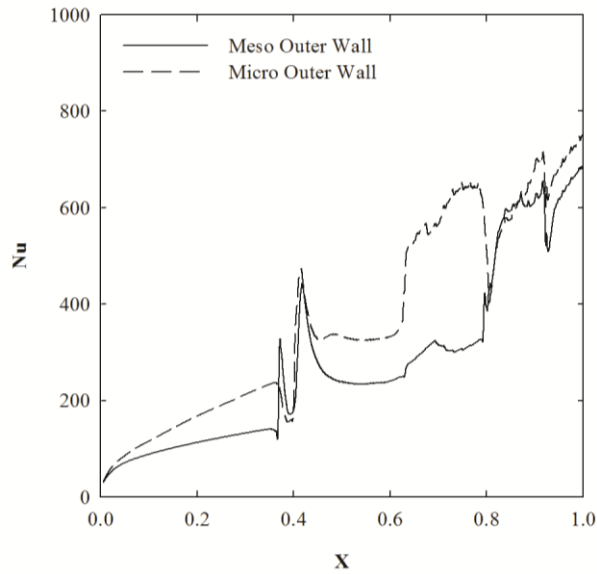


Figure 2.20. Outer Wall Nusselt Number Distributions along Path 1

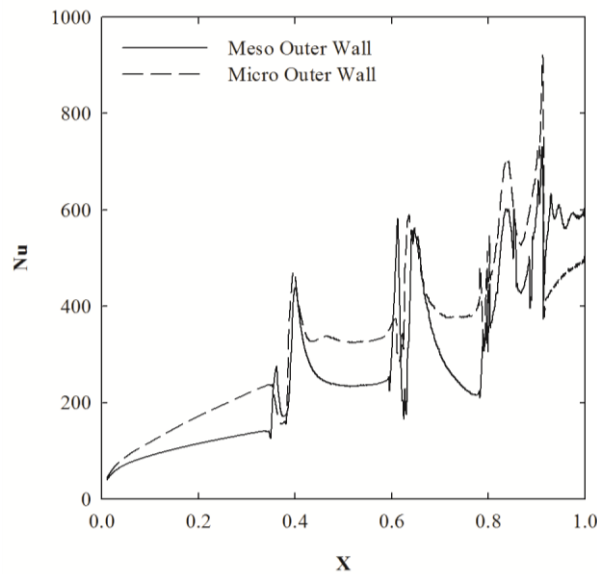


Figure 2.21. Outer Wall Nusselt Number Distributions along Path 2

Mid-depth fluid temperature isolines at the first and second bifurcation can be seen in Figures 2.22, 2.23 for the microscale flow network. The mesoscale flow network is not represented as the temperature isolines are not qualitatively different from the microscale flow network at the first two bifurcations. As previously mentioned, the highest wall temperatures are located immediately after bifurcations due to flow separation. The maximum wall temperatures along path 2 are greater than the wall temperatures along path 1. The microscale flow network for example, the outer wall of the $k = 2a$ branch has a maximum temperature of 318.5 K while the outer wall of the $k = 2b$ branch has a maximum temperature of 322.0 K. Similarly, for the mesoscale flow network the outer wall of the $k = 2a$ branch has a maximum temperature of 575.8 K while the outer wall of the $k = 2b$ branch has a maximum temperature of 821.9 K.

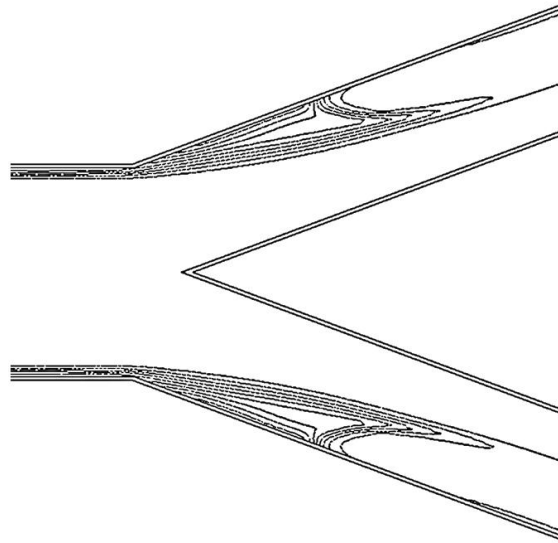


Figure 2.22. Mid-Depth Fluid Temperature Isolines at the First Bifurcation

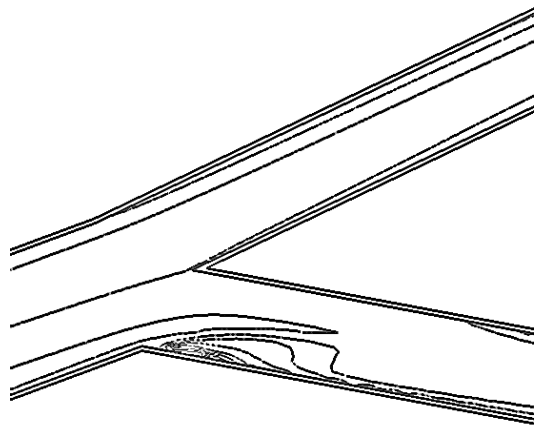


Figure 2.23. Mid-Depth Fluid Temperature Isolines at the Second Bifurcation

Flow separation should be minimized in order to increase wall temperature uniformity. Maximum inner and outer wall temperatures for the microscale and mesoscale flow networks are higher along path 2 where the bifurcations angles are larger. Flow separation can be minimized by decreasing bifurcation angles which results in increased temperature uniformity as well as increased local pressure recovery and thus lower total pressure drop.

Branch level performance characteristics for the microscale and mesoscale flow networks can be seen in Table 2.4. The Nusselt numbers presented are an average of the top, bottom, inner, and outer walls at each branch level. The Reynolds and Euler numbers presented are an average along the mid-depth centerline of each branch level.

Table 2.4. Branch Level Performance Characteristics

Branch Level	Nusselt Number		Reynolds Number		Euler Number	
	Micro	Meso	Micro	Meso	Micro	Meso
0	139	107	2951	2732	0.71	0.51
1	428	414	1829	2899	1.02	0.52
2	558	557	1446	2194	0.42	0.20
3	788	799	947	1808	0.31	0.13
4	764	776	646	1372	0.15	0.07

In order to better characterize the microscale and mesoscale flow networks in relation to traditionally employed compact heat exchangers several performance characteristics will be utilized as detailed by Kays and London [2.39]. In the following calculations fluid properties were taken at 293 K and assumed to be constant. The heat transfer coefficient was calculated by dividing the uniform heat flux applied to the periphery of all channels walls divided by the bulk fluid temperature increase across the branching flow network in consideration. The characteristic length for the flow network was defined as the square root of the surface area available for heat transfer. The Nusselt number can thus defined as follows,

$$\text{Nu} = \frac{hL_c}{k} \quad (2.15)$$

The Stanton number is the ratio of the heat transferred to the fluid to the heat exported by the fluid and is defined as,

$$\text{St} = \frac{h}{\rho c_p u_i} \quad (2.16)$$

The Prandtl number is the ratio of momentum to thermal diffusivity and was assumed to be constant. Two traditionally employed performance characteristics that describe compact heat exchangers are the Colburn factor and the friction factor. The Colburn factor is defined as follows,

$$j = \text{St} \cdot \text{Pr}^{2/3} \quad (2.17)$$

The final performance characteristic, the friction factor is defined as,

$$f = \frac{d_0}{L_c} 2\rho \frac{\Delta p}{4G^2} \quad (2.18)$$

A summary of the overall performance characteristics for the microscale and mesoscale branching flow networks can be seen in Table 2.5. The Reynolds and Euler numbers presented are defined at the inlet of the branching flow networks.

Table 2.5. Flow Network Performance Characteristics

	Re	Eu	Nu	St	j	f
Microscale	2272	1.49	826	0.00237	0.00853	0.0337
Mesoscale	2272	0.94	833	0.00239	0.00861	0.0214

As can be seen in Table 2.5 the use of biological inspiration in the design of flow networks is applicable in microscale as well as mesoscale. The microscale and mesoscale flow networks offer similar thermal performance while the mesoscale flow network has the additional advantage of reduced pressure drop.

Conclusions

A computational model has been developed to study the effects of scaling on a microscale tree-like flow network's fluid flow and heat transfer characteristics. A mesoscale model, with fourth-order branch channel widths on the order of microscale, was created to observe these effects. Results were cast in terms of commonly defined dimensionless parameters that allow the branching flow networks to be compared to traditional compact heat exchangers. Mesoscale tree-like flow networks exhibit qualitatively similar centerline pressure and wall temperature distributions as microscale tree-like flow networks under the conditions studied. While the microscale flow network had two orders of magnitude greater local pressure recovery at bifurcations the benefit of local pressure recovery at bifurcations is still present in the mesoscale flow network. The microscale flow network studied had a total pressure drop two orders of magnitude greater than the mesoscale flow network. Bifurcation angles, at all scales,

have a significant impact on local pressure recovery and wall temperature distributions due to flow separation and zones of recirculation. Wall temperature uniformity can be increased by minimizing flow separation that results in hot spots at walls immediately downstream of bifurcations. Flow separation results in outer walls with higher maximum wall temperatures when compared with inner walls. The microscale and mesoscale flow networks exhibit similar thermal performance at all branch levels. The mesoscale flow network had an order of magnitude larger increase in bulk fluid temperature across the flow network. Knowledge obtained when studying microscale tree-like flow networks can be utilized in the design of mesoscale tree-like flow networks.

Acknowledgments

Portions of this work were funded by The University of Alabama GK-12 Program. The GK-12 Program is supported by the National Science Foundation under grant 0742504.

References

- [2.1] Mandelbrot, B. B., 1982, *The Fractal Geometry of Nature*, Freeman, New York.
- [2.2] Tuckerman, B. B., and Pease, R. F. W., 1981, "High-Performance Heat Sinking for VLSI," *IEEE Electron Device Letters*, 2(5), pp. 126-129.
- [2.3] West, G. B., Brown, J. H., and Enquist, B. J., 1997, "A General Model for the Origin of Allometric Scaling Laws in Biology," *Science*, 276, pp. 122-126.
- [2.4] West, G. B., Brown, J. H., and Enquist, B. J., 1999, "The Fourth Dimension of Life: Fractal Geometry and Allometric Scaling of Organisms," *Science*, 284, pp. 1677-1679.
- [2.5] West, G. B., 1999, "The Origin of Universal Scaling Laws in Biology," *Physica A*, 263, pp. 104-113.
- [2.6] Bau, H. H., 1998, "Optimization of Conduits' Shape in Micro Heat Exchangers," *International Journal of Heat and Mass Transfer*, 41(18), pp. 2717-2723.
- [2.7] Muwanga, R., Hassan, I., and Ghorab, A., 2008, "Numerical Investigation of a Radial Microchannel Heat Exchanger with Varying Cross-Sectional Channels," *Journal of Thermophysics and Heat Transfer*, 22(3), pp. 321-332.
- [2.8] Bejan, A., 1997, "Constructal-Theory Network of Conducting Paths for Cooling a Heat Generating Volume," *International Journal of Heat and Mass Transfer*, 40(4), pp. 799-816.
- [2.9] Bejan, A., 1997, "Constructal Tree Network for Fluid Flow between a Finite-Size Volume and One Source or Sink," *Revue Generale de Thermique*, 36(8), pp. 592-604.
- [2.10] Murray, C. D., 1926, "The Physiological Principle of Minimum Work. I. The Vascular System and the Cost of Blood Volume," *Journal of Physiology*, 12(3), pp. 207-214.
- [2.11] Sherman, T. F., 1997, "The Meaning of Murray's Law," *Journal of General Physiology*, 78, pp. 431-453.
- [2.12] Lee, J. Y., and Lee, S. J., 2010, "Murray's Law and the Bifurcation Angle in the Arterial Micro-Circulation System and Their Application to the Design of Microfluidics," *Journal of Microfluidics and Nanofluidics*, 8(1), pp. 85-95.
- [2.13] Pence, D. V., 2002, "Reduced Pumping Power and Wall Temperature in Microchannel Heat Sinks with Fractal-Like Branching Channel Networks," *Microscale Thermophysical Engineering*, 6, pp. 319-330.
- [2.14] White, F. M., 1991, *Viscous Fluid Flow*, 2nd ed., McGraw-Hill, New York, pp. 291-293.

- [2.15] Pence, D. V., 2000, "Improved Thermal Efficiency and Temperature Uniformity Using Fractal-Like Branching Channel Networks," Proc. International Conference on Heat Transfer and Transport Phenomena in Microscale, edited by G. P. Celesta, New York, pp. 142-148.
- [2.16] Pence, D. V., and Enfield, K. E., 2004, "Inherent Benefits in Microscale Fractal-Like Devices for Enhanced Transport Phenomena," Design and Nature II, WIT Press, Boston, pp. 317-327.
- [2.17] Alharbi, A. Y., Pence, D. V., and Cullion, R. N., 2004, "Fluid Flow Through Microscale Fractal-Like Branching Channel Networks," Journal of Fluids Engineering, 125(6), pp. 1051-1057.
- [2.18] Alharbi, A. Y., Pence, D. V., and Cullion, R. N., 2004, "Thermal Characteristics of Microscale Fractal-Like Branching Channels," Journal of Heat Transfer, 126(5), pp. 744-755.
- [2.19] Wang, X. Q., Mujumdar, A. S., and Yap, C., 2006, "Thermal Characteristics of Tree-Shaped Microchannel Nets for Cooling of a Rectangular Heat Sink," International Journal of Thermal Sciences, 45(11), pp. 1103-1112.
- [2.20] Wang, X. Q., Mujumdar, A. S., and Yap, C., 2006, "Numerical Analysis of Blockage and Optimization of Heat Transfer Performance of Fractal-Like Microchannel Nets," Journal of Electronic Packaging, 128(1), pp. 38-45.
- [2.21] Kobayashi, M. H., Pedro, H. T. C., Coimbra, C. F. M., and da Silva, A. K., 2009, "Formal Evolutionary Development of Low-Entropy Dendritic Thermal Systems," Journal of Thermophysics and Heat Transfer, 23(4), pp. 822-827.
- [2.22] Chen, Y., and Cheng, P., 2002, "Heat Transfer and Pressure Drop in Fractal Tree-Like Microchannel Nets," International Journal of Heat and Mass Transfer, 45(13), pp. 2643-2648.
- [2.23] Chen, Y., and Cheng, P., 2005, "An Experimental Investigation on the Thermal Efficiency of Fractal Tree-Like Microchannel Nets," International Communications in Heat and Mass Transfer, 32(7), pp. 931-938.
- [2.24] Enfield, K. E., Siekas, J. J., and Pence, D. V., 2004, "Laminar Mixing in Microscale Fractal-Like Merging Channel Networks," Journal of Microscale Thermophysical Engineering, 8(5), pp. 207-224.
- [2.25] Khan, W. A., and Yovanovich, M. M., 2008, "Analytical Modeling of Fluid Flow and heat Transfer in Microchannel/Nanochannel Heat Sinks," Journal of Thermophysics and Heat Transfer, 22(3), pp. 352-359.

- [2.26] Senn, S. M., and Poulikakos, D., 2004, "Laminar Mixing, Heat Transfer and Pressure Drop in Tree-Like Microchannel Nets and Their Application for Thermal Management in Polymer Electrolyte Fuel Cells," *Journal of Power Sources*, 130(1-2), pp. 178-191.
- [2.27] Muwanga, R., and Hassan, I., 2008, "Flow and Heat Transfer in a Cross-Linked Silicon Microchannel Heat Sink," *Journal of Thermophysics and Heat Transfer*, 22(3), pp. 333-331.
- [2.28] Wang, X. Q., Mujumdar, A. S., and Yap, C., 2007, "Effect of Bifurcation Angle in Tree-Shaped Microchannel Networks," *Journal of Applied Physics*, 102(7), 2007.
- [2.29] Wang, X. Q., Mujumdar, A. S., and Yap, C., 2010, "Flow and Thermal Characteristics of Offset Branching Network," *International Journal of Thermal Sciences*, 49(2), pp. 272-280.
- [2.30] Ghaedamini, H., Salimpour, M. R., and Mujumdar, A. S., 2011, "The Effect of Sveltteness on the Bifurcation Angles Role in Pressure Drop and Flow Uniformity of Tree-Shaped Microchannels," *Applied Thermal Engineering*, 31(5), pp. 708-716.
- [2.31] Reid, R. C., Prausnitz, J. M. and Poling, B. E., 1987, *The Properties of Gases and Liquids*, 4th ed., McGraw-Hill, New York.
- [2.32] Saad, Y., 1996, *Iterative Methods for Sparse Linear Systems*, PWS Publishing Company, Boston.
- [2.33] Hackbusch, W., 1985, *Multi-grid Methods and Applications*, Springer-Verlag, New York.
- [2.34] Roache, P. J., 1998, *Technical Reference of Computational Fluid Dynamics*, Hermosa Publishers, Albuquerque, New Mexico.
- [2.35] Hirsch, C., 1988, *Numerical Computation of Internal and External Flows*, John Wiley and Sons, Chichester.
- [2.36] Patankar, S. V., 1980, *Numerical Heat Transfer and Fluid Flow*, Hemisphere, Washington, D.C.
- [2.37] Apreotesi, M. A., 2007, "Microscale Thermal Management Utilizing Vapor Extraction from a Fractal-Like Branching Heat Sink," M. S. Thesis, Oregon State University, Corvallis, OR.
- [2.38] Bahrami, M., Yovanovich, M. M., and Culham, J. R., 2006, "Pressure Drop of Fully-Developed, Laminar Flow in Microchannels of Arbitrary Cross-Section," *Journal of Fluids Engineering*, 128(5), pp. 1036-1044.

[2.39] Kays, W. M., and London, A. L., 1984, Compact Heat Exchangers, 2nd ed., McGraw-Hill, New York.

CHAPTER 3

BEHAVIOR OF THERMALLY RADIATING TREE-LIKE FINS*

Abstract

The performance of tree-like fins with varying bifurcation angle, surface emissivity, material, width-to-thickness ratio, and base heat rate was examined. Overall system performance was examined computationally. The computational results have been validated, verified, and cast in terms of commonly defined dimensionless parameters. Tree-like fins were found to be more effective and more efficient than the rectangular fins. Fin efficiency and effectiveness were found to increase with increasing bifurcation angles while base temperatures were found to decrease with increasing bifurcation angles. As expected, base temperatures were highest for the largest width-to-thickness ratios and smallest for materials with relatively higher thermal conductivities.

Introduction

It is critically important to optimize the design of extended surfaces utilized by space heat rejection systems to maximize heat rejection while minimizing mass. Thermal radiation is the only mode of heat transfer available for removing waste thermal energy in a space environment. Heat generated by satellites, spacecraft, or other orbiting vehicles must be converted into useful energy or rejected into space. Rectangular flat plate radiators attached to spacecraft are typically utilized to reject waste heat in space. Such radiators are often used as a means of heat rejection for components that have specific temperature constraints. As thermal radiation is a function of

* This chapter is based on Calamas, D., and Baker, J., 2013, "Behavior of Thermally Radiating Tree-Like Fins," Journal of Heat Transfer, Accepted for Publication.

the available surface area it is important to maximize the surface area without increasing the mass or volume of the system.

The thermal performance and mass minimization of extended surfaces has been extensively studied in the past for rectangular and parabolic profiles radiating to free space where the temperature of the surroundings is absolute zero [3.1-3.8]. Geometric optimization of fin geometry to increase heat transfer per unit mass has also been studied. Aziz and Kraus [3.9] presented a thorough review and design reference of optimal geometries for radiating and convecting-radiating longitudinal fins of various profiles. Naumann [3.10] investigated flat and tapered rectangular fins joining circular tubes and developed an analytical expression to determine the maximum heat radiated per unit mass. Naumann concluded that tapering fins yielded an increase in heat transfer per unit mass. Schnurr et al. [3.11] investigated radiating straight and circular fins of rectangular and triangular profile with varying surface emissivities and concluded that for a given heat rate and base temperature a minimum mass fin array could be achieved through tapering. Krikkis and Razelos [3.12] developed correlations for spacecraft radiators with rectangular and triangular profiles based on the criteria of volume minimization and heat rejection maximization. Krikkis and Razelos concluded optimal minimum mass fin geometries were contingent upon the opening angle between fins, fin surface emissivity, and fin profile. Kumar et al. [3.13] developed correlations for optimizing finned radiators and found an ideal number of fins exists which maximizes fin effectiveness.

There have been numerous studies that examined the effect of radiative interaction between components in spacecraft radiators. Khor et al. [3.14] experimentally investigated the effects of thermal radiation on fin performance and concluded that including thermal radiation without the use of view factors can result in significant error. Shabany [3.15] developed simple

analytical correlations, based on the view factor between fins and their surroundings, for radiation heat transfer from diffuse and gray plate-fin heat sinks. Ellison [3.16] computed gray view factors for radiation heat transfer between fins and a nonreflecting ambient surface and concluded that some commonly employed methods for predicting gray body view factors had significant error when projected areas were utilized for fin height-to-spacing ratios greater than 3. Ellison found that fin structures with height-to-spacing ratios greater than 3 behaved as black bodies with surface areas equal to the projected areas. Ellison developed and recommended the use of an equivalent circuit for computing shape factors. Razelos and Krikkis [3.17] investigated the optimum dimensions of minimum volume and maximum heat rejection rectangular fins and concluded that the radiative interaction between the fin and tube should be incorporated into models. Chung and Zhang [3.18, 3.19] investigated the optimization of minimum mass longitudinal fins with mutual irradiation and concluded that radiative interaction at the base significantly impacted optimal fin geometry. Krishnaprakas and Narayana [3.20] investigated the optimal dimensions for rectangular fins with fin-fin radiation as well as diffuse and spectral surface reflection and concluded that an optimized geometry resulted in an array of short, thin fins.

Several studies have examined mathematical and physical explanations for complex geometries found in nature [3.21, 3.22]. The term “fractal”, as described by Mandelbrot [3.22], refers to geometric patterns that can be scaled down infinitely and fail to be described by classical geometry [3.23]. A fractal can be split into parts that are scaled copies of the whole, a property known as self-similarity. Fractal branching networks have identical bifurcations at all scales as a result of fixed length and width scale ratios between parent and daughter branches. Fractal patterns can be seen in coastlines, leaves, circulatory systems and even clouds. Tree-like

internal flow passages, inspired by the vascular systems of plants and animals have shown to be advantageous [3.24, 3.25]. Calamas and Baker [3.26] examined the performance of a biologically-inspired mesoscale tree-like flow network and found that system performance could be characterized in a manner similar to traditional compact heat exchangers. Calamas and Baker concluded that mesoscale tree-like flow networks have similar thermal performance as microscale flow networks while having the additional advantage of reduced pumping power. Similarly, fractal patterns have been utilized in heat exchangers to increase the surface area available for heat transfer. Van Der Vyver and Meyer [3.27, 3.28] developed a computational model for a tube-in-tube heat exchanger where the inner tube utilized a fractal pattern known as a quadratic Koch island.

Conjugate heat transfer has also been examined for extended surfaces with biologically inspired designs. Fins, with biologically inspired, tree-like designs provide larger surface areas for heat transfer for the same mass and base area when compared to traditional employed rectangular fins. Lee and Lin [3.29] investigated extended surfaces under forced and natural convection and concluded as the Reynolds number increased the number of branch levels required for optimum thermal performance decreased. Xu et al. [3.30] investigated the optimal branching ratio for conducting paths and found it to be different from the optimal branching ratio predicted by Murray's law [3.24] for internal flow. Bejan [3.31] initially discovered universal geometries that unite transport systems found in engineering and nature and concluded they could be applied to the design and optimization of engineered systems. Bejan [3.32] developed a solution for optimizing conducting paths for application in cooling a heat generating volume and found the paths form a tree-like network. Bejan's optimization technique, known as "Constructal Theory," states that finite-volume systems evolve to afford easier access to the imposed currents

that flow through it which explains the natural tendency of flow systems to evolve toward greater flow access [3.33, 3.34]. Bejan and Errera [3.35] expanded Bejan's [3.32] previous work on conduction to convection heat transfer and similarly found the fluid channels formed a volume filling tree-like flow network. Bejan and Dan [3.36] utilized two different methods to optimize the geometry of a conducting path between a volume and a point and found the two methods resulted in constructal tree networks. Bejan's constructal theory attempts to theoretically unify structures found in nature while also providing guidelines for the geometric optimization of internal and external flow structures [3.37, 3.38]. Bejan [3.39] utilized constructal theory in the design of a dendritic heat exchanger with the objective of minimizing pumping power and maximizing thermal performance and found the tree-like heat exchanger resulted in increased system performance when compared with traditional parallel channel heat exchangers. Similarly, da Solva et al. [3.40] and Zimparov et al. [3.41] utilized constructal theory in the design of heat exchangers. Bejan's constructal theory has also been extended to fins in convection heat transfer and resulted in increased thermal performance when compared to traditionally utilized extended surfaces [3.42-3.45]. There are also several critical reviews examining constructal theory [3.46, 3.47]. The application of Bejan's constructal law of design in nature, originally developed for convection and conduction heat transfer, in the present analysis can be seen in the tree-like design of the thermally radiating extended surfaces.

Plawsky [3.48] investigated tree-like fins and concluded that while the surface area increases with each generation, or branch level, fin efficiency and effectiveness approach asymptotic values. There has not, however, been an investigation on the use of tree-like fins for application in heat removal from a surface source solely by thermal radiation. It is hypothesized that tree-like fins offer the advantages of increased surface area for thermal radiation heat

transfer, increased effectiveness, and lower base temperatures when compared to rectangular fins of equal mass, volume and base surface area. In this paper, the effect of varying tree-like fin geometry, base heat rates, surface emissivity, material, and thickness on fin performance is investigated. The increase in surface area per unit mass that tree-like fins offer when compared with traditionally employed rectangular fins could result in the improved thermal performance of spacecraft heat rejection systems.

Tree-like Fins

The nomenclature and coordinate system used to describe the tree-like fins can be seen in Figure 3.1

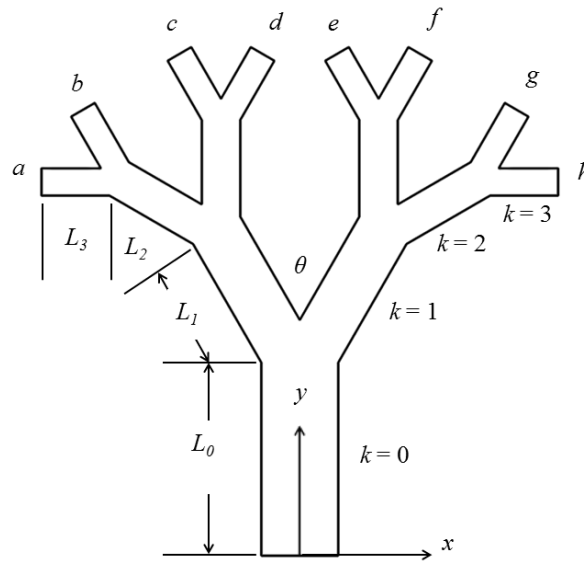


Figure 3.1. Tree-Fin Nomenclature and Coordinate system

The following branch scale ratios will be utilized to characterize the branching of the tree-like fins,

$$\beta = \frac{w_{k+1}}{w_k} = n^{-1/2} \quad (3.1)$$

$$\gamma = \frac{L_{k+1}}{L_k} = n^{-1/2} \quad (3.2)$$

Five different width-to-thickness ratios will be utilized and are defined as follows,

$$\Gamma = \frac{w}{\delta} \quad (3.3)$$

For this analysis, $n = 2$ as each parent branch splits into 2 daughter branches. The first branch, which corresponds to the base of the fin, is defined as the zeroth-order branch, $k = 0$, and the last branch, which corresponds to the tip of the fin, is defined as the third-order branch, $k = 3$. The tree-like fins feature symmetric branching. The bifurcation angle is defined as the angle between two branches at the same branch level. The dimensions for the tree-like fins can be seen in Table 3.1 and are constant regardless of bifurcation angle.

Table 3.1. Tree-Like Fin Dimensions

k	L (cm)	w (cm)
0	2.500	1.000
1	1.768	0.707
2	1.250	0.500
3	0.884	0.354

Each individual tree-like fin has a corresponding rectangular fin of equal mass, volume, and base surface area to which it was compared. The three tree-like fins can be seen in Figure 3.2. The tree-like fins will be described by their bifurcation angle between branches. For example, the tree-like fin with a bifurcation angle of 90° will be denoted as “Tree 90° ” in all figures. The rectangular fin having the same mass, volume, and base area as the 90° tree-like fin will be denoted as “Rectangle 90° ” in all figures. The geometric and mass properties for the tree-like and rectangular fins can be seen in Table 3.2.

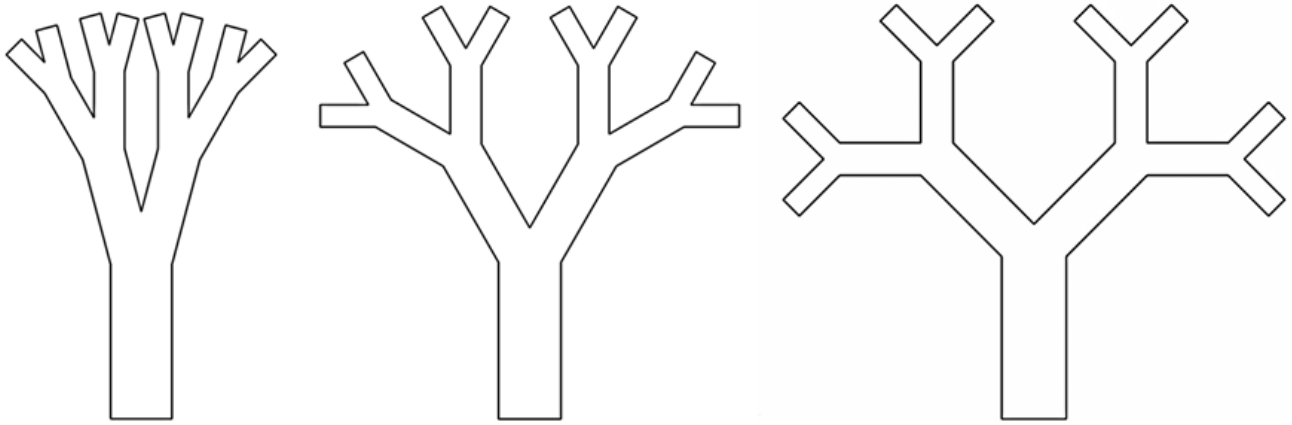


Figure 3.2. 30, 60, and 90 ° Bifurcation Angle Tree-Like Fins

Table 3.2. Tree-Like And Rectangular Fin Dimensions and Mass Properties

Fin	Angle (°)	m (g)	w (cm)	δ (cm)	H (cm)	A_s (cm ²)	A_b (cm ²)	V (cm ³)
Tree	30	21.80	1.00	0.25	-	28.05	0.25	2.45
Rectangle	-	21.80	1.00	0.25	9.80	24.99	0.25	2.45
Tree	60	23.02	1.00	0.25	-	30.21	0.25	2.59
Rectangle	-	23.02	1.00	0.25	10.35	26.37	0.25	2.59
Tree	90	23.92	1.00	0.25	-	31.51	0.25	2.69
Rectangle	-	23.92	1.00	0.25	10.75	27.38	0.25	2.69

Computational Model

The computational fluid dynamic simulations were performed using commercially available computational fluid dynamics software which utilizes the ray tracing method to calculate radiative heat transfer. Thermal radiation heat transfer from solid surfaces is assumed to be diffuse. The radiative intensity per unit area per unit solid angle is isotropic and obeys Lambert's law. The absorptivity and emissivity of radiative surfaces are assumed to obey Kirchhoff's law. Radiative surfaces which are not specified as a blackbody are assumed as ideal graybodies as they are wavelength independent. The net radiative heat flux at the surfaces, which is the difference between the irradiation and radiosity, is defined as,

$$q'' = \varepsilon\sigma T^4 + \rho_T q''_{T,i} - \alpha q''_{T,i} \quad (3.4)$$

For gray surfaces, the reflectivity is simply calculated as one minus the emissivity. Radiation heat fluxes are solved using a discrete ray Monte-Carlo method which emits equally distributed rays in the zenith and azimuthal direction forming a hemisphere over a radiative surface. Each ray is traced from a radiative surface until it intercepts the computational domain's boundary or another radiative surface. When a ray intercepts a radiative surface, the radiation heat carried by the ray is uniformly distributed over the area of intersection. The incident radiative heat flux on a surface can thus be calculated as,

$$q''_{T,i} = \sum F_{i,k} q''_{T,i,k} \quad (3.5)$$

The governing equation for the solid media can be seen in Equation 3.6.

$$\frac{\partial^2 T}{\partial x_i^2} = 0 \quad (3.6)$$

The radiative heat flux boundary condition at thermally radiating solid surfaces can be seen in Equation 3.7. The constant heat flux boundary condition at the fin base can be seen in Equation 3.8.

$$\varepsilon\sigma T^4 + \rho_T q''_{T,i} - \alpha q''_{T,i} = -k \frac{\partial T}{\partial x_n}, \quad S = S_r \quad (3.7)$$

$$q'' = -k \frac{\partial T}{\partial x_n}, \quad S = S_b \quad (3.8)$$

The governing equation is solved with the finite volume method on a spatially rectangular computational mesh with the planes orthogonal to the Cartesian coordinate system axes. The computational mesh is refined locally at the solid surface. Basic mesh cells intersecting with the solid surface are split uniformly into smaller cells until a specified cell size is obtained. The mesh is further refined at the solid surface until the maximum angle between the normal to the surface inside a cell does not exceed a specified value. The governing equation is discretized in a

conservative form. The numerical model is spatially second-order accurate. The governing equation is integrated over a control volume and approximated with cell-centered values of temperature [3.49-3.51].

Validation and Verification

The three-dimensional computational model was validated with the theoretical model for fin efficiency developed by Mackay et al. [3.4] and presented by Kern and Kraus [3.52] for longitudinal radiating fins of rectangular profiles. The nomenclature and coordinate system for the validation model can be seen in Figure 3.3.

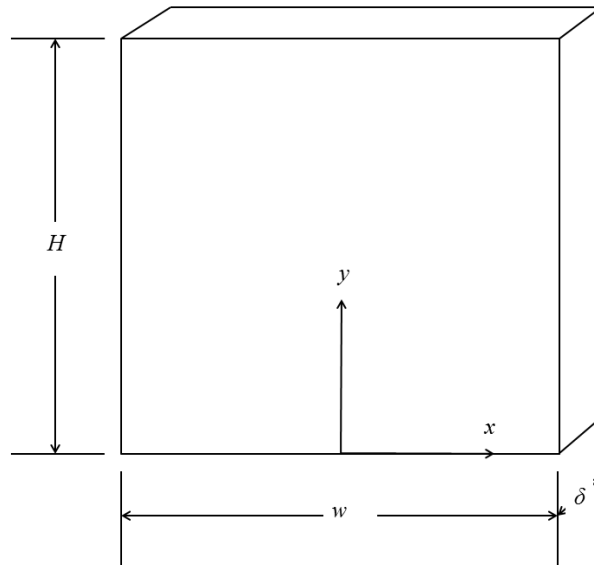


Figure 3.3. Computational Model Validation Nomenclature and Coordinate System

The dimensions for the computational model of the longitudinal radiating fin of rectangular profile can be seen in Table 3.3. The rectangular fins were assumed to radiate to free space where the environmental temperature is taken as absolute zero. Heat enters the longitudinal rectangular fins at the base and passes from the fin faces by radiation only to an environment at 0 K. Radiant interactions between the fin and a base were neglected as this would require additional information. The base temperature was assumed to be constant and the tip of the fin is

insulated. Nine different base temperatures from 200 K to 600 K in increments of 50 K were utilized in the validation case. The fin material was assumed to be copper with a temperature dependent thermal conductivity and a surface emissivity of 1.0 in the computational model. The thermal conductivity was assumed to be a constant 390 W/mK in the theoretical model.

Table 3.3. Validation Model Dimensions

H (cm)	w (cm)	δ (cm)	A_s (cm ²)	A_b (cm ²)
10	10	0.25	210	2.50

The theoretical and computational results are compared for fin efficiency. Fin efficiency is defined as the ratio of the fin heat transfer rate to the heat transfer rate if the entire fin were at the base temperature. The theoretical fin efficiency is defined as follows [3.38],

$$\eta_t = \frac{2\left(\frac{1}{Z^3} - \frac{1}{Z^8}\right)^{1/2}}{H\left(\frac{20\sigma T_b^3}{k\delta}\right)^{1/2}} \quad (3.9)$$

The calculated computational model for fin efficiency utilized for comparison is defined as follows,

$$\eta_f = \frac{Q}{\varepsilon\sigma A_s T_b^4} \quad (3.10)$$

The percent difference between the theoretical model and the computational model generally increased with increasing base temperatures. The largest percent error was found to be 1.93 % which corresponded to a base temperature of 600 K. The percent error was less than 2.0 % for all base temperatures. The graphical comparison of the computational and theoretical model fin efficiency as a function of the dimensionless temperature ratio can be seen in Figure 3.4. To verify that the results are grid independent the number of cells was successively doubled until grid independence was achieved. The grid was refined six times. The use of approximately

30,000 cells proved to be sufficient for the analysis. The largest localized numerical errors occurred at the base of the fin and for solid temperature are on the order of 0.09 K.

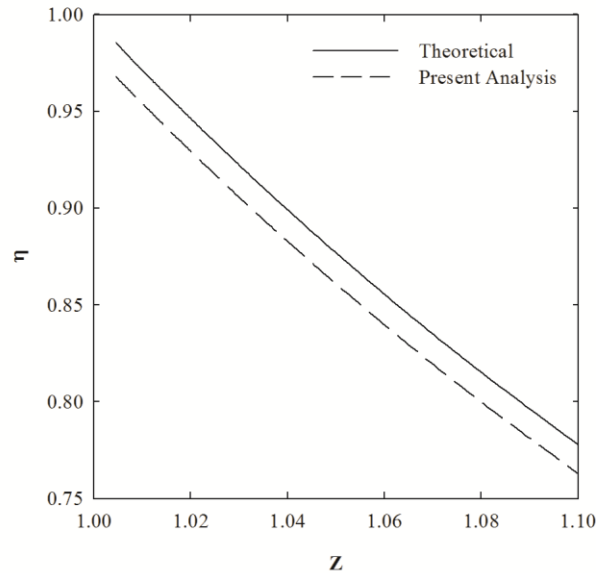


Figure 3.4. Computational Model Validation

Results and Discussions

The tree-like and rectangular fins were examined with 6 different heat rates at their base. The heat rates applied were 1, 5, 10, 15, 20, and 25 W. The fin material was assumed to be copper with three different surface emissivities of 1.0, 0.9 and 0.8. Results for fin surface emissivities of 1.0 are presented unless otherwise stated as decreasing the surface emissivity under the conditions studied did not yield qualitatively different results. Three different fin configurations, with bifurcation angles of 30, 60, and 90 ° were investigated. Four different fin materials, consisting of copper, aluminum, gold, and silver were also investigated. Results for copper as the fin material are presented unless otherwise stated. In addition, 5 different fin thicknesses were investigated corresponding to width-to-thickness ratios of 1, 2, 4, 8, and 16. Results for a fin width-to-thickness ratio of 4 are presented unless otherwise stated.

Fin effectiveness is defined as the ratio of the fin heat transfer rate to the heat transfer rate if a fin were not present. Fin effectiveness is thus defined as follows,

$$\varepsilon = \frac{Q}{\sigma \varepsilon A_b T_b^4} \quad (3.11)$$

Fin effectiveness as a function of heat rate for the 30, 60, and 90 ° tree-like and rectangular fins corresponding to the tree-like fins of equal mass, and base area can be seen in Figure 3.5. It should be noted that the tip temperature for the tree-like fins is calculated as the average temperature at the tips of the $k = 3a$ branch level.

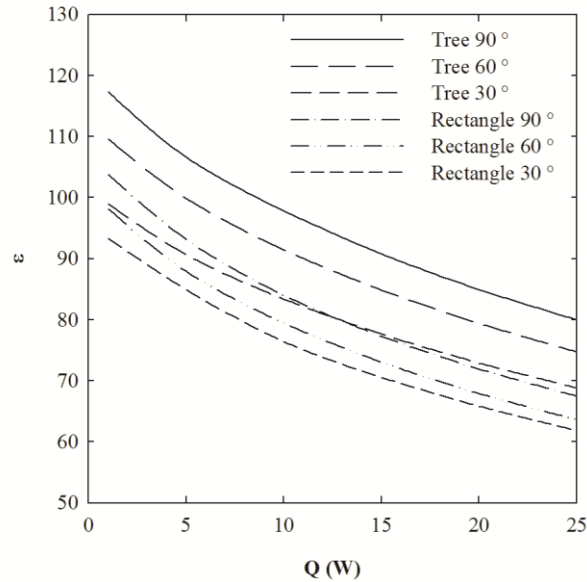


Figure 3.5. Fin Effectiveness with Varying Heat Rate

Effectiveness for the tree-like fins was found to increase with bifurcation angle. Inter-surface thermal radiation interactions decrease with increasing bifurcation angles as projected areas between branches decrease. The decrease in inter-surface thermal radiation interactions results in increased fin effectiveness as less thermal radiation is absorbed by neighboring branches. Though not graphically presented due to qualitatively similar behavior, fin

effectiveness was found to increase with decreasing surface emissivity for the tree-like and rectangular fins. As a consequence of the aforementioned assumptions regarding radiative properties, as the emissivity decreases the absorptivity also decreases which results in less absorption of inter-surface irradiation due to increased reflectivity. The tree-like fins were found to be more effective, regardless of bifurcation angle, than their rectangular counterparts. Fin effectiveness was found to decrease with increasing base heat rate as a consequence of an increasing solid temperature gradient as well as base temperature.

At all base heat rates and surface emissivities studied the 90 ° tree-like fin was more effective than the 60 ° and 30 ° tree-like fins as well as the rectangular fins. As such, fin material was varied for the 90 ° tree-like fin only. The materials considered and their corresponding density and fin mass can be seen in Table 3.4.

Table 3.4. Fin Material Mass Properties

Material	ρ (kg/m ³)	m (g)
Copper, Cu	8900	23.92
Aluminum, Al	2689	7.23
Gold, Au	19320	51.92
Silver, Ag	10500	28.22

Fin effectiveness as a function of base heat rate for the 90 ° tree-like fin of varying fin material can be seen in Figure 3.6. Silver and copper have the highest effectiveness due to their high thermal conductivities relative to the other materials. However, on a per unit mass basis the aluminum fin is the most effective (refer to Figure 3.7) due its low density relative to the other materials.

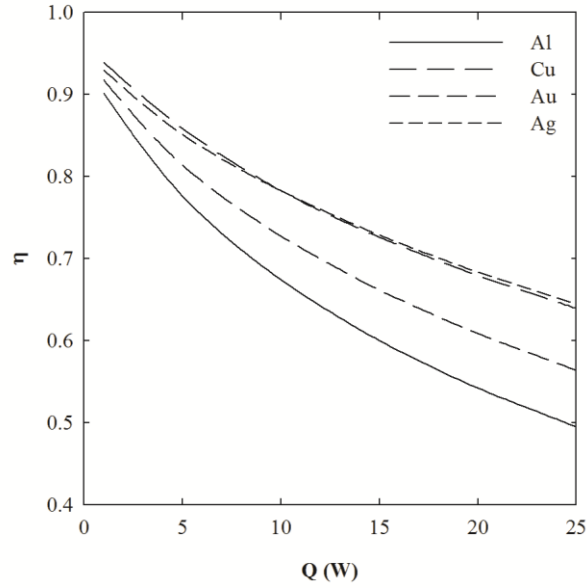


Figure 3.6. Fin Effectiveness with Varying Material for the 90 ° Tree-Like Fin

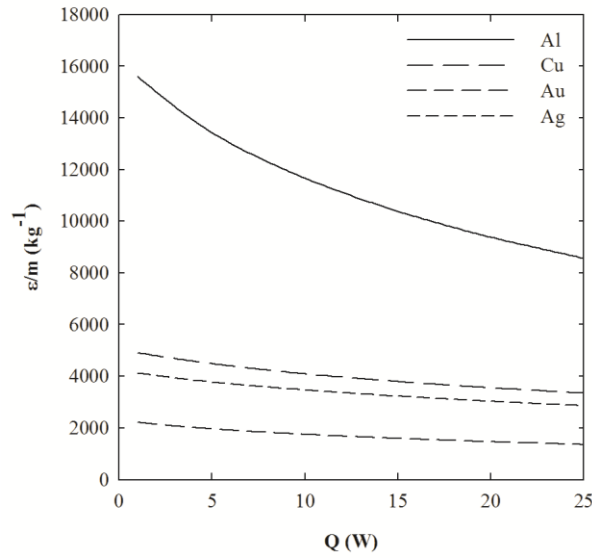


Figure 3.7. Fin Effectiveness per unit Mass With Varying Material for the 90 ° Tree-Like fin

The tree-like and rectangular fins previously utilized in the present analysis had a width-to-thickness ratio of 4. When compared to a width-to-thickness ratio of 4, width-to-thickness

ratios of 8 and 16 result in a decrease in fin base area of 75 and 50 % respectively while width-to-thickness ratios of 1 and 2 result in an increase in fin base area of 100 and 300 % respectively.

The thickness for the 90° tree-like fin was varied as can be seen in Table 3.5.

Table 3.5 Varying Fin Thickness Area and Mass Properties

δ (cm)	w (cm)	Γ	A_b (cm ²)	A_s (cm ²)	m (g)
0.0625	1.0	16	0.0625	24.00	5.98
0.1250	1.0	8	0.1250	26.51	11.96
0.2500	1.0	4	0.2500	31.51	23.92
0.5000	1.0	2	0.5000	41.52	47.84
1.0000	1.0	1	1.0000	61.54	95.67

Fin effectiveness as a function of width-to-thickness ratio for the 90 ° tree-like fin can be seen in Figure 3.8.

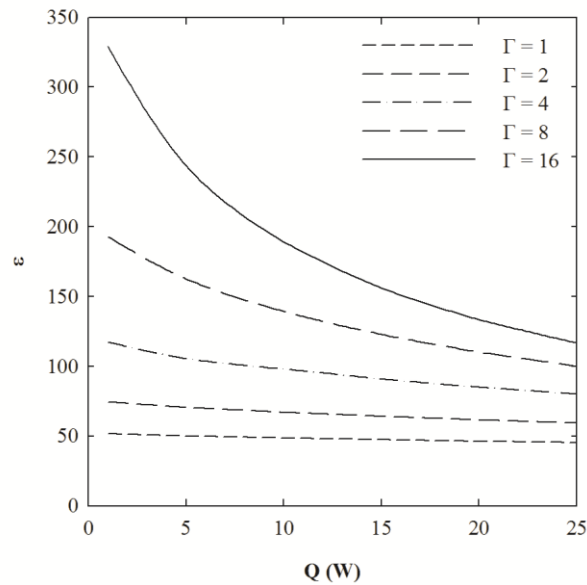


Figure 3.8. Fin Effectiveness with Varying Width-to-Thickness Ratio for the 90 ° Tree-Like Fin

The effectiveness was found to decrease with increasing base heat rate under the conditions studied. Inter-surface thermal radiation interactions decrease with increasing width-to-thickness

ratios as projected areas between branches decrease. Temperature gradients across the thickness of the fin were found to decrease with width-to-thickness ratio. Base temperatures were found to increase with width-to-thickness ratio. The thinner fins thus result in increased fin effectiveness.

As previously mentioned, fin efficiency is defined as the ratio of the fin heat transfer rate to the heat transfer rate if the entire fin were at the base temperature. The solid temperature gradient for the tree-like fins can be seen in Figure 3.9. As can be seen in Figure 3.9, temperature uniformity increases with bifurcation angle which results in increased fin efficiency. The geometry of the tree-like fins results in an increase in surface area when compared to the rectangular fins. The 30, 60 and 90 ° tree-like fins result in an increase in surface area of 12.24, 14.56, and 15.08 % respectively when compared with their rectangular fin counterparts. Fin efficiency as a function of base heat rate for the 30, 60, and 90 ° tree-like and rectangular fins can be seen in Figure 3.10. As previously mentioned, inter-surface thermal radiation interactions decrease with increasing bifurcation angles as projected areas between branches decrease which, as with fin effectiveness, results in increased fin efficiency.

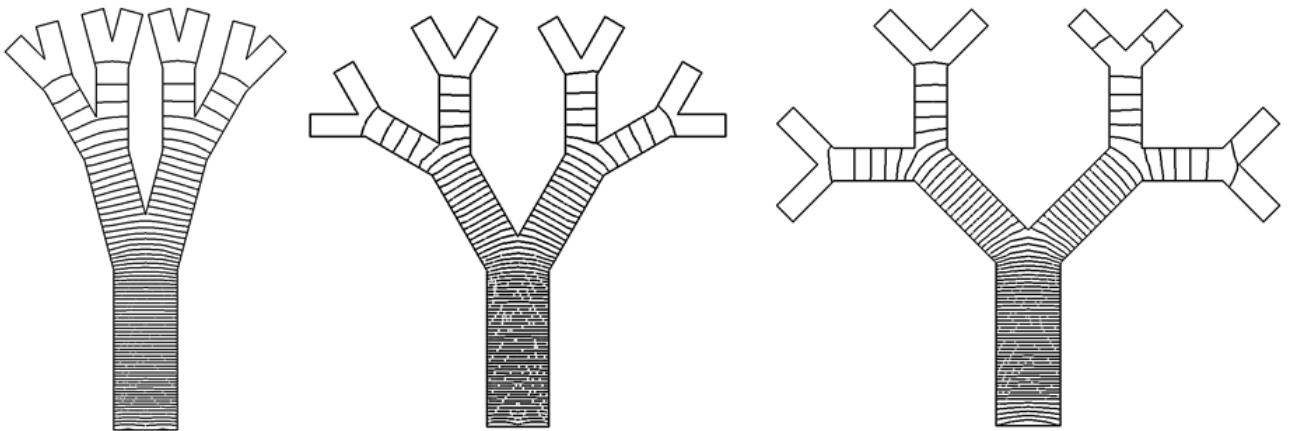


Figure 3.9. Tree-Like Fin Temperature Isolines

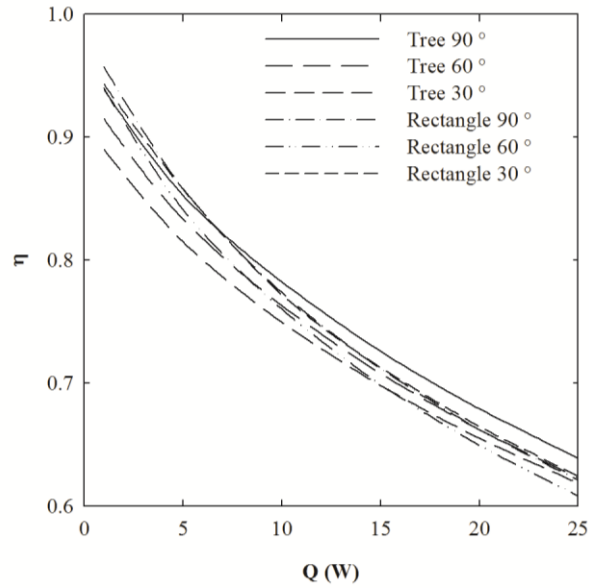


Figure 3.10. Fin Efficiency with Varying Heat Rate

The tree-like fins are more efficient than the rectangular fins, regardless of bifurcation angle and surface emissivity. At all base heat rates and surface emissivities studied the 90 ° tree-like fin was more efficient than the 60 ° and 30 ° tree-like fins. Fin efficiency as a function of base heat rate for the 90 ° tree-like fin of varying fin material can be seen in Figure 3.11.

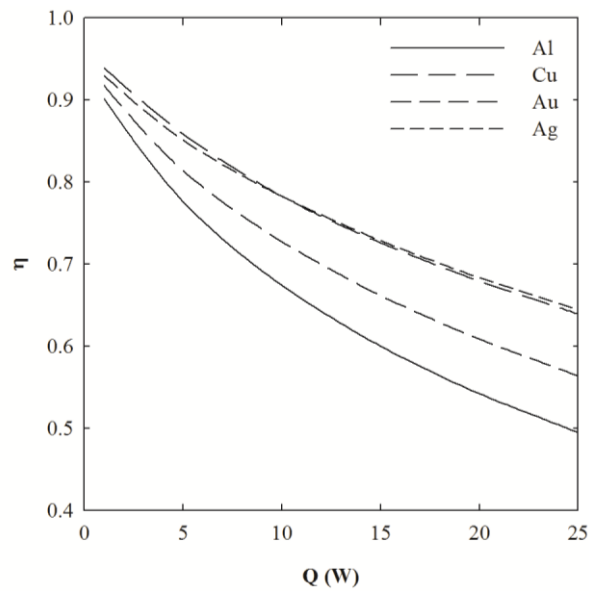


Figure 3.11. Fin Efficiency with Varying Material for the 90 ° Tree-Like Fin

As with fin effectiveness, silver and copper have the highest efficiency for the conditions studied due to their relatively high thermal conductivities. The previously studied tree-like and rectangular fins had a width-to-thickness ratio of 4. Width-to-thickness ratios of 8 and 16 result in a decrease in fin surface area of 23.83 and 15.87 % respectively. Width-to-thickness ratios of 1 and 2 result in an increase in fin surface area of 31.77 and 95.30 % respectively. As with effectiveness, the width-to-thickness ratio was varied for the 90 ° tree-like fin only as it was the most efficient fin under the conditions studied. Fin efficiency as a function of width-to-thickness ratio for the 90 ° tree-like can be seen in Figure 3.12. While increasing width-to-thickness ratios results in increased fin effectiveness, fin efficiency decreases as a result of higher base temperatures.

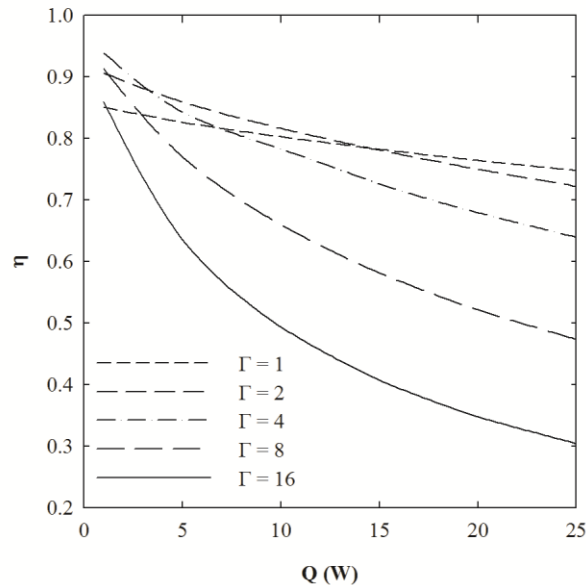


Figure 3.12. Fin Efficiency with Varying Width-to-Thickness Ratio for the 90 ° Tree-Like Fin

The tree-like and rectangular fin base temperatures as a function of heat rate can be seen in Figure 3.13.

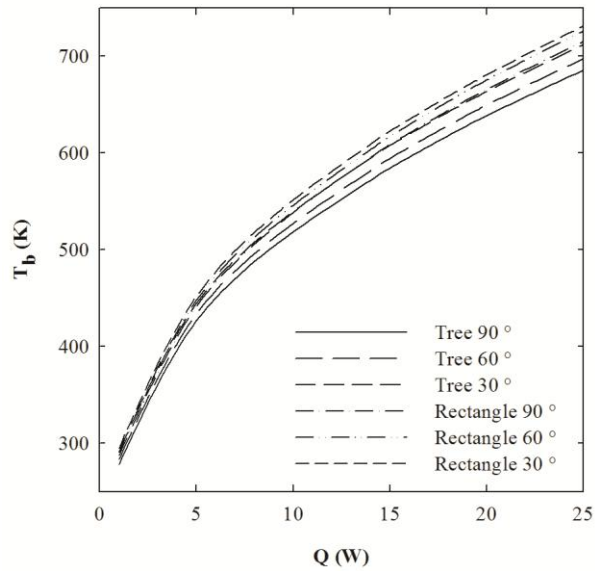


Figure 3.13. Fin Base Temperatures with Varying Heat Rate

Base temperatures, regardless of bifurcation angle and surface emissivity, are lower for the tree-like fins when compared to the rectangular fins. Base temperatures for the tree-like and rectangular fins were found to increase with decreasing surface emissivity under the conditions studied as the amount of thermal radiation leaving the surface of the fins decreases. Though the tree-like and rectangular fins have equal base areas as they have the same width and thickness, the tree-like fins have more surface area which similarly results in lower base temperatures. The 90° tree-like fin had lower base temperatures at all surface emissivities when compared with the 60° and 30° tree-like fins as well as the rectangular fins. Base temperatures as a function of heat rate and fin material for the 90° tree-like can be seen in Figure 3.14.

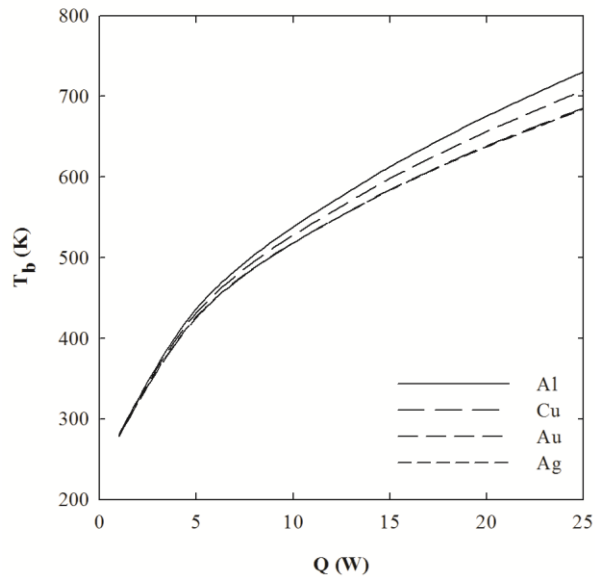


Figure 3.14. Fin Base Temperature for Varying Fin Material for the 90 ° Tree-Like Fin

Silver and copper had the lowest base temperatures attributed to their relatively high thermal conductivities when compared with the other materials studied. The fin base temperatures for the 90 ° tree-like fin with varying width-to-thickness ratio can be seen in Figure 3.15. The 90 ° tree-like fin with a width-to-thickness ratio of 16 had the highest base temperatures while the fin with a width-to-thickness ratio of 1 has the lowest base temperatures. The increase in base temperature with increasing width-to-thickness ratio is attributed to decreasing fin base surface area.

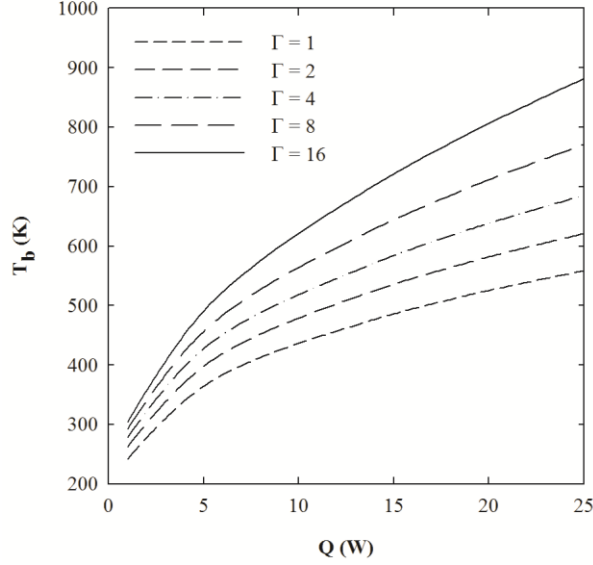


Figure 3.15. Fin Base Temperature for Varying Width-to-Thickness Ratio for the 90 ° Tree-Like

Fin

Correlation

A computational correlation was employed in order to better quantify the performance of the tree-like fins. Four dimensionless groups, obtained using the Buckingham Pi Theorem [53], were used to correlate tree-like fin effectiveness. Two of the dimensionless parameters, the temperature ratio and the width-to-thickness ratio have been previously defined. Two additional parameters, an area ratio and the Stark number, will be introduced. The ratio of the surface area for the tree-like fin in consideration divided by the surface area for the 30 ° tree-like fin is defined as,

$$A = \frac{A}{A_{30^\circ}} \quad (3.12)$$

The surface area of the 30 ° tree-like is utilized in the denominator of the area ratio term as it has the smallest surface area of the tree-like fins. This allows the increase in surface area that

corresponds to an increase in bifurcation angle to be incorporated. The Stark number is the ratio of the heat transferred by radiation to that transferred by conduction and is defined as follows,

$$Sk = \frac{\varepsilon \sigma L_c T_b^3}{k} \quad (3.13)$$

The characteristic length of a tree-like fin was defined as the root of the surface area. The various constants for the correlation were established through a minimization of the average error between the predicted fin effectiveness and the computational model fin effectiveness. The four aforementioned dimensionless parameters used to correlate the effectiveness of the tree-like fins can be seen in Equation 3.14.

$$\varepsilon = 24.533 Z^{-3.124} \Gamma^{1.072} \Lambda^{1.014} Sk^{0.002} \quad (3.14)$$

The correlation that can be seen in Figure 3.16 resulted in an average error of 1.50 % and a maximum error of 5.85 %.

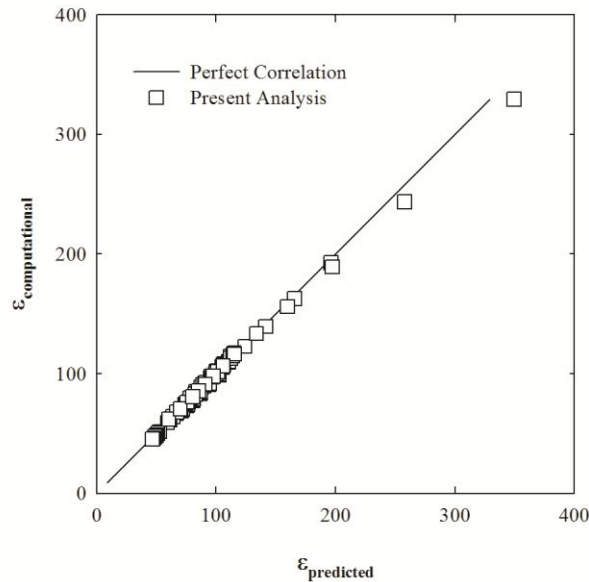


Figure 3.16. Tree-Like Fin Effectiveness Correlation

Conclusion

A validated and verified computational model has been developed to study the effects of fin geometry on fin effectiveness, efficiency and base temperature. The tree-like fins were found to be more effective than rectangular fins of equal mass, base area, and volume. Fin effectiveness was found to increase for the tree-like fins with bifurcation angle due to increased surface area and decreased projected areas between branches for thermal radiation interactions. Fin effectiveness per unit mass was found to be highly dependent on material density and less dependent on material thermal conductivity. For example, while the silver and copper fins had the highest effectiveness the aluminum fin had the greatest effectiveness on a per unit mass basis. Fin effectiveness was found to be highest for fins with the largest width-to-thickness ratios as fin effectiveness is a function of base area. The thinner fins also result in decreased projected areas between branches and consequently less thermal radiation interaction. The tree-like fins were found to be more efficient than rectangular fins of equal mass, base area, and volume for heat rates of 5, 10, 15, 20, and 25 W and less efficient for an applied heat rate of 1 W. Fin efficiency was found to increase for the tree-like fins with bifurcation angle as fin temperature uniformity increased. Fin efficiency was found to be highest for materials with relatively higher thermal conductivities. Fin efficiency was found to be highest for fins with the smallest width-to-thickness ratios as fin efficiency is a function of surface area. The tree-like fins were found to have lower base temperatures than rectangular fins of equal mass, base area, and volume. Fin base temperatures were found to decrease with increasing bifurcation angle. Materials with relatively higher thermal conductivities had lower base temperatures. Fins with larger width-to-thickness ratios were found to have high base temperatures due to decreased base surface areas. A correlation for the effectiveness of the tree-like fins was also developed which incorporated

the various parameters investigated. The correlation had an average error of 1.50 %. The thermal performance of the tree-like fins was found to be greater than that of the rectangular fins as they were found to be more effective, efficient and had lower base temperatures under the conditions studied.

Acknowledgement

Portions of this work were funded by the University of Alabama GK-12 Program. The GK-12 Program is supported by the National Science Foundation under grant 0742504.

References

- [3.1] Schmidt, E., 1926 "Die Wärmeübertragung durch Rippen, Z.," Verein. Deutsch. Ing., 70, pp. 885-889.
- [3.2] Duffin, R. J., 1959, "A Variational Problem Relating to Cooling Fins," J. Mathematics and Mechanics, 8, pp. 47-56.
- [3.3] Liu, C., 1962, "A Variational Problem with Applications to Cooling Fins," J. Society for Industrial and Appl. Mechanics, 10(1), pp. 19-29.
- [3.4] Mackay, D. B., and Leventhal, E. L., 1960, "Radiant Heat Transfer from a Flat Plate Uniformly Heated Along the Edge," AIChE 4th National Heat Transfer Conference, New York.
- [3.5] Wilkins, J. E., 1960, "Minimum-Mass Thin Fins which Transfer Heat Only by Radiation to Surroundings at Absolute Zero," J. Society for Industrial and Applied Mathematics, 8(4), pp. 630-639.
- [3.6] Bartas, J. G., and Sellers, W. H., 1960, "Radiation Fin Effectiveness," J. Heat Transfer, 82C, pp. 73-75.
- [3.7] Sparrow, E. M., and Eckert, E. R. G., 1962, "Radiant Interaction between Fin and Base Surfaces," J. Heat Transfer, 84(1), pp. 12-18.
- [3.8] Callinan, J. P., and Berggren, W. P., 1959, "Some Radiator Design Criteria for Space Vehicles," J. Heat Transfer, 81C, pp. 237-238.
- [3.9] Aziz, A., and Kraus, A. D., 1996, "Optimum Design of Radiating and Convecting-Radiating Fins," Heat Transfer Engineering, 17(3), pp. 44-78.
- [3.10] Naumann, R. J., 2004, "Optimizing the Design of Space Radiators," Intl. J. Thermophysics, 25(6), pp. 1929-1941.
- [3.11] Schnurr, N. M., Shapiro, A. B., and Townsend, M. A., 1976 "Optimization of Radiating Fin Arrays With Respect to Weight," J. Heat Transfer, 98(4), pp. 643-648.
- [3.12] Krikkis, R. N., and Razelos, P., 2002, "Optimum Design of Spacecraft Radiators with Longitudinal Rectangular and Triangular Fins," J. Heat Transfer, 124(5), pp. 805-812.
- [3.13] Kumar, S. S., Nayak, N., and Venkateshan, S. P., 1993, "Optimum Finned Space Radiators," Intl. J. Heat and Fluid Flow, 14(2), pp. 191-200.

- [3.14] Khor, Y. K., Hung, Y. M., and Lim, B. K., 2010, "On the Role of Radiation View Factor in Thermal Performance of Straight-Fin Heat Sinks," *International Communications in Heat and Mass Transfer*, 37(8), pp.1087-1095
- [3.15] Shabany, Y., 2008, "Radiation Heat Transfer from Plate-Fin Heat Sinks," *Semiconductor Thermal Measurement and Management Symposium*, pp. 132-136.
- [3.16] Ellison, G. N., 1979, "Generalized Computations of the Gray Body Shape Factor for Thermal Radiation from a Rectangular U-Channel," *IEEE Transactions on Components, Hybrids and Manufacturing Technology*, 2(4), pp. 517-522.
- [3.17] Razelos, P., and Krikkis, R. N., 2001, "Optimum Design of Longitudinal Rectangular Fins with Base-to-Fin Radiant Interaction," *Heat Transfer Engineering*, 22(4), pp. 3-17.
- [3.18] Chung, B. T. F., and Zhang, B. X., 1991, "Minimum Mass Longitudinal Fins with Radiation Interaction at the Base," *J. Franklin Institute*, 328(1), pp. 143-161.
- [3.19] Chung, B. T. F., and Zhang, B. X., 1991, "Optimization of Radiating Fin Array Including Mutual Irradiation Between Radiator Elements," *J. Heat Transfer*, 113(4), pp. 814-822.
- [3.20] Krishnaprakas, C. K., and Narayana, K. B., 2003, "Heat Transfer Analysis of Mutually Irradiating Fins," *Intl. J. Heat and Mass Transfer*, 46(5), pp. 761-769.
- [3.21] Thompson, D'A. W., 1942, *On Growth and Form*, Cambridge University Press, Cambridge.
- [3.22] Mandelbrot, B. B., 1982, *The Fractal Geometry of Nature*, Freeman, New York.
- [3.23] Barnsley, M., 1988, *Fractals Everywhere*, Academic Press, San Diego.
- [3.24] Murray, C. D., 1926, "The Physiological Principle of Minimum Work. I. The Vascular System and the Cost of Blood Volume," *J. Physiology*, 12(3), pp. 207-214.
- [3.25] Cohn, D. L., 1954, "Optimal Systems: The Vascular System," *Bulletin of Mathematical Biophysics*, 16, pp. 59-74.
- [3.26] Calamas, D., and Baker, J., 2012, "Performance of a Biologically-Inspired Heat Exchanger with Hierarchical Bifurcating Flow Passages," *J. Thermophysics and Heat Transfer*, Accepted for Publication.
- [3.27] Van Der Vyver, H., 2003, "Validation of a CFD Model of a Three-Dimensional Tube-In-Tube Heat Exchanger," *Proc. of Third International Conference on CFD in the Minerals and Process Industries*, CSIRO, Melbourne, Australia, pp. 235-240.

- [3.28] Meyer, J., and Van Der Vyver, H., 2005, "Heat Transfer Characteristics of a Quadratic Koch Island Fractal Heat Exchanger," *Heat Transfer Engineering*, 26(9), pp. 22-29.
- [3.29] Lee, D. J., and Lin, W.W., 1995, "Second Law Analysis on Fractal-Like Fin under Cross Flow," *AIChE Journal*, 41(10), pp. 2314-2317.
- [3.30] Xu, P., Yu, B., Yun, M., and Zou, M., 2006, "Heat Conduction in Fractal Tree-like Branched Networks," *Intl. J. of Heat and Mass Transfer*, 49, pp. 3746-3751.
- [3.31] Bejan, A., *Shape and Structure, From Engineering to Nature*, Cambridge, Cambridge University Press, 2000.
- [3.32] Bejan, A., 1997, "Constructal-Theory Network of Conducting Paths for Cooling a Heat Generating Volume," *Intl. J. Heat and Mass Transfer*, 40(4), pp. 799-816.
- [3.33] Bejan, A., and Lorente, S., 2010, "The Constructal Law of Design and Evolution in Nature," *Phil. Trans. R. Soc. B*, 365(1545), pp. 1335-1347.
- [3.34] Bejan, A., and Lorente, S., 2006, "Constructal Theory of Generation of Configuration in Nature and Engineering," *J. Applied Physics*, 100(4).
- [3.35] Bejan, A., and Errera, M. R., 2000, "Convective Trees of Fluid Channels for Volumetric Cooling," *International Journal of Heat and Mass Transfer*, 43, pp. 3105-3118.
- [3.36] Bejan, A., and Dan, N., 1999, "Two Constructal Routes to Minimal Heat Flow Resistance via Greater Internal Complexity," *Journal of Heat Transfer*, 121(1).
- [3.37] Bejan, A., Lorente, S., and Lee, J., 2008, "Unifying Constructal Theory of Tree Roots, Canopies and Forests," *Journal of Theoretical Biology*, 254(3), pp. 529-540.
- [3.38] Rocha, L. A. O., Lorenzini, E., and Biserni, C., 2005, "Geometric Optimization of Shapes on the Basis of Bejan's Constructal Theory," *International Communications in Heat and Mass Transfer*, 32(10), pp. 1281-1288.
- [3.39] Bejan, A., 2002, "Dendritic Constructal Heat Exchanger with Small-Scale Crossflows and Larger-Scales Counterflows", *International Journal of Heat and Mass Transfer*, 45(23), pp. 4607-4620.
- [3.40] da Silva, A. K., Lorente, S., and Bejan, A., 2004, "Constructal Multi-Scale Tree-Shaped Heat Exchangers", *Journal of Applied Physics*, 96(3), pp. 1709-1718.
- [3.41] Zimparov, V. D., da Silva, A. K., and Bejan, A., 2006, "Constructal Tree-Shaped Parallel Flow Heat Exchangers, *International Journal of Heat and Mass Transfer*, 49, pp. 4558-4566.

- [3.42] Alebrahim, A., and Bejan, A., 1999, "Constructal Trees of Circular Fins for Conductive and Convective Heat Transfer," *International Journal of Heat and Mass Transfer*, 42, pp. 3585-3597.
- [3.43] Bejan, A., Almogbel, M., 2000, "Constructal T-Shaped Fins," *International Journal of Heat and Mass Transfer*, 43, pp. 2101-2115.
- [3.44] Almogbel, M., and Bejan, A., 2000, "Cylindrical Trees of Pin Fins," *International Journal of Heat and Mass Transfer*, 43, pp. 4285-4297.
- [3.45] Almogbel, A. Bejan, A., 2001, "Constructal Optimization of Nonuniformly Distributed Tree-Shaped Flow Structures for Conduction," *International Journal of Heat and Mass Transfer*, 44, pp. 4185-4195.
- [3.46] Kuddusi, L., and Egrican, N., 2008, "A Critical Review of Constructal Theory," *Energy Conversion and Management*, 49(5), pp. 1283-1294.
- [3.47] Ghodoossi, L., 2004, "Conceptual Study on Constructal Theory," *Energy Conversion and Management*, 45(9-10), pp. 1379-1395.
- [3.48] Plawky, J. L., 1993, "Transport in Branched Systems I: Steady-State Response," *Chemical Engineering Communications*, 123, pp. 71-86.
- [3.49] Glowinski, R. and Le Tallec, P., 1989, *Augmented Lagrangian Methods and Operator-Splitting Methods in Nonlinear Mechanics*. SIAM, Philadelphia.
- [3.50] Marchuk, G.I., 1982, *Methods of Numerical Mathematics*, Springer-Verlag, Berlin.
- [3.51] Samarskii, A.A., 1989, *Theory of Difference Schemes*, Nauka, Moscow.
- [3.52] Kern, D. Q., and Kraus, A. D., 1972, *Extended Surface Heat Transfer*, McGraw-Hill, New York, pp. 203-211.
- [3.53] Fox, R. W., and McDonald, A. T., *Introduction to Fluid Mechanics*, 4th ed., New York, John Wiley & Sons, 1992.

CHAPTER 4

TREE-LIKE BRANCHING FINS: PERFORMANCE AND NATURAL CONVECTIVE HEAT TRANSFER BEHAVIOR*

Abstract

The performance of tree-like fins with varying bifurcation angle, scale, material, width-to-thickness ratio, and heat flux was examined. Overall system performance was examined computationally. The computational results have been validated, verified, and cast in terms of commonly defined dimensionless parameters. Tree-like fins were found to be more effective and had lower base temperatures than the rectangular fins. Fin effectiveness was found to increase with increasing bifurcation angle while fin efficiency and base temperatures were found to decrease with increasing bifurcation angle. Base temperatures were highest for the largest width-to-thickness ratios and smallest for materials with relatively higher thermal conductivities. The microscale tree-like fin studied had the highest effectiveness and efficiency as well as the lowest base temperatures when compared to the mesoscale and macroscale fins of the same geometry.

Introduction

The rejection of waste heat is critically important in the design optimization of extended surfaces utilized by electronics, industrial equipment and other mechanical devices. It is often desirable to maximize heat rejection while minimizing the mass and volume of extended surfaces. As convective heat transfer is directly proportional to the available surface area it is important maximize surface area while minimizing system mass. The use of tree-like fins,

* Note. This chapter is based on Calamas, D., and Baker, J., 2012, "Tree-Like Branching Fins: Performance and Natural Convective Heat Transfer Behaviour," International Journal of Heat and Mass Transfer (Accepted for Publication).

inspired by biology, offer an increase in surface area per unit mass when compared with traditionally employed rectangular fins.

The thermal performance and geometric optimization of extended surfaces in natural convection has been extensively studied in the past [4.1-4.2]. Mikk [4.3] developed an optimization method for minimizing the mass of convecting fins and concluded that the mass of an ideal fin only slightly differs from that of a fin with a triangular profile. Mao and Rooke [4.4] developed an analytical solution for straight fins with a convective boundary condition at the fin tip and compared the results to previously developed solutions for straight fins with an adiabatic boundary condition at the fin tip. Mao et al. concluded neglecting tip convection led to significant errors for combinations of small length to width ratios as well as small Biot numbers. Leong and Kooi [4.5] experimentally investigated rectangular fins with varying material and base temperature and concluded that maximum heat transfer coefficients were located at positions between 22 and 45 % of the fin height measured from the base. Temperature measurements along the fin were found to be in good agreement with one-dimensional solutions for convective fin tips. Razelos and Georgiou [4.6] presented new design criteria for extended surfaces and recommended the use of the fin removal number instead of fin effectiveness. The design criteria presented require a heat transfer increase by an order magnitude of at least 10. A Biot number on the order of 0.01 and an aspect number on the order of 1 were recommended as design guidelines.

There have been numerous studies that have examined physical and mathematical explanations for complex geometries found in nature [4.7, 4.8]. Mandelbrot [4.8] describes fractals as geometric patterns that can be scaled down infinitely and fail to be described by classical geometry [4.9]. Fractal geometries are self-similar as they can be divided into parts that

are scaled copies of the whole. Fractal-like branching networks have identical bifurcations at all scales which results from fixed bifurcation angles as well as fixed length and width scale ratios between parent and daughter branches. Fractal patterns can be found in nature and can be seen in coastlines, leaves and clouds. Tree-like internal flow passages, inspired by the vascular systems of plants and animals have shown to be advantageous as they minimize flow resistance [4.10, 4.11]. Calamas and Baker [4.12] examined the performance of a biologically-inspired mesoscale tree-like flow network and found that system performance could be characterized in a manner similar to traditional compact heat exchangers. Calamas and Baker concluded that mesoscale tree-like flow networks have similar thermal performance as microscale flow networks while having the additional advantage of reduced pumping power. Fractal patterns have been employed in heat exchangers to increase the surface area available for heat transfer. Van Der Vyver and Meyer [4.13, 4.14] developed a computational model for a tube-in-tube heat exchanger where the inner tube utilized a fractal pattern known as a quadratic Koch island. Bonjour et al. [4.15] optimized the use of branched fins for a coaxial two-stream heat exchanger in order to minimize the global thermal resistance. Bonjour et al. concluded the optimal configuration is dependent on the cross section of the heat exchanger as well as the smallest fin structure that can be manufactured.

Conjugate heat transfer has also been examined for extended surfaces with biologically inspired designs. Fins, with biologically inspired, tree-like designs provide larger surface areas for heat transfer for the same mass and base area when compared to traditional employed rectangular fins. Lee and Lin [4.16] performed a second law analysis on fractal-like fins under cross flow and concluded that as the Reynolds number increases the number of optimal branch levels decreases. Lin and Lee [4.17] analytically investigated the thermal performance of

branching fins with a power-law heat transfer coefficient. Xu et al. [4.18] investigated the optimal branching ratio for conducting paths and found it to be different from the optimal branching ratio predicted by Murray's law [4.10] for internal flow. Plawsky [4.19, 4.20] investigated the thermal performance of branched extended surfaces and concluded that while the surface area of branching structures increase with branch level, there is a finite number of branch levels after which fin efficiency and effectiveness fail to increase. Plawsky found that the thermal performance of contracting branching structures was higher than that of expanding structures.

Bejan [4.21] developed a solution for optimizing conducting paths for application in cooling a heat generating volume and found the paths form a tree-like network. Bejan's optimization technique, known as "Constructal Theory," states that finite-volume systems evolve to afford easier access to the imposed currents that flow through it which explains the natural tendency of flow systems to evolve toward greater flow access [4.22, 4.23]. Almgel [4.24] presented a geometric optimization technique for tree-like fins based on fin volume and material and found that the global thermal conductance can be maximized. Almgel concluded that optimized tree-like fins offer greater thermal performance when compared with longitudinal and optimized T-shaped fins. Lorenzini and Rocha [4.25] presented a numerical optimization of Y-shaped fins based on fin volume and material and through a triple optimization found an optimal structure that minimized the global thermal resistance. Y-shaped fin structures were found to offer increased thermal performance when compared to T-shaped structures. Bejan and Dan [4.26] utilized two different methods to optimize the geometry of a conducting path between a volume and a point and found the two methods resulted in constructal tree networks. Calamas and Baker [4.27] investigated the thermal performance of tree-like fins thermally radiating to

free space and found the tree-like fins were more effective than rectangular fins of equal mass, volume, and base area.

It is hypothesized that tree-like fins offer the advantages of increased surface area for natural convection heat transfer, increased effectiveness, and lower base temperatures when compared to rectangular fins of equal mass, volume and base surface area. In this paper, the effect of varying tree-like fin geometry, base heat fluxes, material, thickness, and scale on thermal performance is investigated. The increase in surface area per unit mass that tree-like fins offer when compared with traditionally employed rectangular fins could result in improved thermal performance of electronics and other industrial equipment.

Tree-Like Fins

The nomenclature and coordinate system used to describe the tree-like fins can be seen in Figure 4.1. The following branch scale ratios are employed in the design and characterization of the branching of the tree-like fins,

$$\beta = \frac{w_{k+1}}{w_k} = n^{-1/2} \quad (4.1)$$

$$\gamma = \frac{L_{k+1}}{L_k} = n^{-1/2} \quad (4.2)$$

Five different width-to-thickness ratios for the tree-like fins will be utilized in the present analysis and are defined as follows,

$$\Gamma = \frac{w}{\delta} \quad (4.3)$$

When employing the branch scale ratios $n = 2$ as each parent branch splits into 2 daughter branches. The first branch, which is associated to the base of the fin, is denoted as the zeroth-order branch, $k = 0$, and the final branch, which is associated to the tip of the fin, is denoted as the third-order branch, $k = 3$. The tree-like fins have symmetric branching at all branch levels.

The bifurcation angle is defined as the angle between two branches located at the same branch level. The dimensions for the tree-like fins can be seen in Table 4.1 and regardless of bifurcation angle are constant.

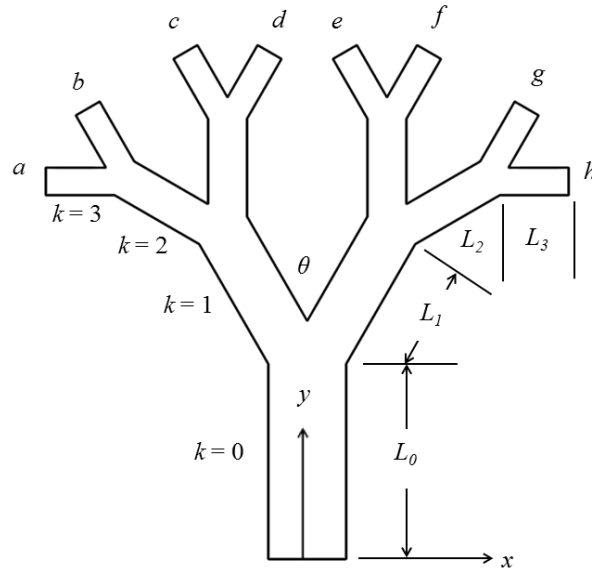


Figure 4.1. Tree-Fin Nomenclature and Coordinate System

Table 4.1. Tree-Like Fin Dimensions

k	Microscale		Mesoscale		Macroscale	
	L (mm)	w (mm)	L (cm)	w (cm)	L (cm)	w (cm)
0	2.500	1.000	2.500	1.000	25.00	10.00
1	1.768	0.707	1.768	0.707	17.68	7.07
2	1.250	0.500	1.250	0.500	12.50	5.00
3	0.884	0.354	0.884	0.354	8.84	3.54

Each individual tree-like fin has a corresponding rectangular fin of equal mass, volume, and base surface area to which it was compared. The tree-like fins are denoted by their bifurcation angle between branches. The 90, 60, and 30 ° tree-like fins can be seen in Figure 4.2. For example, the tree-like fin with a bifurcation angle of 90 ° will be defined as “Tree 90 °” in all figures. The rectangular fin of equal mass, volume, and base area as the 90 ° tree-like fin will similarly be

defined as “Rectangle 90 °” in all figures. The dimensions and mass properties for the tree-like and rectangular fins can be seen in Table 4.2.

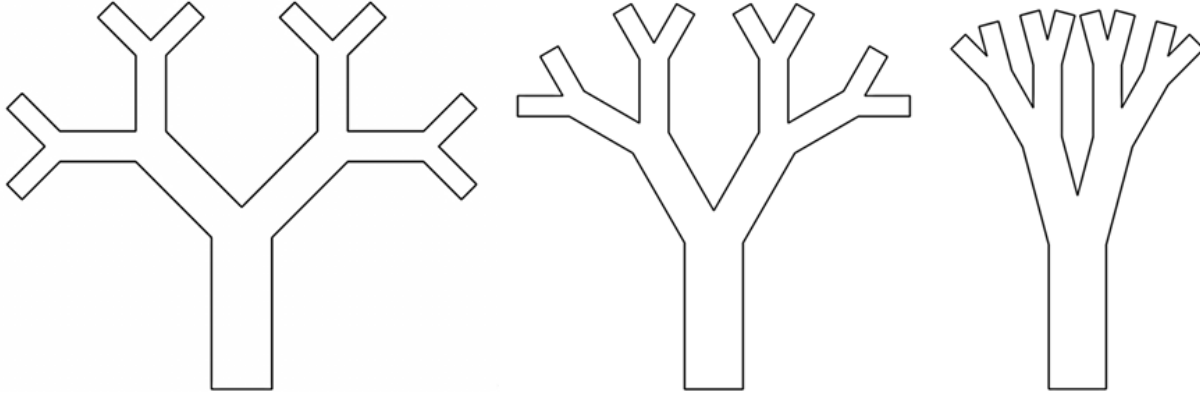


Figure 4.2. 90, 60, and 30 ° Bifurcation Angle Tree-Like Fins

Table 4.2. Tree-Like and Rectangular Fin Dimensions and Mass Properties

Fin	Angle (°)	m (g)	w (cm)	δ (cm)	H (cm)	A_s (cm ²)	A_b (cm ²)	V (cm ³)
Tree	30	21.80	1.00	0.25	-	28.05	0.25	2.45
Rectangle	-	21.80	1.00	0.25	9.80	24.99	0.25	2.45
Tree	60	23.02	1.00	0.25	-	30.21	0.25	2.59
Rectangle	-	23.02	1.00	0.25	10.35	26.37	0.25	2.59
Tree	90	23.92	1.00	0.25	-	31.51	0.25	2.69
Rectangle	-	23.92	1.00	0.25	10.75	27.38	0.25	2.69

Computational Model

The computational fluid dynamic simulations were performed using commercially available computational fluid dynamics software, employing the finite volume method. The steady form of the three-dimensional continuity, momentum, and energy equations can be seen below.

$$\frac{\partial(\rho u_i)}{\partial x_i} = 0 \quad (4.4)$$

$$\frac{\partial(\rho u_i u_j)}{\partial x_i} = -\frac{\partial p}{\partial x_i} + \frac{\partial}{\partial x_i} \left(\mu \frac{\partial u_j}{\partial x_i} \right) - \rho g_i \quad (4.5)$$

$$\frac{\partial(\rho u_i c_p T)}{\partial x_i} = \frac{\partial}{\partial x_i} \left(k \frac{\partial T}{\partial x_i} \right) \quad (4.6)$$

The governing equation for the solid media and the constant heat flux boundary condition applied at the base of the fin are as follows,

$$\nabla^2 T = 0 \quad (4.7)$$

$$q'' = -k \frac{\partial T}{\partial x_n} \quad (4.8)$$

The Navier-Stokes equations are accompanied by fluid state equations which define the nature of the fluid as well as by empirical temperature dependencies of fluid properties incorporated in the model [4.28]. The governing equations are solved with the finite volume method on a spatially rectangular computational mesh with the planes orthogonal to the Cartesian coordinate system axes and refined locally at the solid/fluid interface and in the fluid region. At the solid/fluid interface additional boundary faces and corresponding mass and heat fluxes that take into account boundary conditions and model geometry are introduced. The governing equations are discretized in a conservative form. The numerical model is spatially second-order accurate. The governing equations are integrated over a control volume and then approximated with cell-centered values of the basic variables [4.29-4.31]. Second-order upwind approximations of fluxes are based on the implicitly treated modified Leonard's QUICK [4.32] approximations and the Total Variation Diminishing [4.33] method. An elliptic type discrete pressure equation is derived by algebraic transformations of the derived discrete governing equations and incorporates velocity boundary conditions using the SIMPLE-like [4.34] method.

Validation and Verification

The three-dimensional computational model was validated with the theoretical model for fin efficiency as presented by Kern and Kraus [4.35] for longitudinal convecting fins of rectangular profiles and adiabatic tips. The nomenclature and coordinate system for the validation model can be seen in Figure 4.3. The dimensions for the computational model of the longitudinal convecting fin of rectangular profile can be seen in Table 4.3.

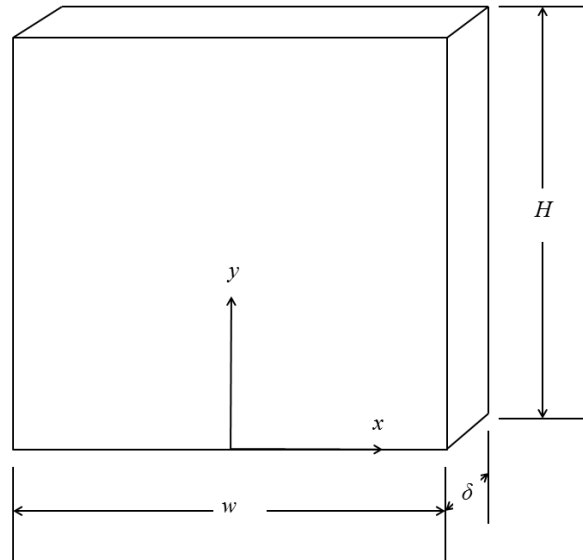


Figure 4.3. Computational Model Validation Nomenclature and Coordinate System

Table 4.3. Validation Model Dimensions

H (cm)	w (cm)	δ (cm)	A_s (cm ²)	A_b (cm ²)
10	10	0.25	210	2.50

Environmental temperature was assumed to be 293 K. The base temperature was assumed to be constant and the tip of the fin is insulated in the validation model. Six different base temperatures from 350 K to 600 K in increments of 50 K were employed in the validation case. The fin material was assumed to be copper with a temperature dependent thermal conductivity in the

computational model. The thermal conductivity was assumed to be a constant 390 W/mK in the theoretical model.

The theoretical and computational results were compared on the basis of fin efficiency. Fin efficiency is defined as the ratio of the fin heat transfer rate to the heat transfer rate if the entire fin were at the base temperature. The theoretical fin efficiency as defined by Kern and Kraus [4.34] can be seen below.

$$\eta_t = \frac{\tanh\left(\left(\frac{2h}{k\delta}\right)^{1/2} H\right)}{\left(\frac{2h}{k\delta}\right)^{1/2} H} \quad (4.9)$$

The calculated computational model for fin efficiency utilized for comparison is defined as follows,

$$\eta_f = \frac{Q}{hA_s(T_b - T_\infty)} \quad (4.10)$$

The largest percent error was found to be 1.86 % which corresponded to a base temperature of 600 K. The average percent error between the computational and theoretical fin efficiency was 1.64 %. A graphical comparison of the computational and theoretical model fin efficiency as a function of the dimensionless temperature ratio can be seen in Figure 4.4. The number of cells was successively doubled until grid independence was achieved. The grid was refined six times. The use of approximately 60,000 cells proved to be sufficient for the analysis. The largest localized numerical errors occurred at the base of the fin and for solid temperature and heat rate are on the order of 0.4 K and 0.01 W respectively.

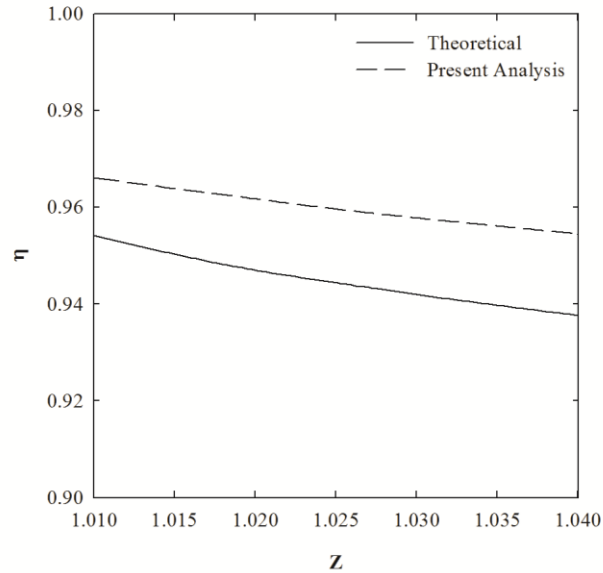


Figure 4.4. Computational Model Validation

Results and Discussions

The tree-like and rectangular fins were supplied with 5 different heat fluxes at their base. The heat fluxes applied were 1000, 5000, 10000, 15000, and 20000 W/m². The tree-like and rectangular fins had convective tips. The environment was assumed to be air at a temperature of 293 K. The fin material was assumed to be aluminum unless otherwise stated. Three different fin configurations, with bifurcation angles of 30, 60, and 90 ° were investigated. Four different fin materials, consisting of copper, aluminum, gold, and silver were also investigated. Five different fin width-to-thickness ratios of 1, 2, 4, 8, and 16 were utilized. Results are presented for a fin width-to-thickness ratio of 4 unless otherwise stated. Three different scales, microscale, mesoscale, and macroscale, were also utilized. Results are presented for mesoscale fins, whose properties can be seen in Table 4.2, unless otherwise stated.

Fin effectiveness is the ratio of the fin heat transfer rate to the heat transfer rate if a fin was not present and is defined as follows,

$$\varepsilon = \frac{Q}{hA_b(T_b - T_\infty)} \quad (4.11)$$

Fin effectiveness as a function of heat flux for the 30, 60, and 90 ° tree-like and rectangular fins corresponding to the tree-like fins of equal mass and base area can be seen in Figure 4.5. It should be noted that the tip temperature for the tree-like fins is calculated as the average temperature at the tips of the $k = 3a$ branch level. Effectiveness for the tree-like fins was found to increase with bifurcation angle. The tree-like fins were found to be more effective, regardless of bifurcation angle, than their rectangular counterparts. Fin effectiveness was found to decrease with increasing heat flux as a consequence of an increasing solid temperature gradient as well as base temperature. The 30, 60, and 90 ° tree-like fins had an average heat transfer coefficient of 7.42, 8.17, and 8.58 W/m²K respectively. The rectangular fins of equal mass and base area as the 30, 60, and 90 ° tree-like fins had average heat transfer coefficients of 7.14, 7.00, and 6.87 W/m²K respectively. Heat transfer coefficients presented are an average over all heat fluxes.

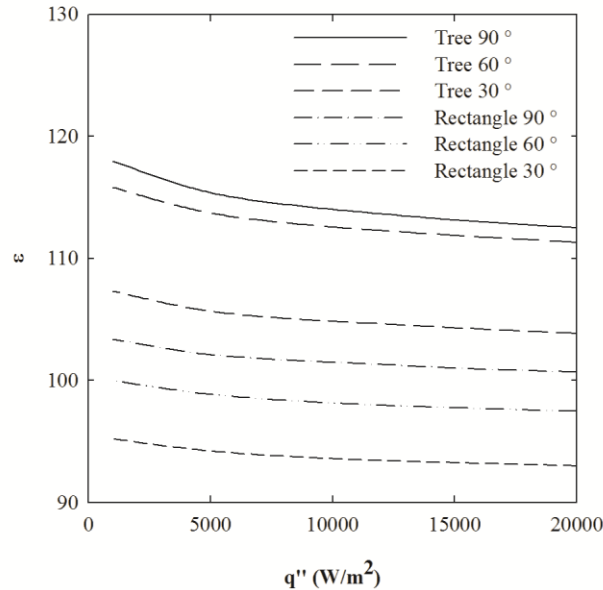


Figure 4.5. Fin Effectiveness with Varying Heat Flux

At all base heat fluxes the 90 ° tree-like fin was more effective than the 60 °, and 30 °, tree-like fins as well as the rectangular fins. As such, the fin material was varied for the 90 ° tree-like fin only. The materials considered and their corresponding density and fin mass can be seen in Table 4.4.

Table 4.4. Fin Material Mass Properties

Material	ρ (kg/m ³)	m (g)
Copper	8900	23.92
Aluminum	2689	7.23
Gold	19320	51.92
Silver	10500	28.22

Fin effectiveness as a function of heat flux for the 90 ° tree-like fin of varying fin material can be seen in Figure 4.6.

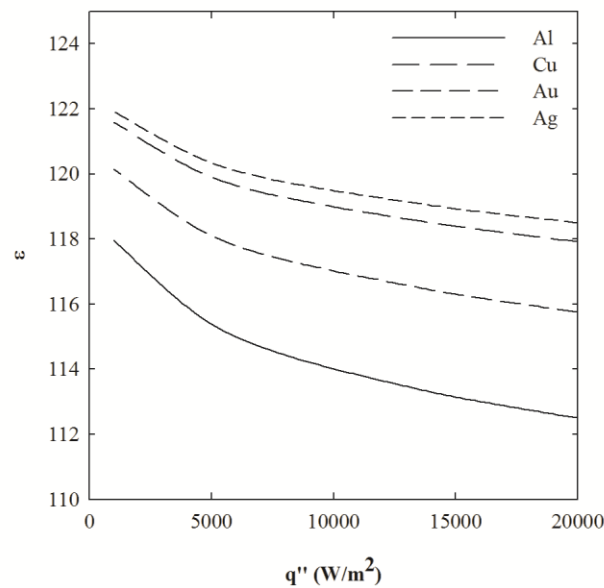


Figure 4.6. Fin Effectiveness with Varying Material for the 90 ° Tree-Like Fin

Silver and copper have the highest effectiveness due to their high thermal conductivities relative to the other materials. However, on a per unit mass basis the aluminum fin is the most effective (refer to Figure 4.7) due its low density relative to the other materials. The silver, copper, gold, and aluminum 90 ° tree-like fins had average heat transfer coefficients of 8.62, 8.62, 8.60, and 8.58 W/m²K respectively.

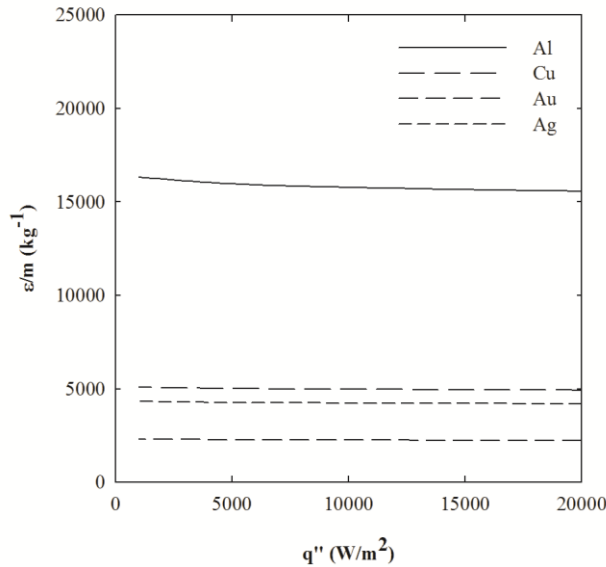


Figure 4.7. Fin Effectiveness per Unit Mass with Varying Material for the 90 ° Tree-Like Fin

The tree-like and rectangular fins previously utilized in the present analysis had a width-to-thickness ratio of 4. When compared to a width-to-thickness ratio of 4, width-to-thickness ratios of 8 and 16 result in a decrease in fin base area of 75 and 50 % respectively while width-to-thickness ratios of 1 and 2 result in an increase in fin base area of 100 and 300 % respectively. The thickness for the 90 ° tree-like fin was varied as can be seen in Table 4.5. Fin effectiveness as a function of width-to-thickness ratio for the 90 ° tree-like fin can be seen in Figure 4.8. The 90 ° tree-like fins with width-to-thickness ratios of 1, 2, 4, 8, and 16 had average heat transfer coefficients of 7.98, 8.60, 8.58, 8.49, and 8.14 W/m²K respectively.

Table 4.5. Varying Fin Thickness Area and Mass Properties

δ (cm)	w (cm)	Γ	A_b (cm ²)	A_s (cm ²)	m (g)
0.0625	1.0	16	0.0625	24.00	5.98
0.1250	1.0	8	0.1250	26.51	11.96
0.2500	1.0	4	0.2500	31.51	23.92
0.5000	1.0	2	0.5000	41.52	47.84
1.0000	1.0	1	1.0000	61.54	95.67

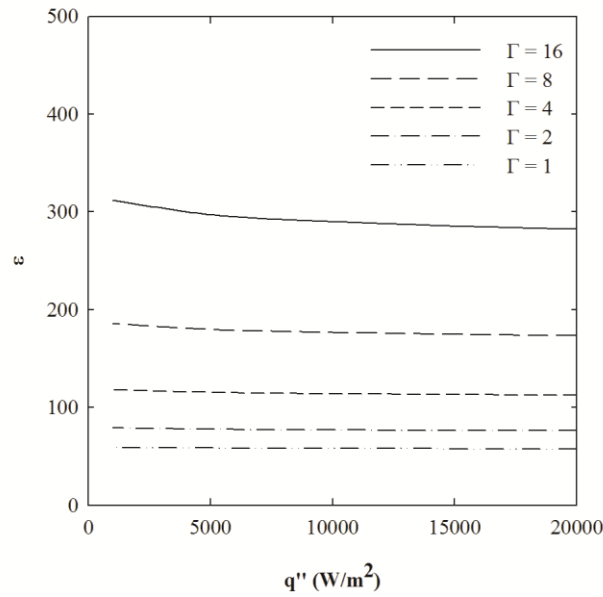


Figure 4.8. Fin Effectiveness with Varying Width-to-Thickness Ratio for the 90 ° Tree-Like Fin

The tree-like and rectangular fins previously employed were denoted as mesoscale fins whose geometric properties can be seen in Table 4.2. The 90 ° tree-like fin was the most effective fin and as such is the only fin scaled. The 90 ° tree-like fin was scaled up and down by a factor of 10 yielding the macroscale and microscale fins respectively. Fin effectiveness as a function of scale for the 90 ° tree-like fin can be seen in Figure 4.9. The microscale, mesoscale, and macroscale 90 ° tree-like fins had average heat transfer coefficients of 30.74, 8.58, and 5.67 W/m²K respectively.

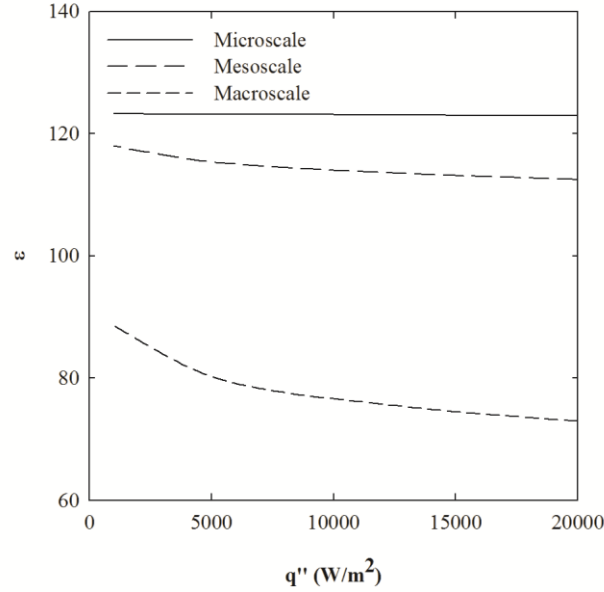


Figure 4.9. Fin Effectiveness with Varying Scales for the 90 ° Tree-Like Fin

The-tree like fins previously utilized in the present analysis had constant length and width scale ratios of $\beta = \gamma = 2^{-1/2}$. The length and width scale ratios of the 90 ° tree-like fin were varied by holding the length scale ratio constant and varying the width scale ratio as well as holding the width scale ratio constant and varying the length scale ratio. The dimensions and geometry of the 90 ° tree-like fin with varying width scale and length scale ratios can be seen in Table 4.6.

Table 4.6. Varying Length and Width Scale Ratios for the 90 ° Tree-Like Fin

k	L	w (cm)					w	L (cm)				
	(cm)	$\beta = n^{-1/4}$	$\beta = n^{-1/3}$	$\beta = n^{-1/2}$	$\beta = n^{-2/3}$	$\beta = n^{-3/4}$	(cm)	$\gamma = n^{-1/4}$	$\gamma = n^{-1/3}$	$\gamma = n^{-1/2}$	$\gamma = n^{-2/3}$	$\gamma = n^{-3/4}$
0	2.500	1.000	1.000	1.000	1.000	1.000	1.000	2.500	2.500	2.500	2.500	2.500
1	1.768	0.841	0.794	0.707	0.630	0.595	0.707	2.102	1.984	1.768	1.575	1.487
2	1.250	0.707	0.630	0.500	0.397	0.354	0.500	1.768	1.575	1.250	0.992	0.884
3	0.884	0.595	0.500	0.354	0.250	0.210	0.354	1.487	1.250	0.884	0.625	0.526

The tree-like fins with varying length scale can be seen in Figure 4.10 while the tree-like fins with varying width scale can be seen in Figure 4.11.

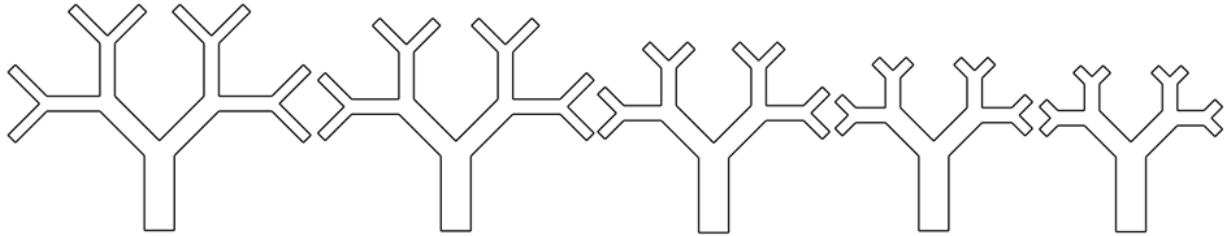


Figure 4.10. Varying Length Scale Ratio for the 90 ° Tree-Like Fin ($\beta = 2^{-1/2}$; $\gamma = 2^{-1/4}$, $\gamma = 2^{-1/3}$, $\gamma = 2^{-1/2}$, $\gamma = 2^{-2/3}$, and $\gamma = 2^{-3/4}$)

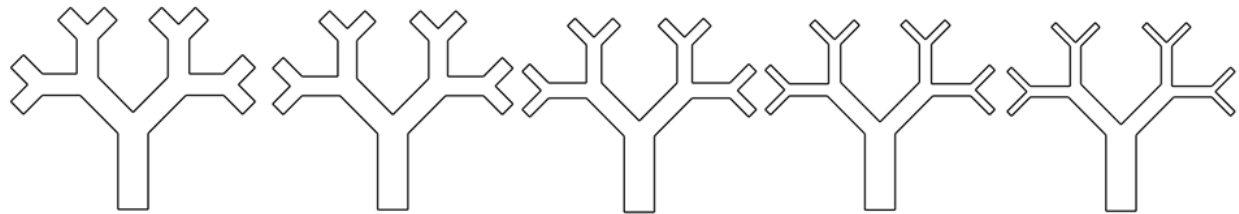


Figure 4.11. Varying Width Scale Ratio for the 90 ° Tree-Like Fin ($\gamma = 2^{-1/2}$; $\beta = 2^{-1/4}$, $\beta = 2^{-1/3}$, $\beta = 2^{-1/2}$, $\beta = 2^{-2/3}$, and $\beta = 2^{-3/4}$)

The 90 ° tree-like fin with a constant length scale ratio of $2^{-1/2}$ and width scale ratios of $2^{-1/4}$, $2^{-1/3}$, $2^{-1/2}$, $2^{-2/3}$, and $2^{-3/4}$ had average heat transfer coefficients of 7.76, 8.10, 8.58, 9.17, and 9.30 respectively. The 90 ° tree-like fin with a constant width scale ratio of $2^{-1/2}$ and length scale ratios of $2^{-1/4}$, $2^{-1/3}$, $2^{-1/2}$, $2^{-2/3}$, and $2^{-3/4}$ had average heat transfer coefficients of 8.33, 8.46, 8.58, 8.71, and 8.99 respectively. Fin effectiveness as a function of length and width scale ratio for the 90 ° tree-like fin can be seen in Figures 4.12 and 4.13.

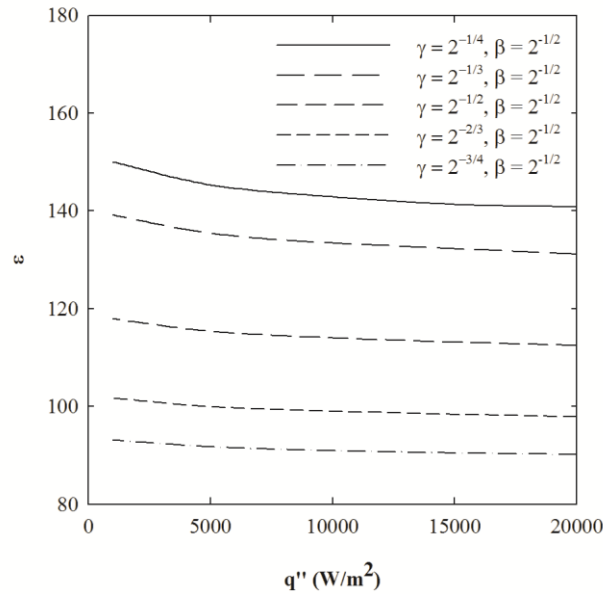


Figure 4.12. Fin Effectiveness as a Function of Length Scale Ratio for the 90 ° Tree-Like Fin

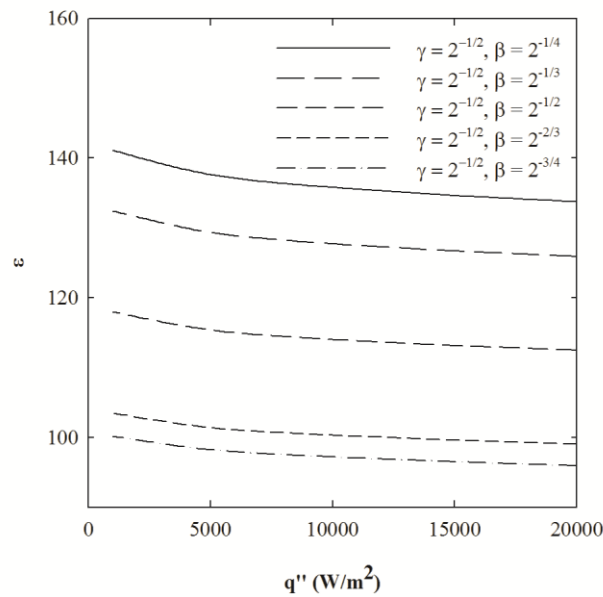


Figure 4.13. Fin Effectiveness as a Function of Width Scale Ratio for the 90 ° Tree-Like Fin

As previously mentioned, fin efficiency is defined as the ratio of the fin heat transfer rate to the heat transfer rate if the entire fin were at the base temperature. The geometry of the tree-like fins results in an increase in surface area when compared to the rectangular fins. The 30, 60

and 90 ° tree-like fins result in an increase in surface area of 12.24, 14.56, and 15.08 % respectively when compared with their rectangular fin counterparts. Fin efficiency as a function of heat flux for the 30, 60, and 90 ° tree-like and rectangular fins can be seen in Figure 4.14. The tree-like fins are more efficient than the rectangular fins regardless of bifurcation angle. The solid temperature gradient for the tree-like fins can be seen in Figure 4.15. The 30 ° tree-like fin is more efficient than the 60 and 90 ° tree-likes and has the largest temperature gradient across the fin.

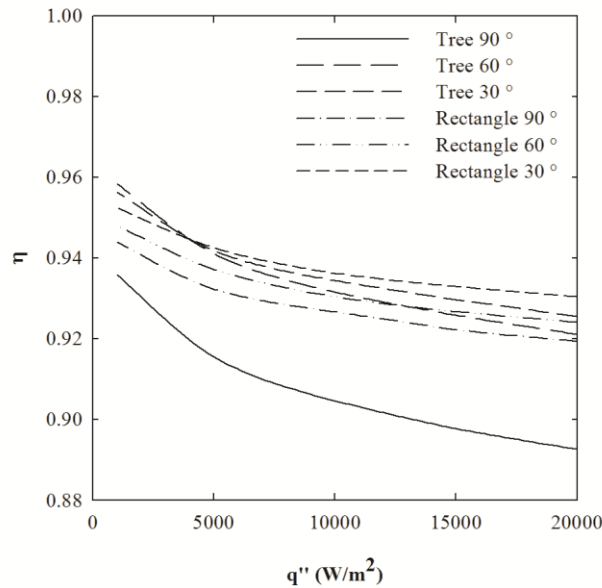


Figure 4.14. Fin Efficiency with Varying Heat Flux

The Grashof number is the ratio of buoyant to viscous forces and is defined as,

$$\text{Gr} = \frac{g\beta(T_s - T_\infty)L_c^3}{\nu^2} \quad (12)$$

The characteristic length of the tree-like fin was defined as the root of the surface area. The surface temperature of the fin was defined as the average of the base and tip temperatures. The average Grashof numbers for the 30, 60, and 90 ° tree-like fins were $2.30 \cdot 10^5$, $2.16 \cdot 10^5$, and

$2.14 \cdot 10^5$ respectively. Grashof numbers presented are an average over all heat fluxes. Fluid velocity isolines for the tree-like fins can be seen in Figure 4.16.

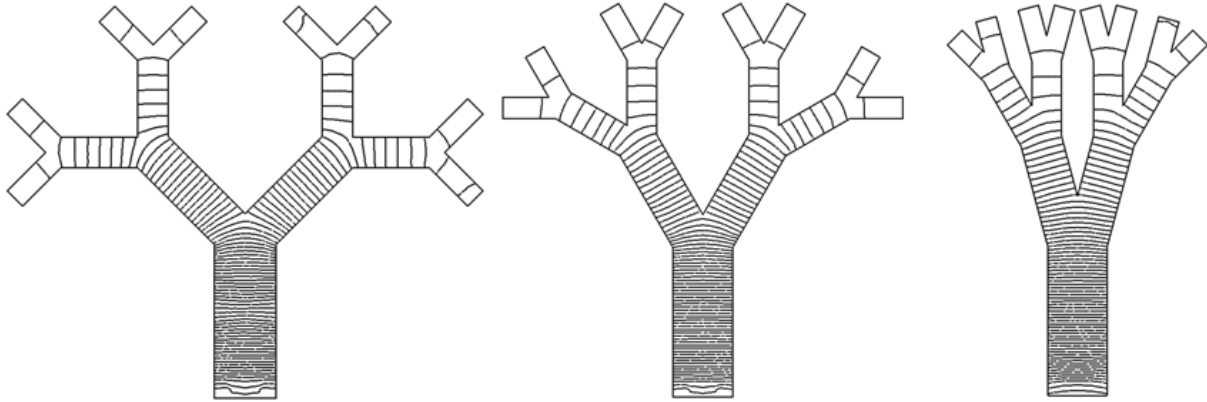


Figure 4.15. Tree-Like Fin Solid Temperature Isolines as a Function of Bifurcation Angle

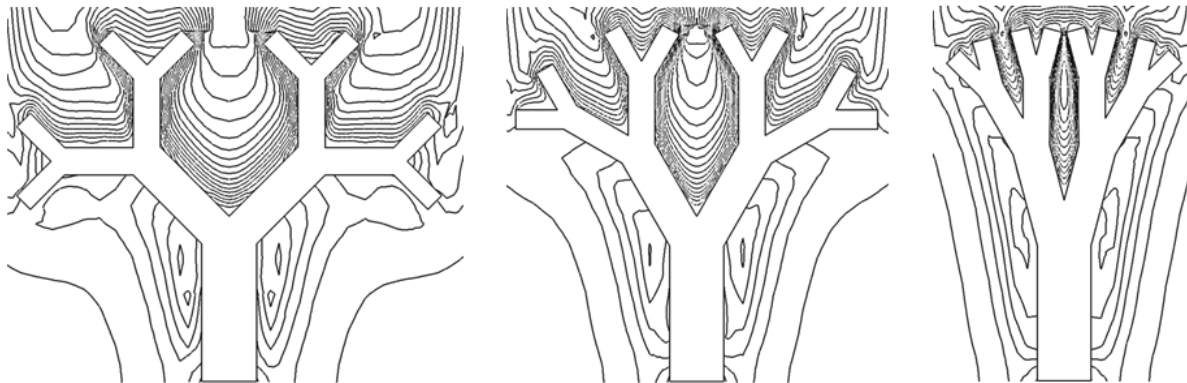


Figure 4.16. Tree-Like Fin Fluid Velocity Isolines as a Function of Bifurcation Angle

It should be noted that the figure is intended to capture flow behavior in the immediate vicinity of the tree-like fins and does not incorporate the entire computational domain utilized in the analysis. As the bifurcation angle decreases fluid interactions between branches at the same branch level also decrease. This effect is most prominent at the third branch level, $k = 0$, of the 30° tree-like fin where the small bifurcation angle between branches forms an effective blockage at the tip of the fin. A natural convective cell is also present at the center of the 30° tree-like fin where the innermost branches at the third branch level nearly meet.

As previously mentioned, at all heat fluxes studied the 90 ° tree-like fin was more effective than the 60 ° and 30 ° tree-like fins. Fin efficiency as a function of heat flux for the 90 ° tree-like fin of varying fin material can be seen in Figure 4.17. As with fin effectiveness, silver and copper have the highest efficiency for the conditions studied due to their relatively high thermal conductivities. The silver, copper, gold, and aluminum 90 ° tree-like fins had average Grashoff numbers of $2.09 \cdot 10^5$, $2.10 \cdot 10^5$, $2.11 \cdot 10^5$, and $2.14 \cdot 10^5$ respectively.

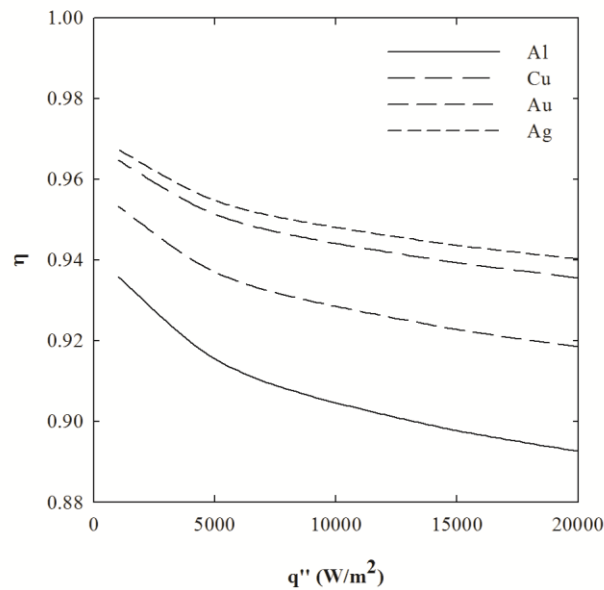


Figure 4.17. Fin Efficiency with Varying Material for the 90 ° Tree-Like Fin

The previously studied tree-like and rectangular fins had a width-to-thickness ratio of 4. Width-to-thickness ratios of 8 and 16 result in a decrease in fin surface area of 23.83 and 15.87 % respectively. Width-to-thickness ratios of 1 and 2 result in an increase in fin surface area of 31.77 and 95.30 % respectively. Fin efficiency as a function of width-to-thickness ratio for the 90 ° tree-like can be seen in Figure 4.18. While increasing width-to-thickness ratios results in increased fin effectiveness, fin efficiency decreases as a result of higher base temperatures. The 90 ° tree-like fins with width-to-thickness ratios of 1, 2, 4, 8, and 16 had average Grashoff

numbers of $1.26 \cdot 10^6$, $4.85 \cdot 10^5$, $2.14 \cdot 10^5$, $1.04 \cdot 10^5$, and $5.39 \cdot 10^4$ W/m²K respectively. Fluid velocity isolines for the tree-like fin with width-to-thickness ratios of 1, 4, and 16 can be seen in Figure 4.19.

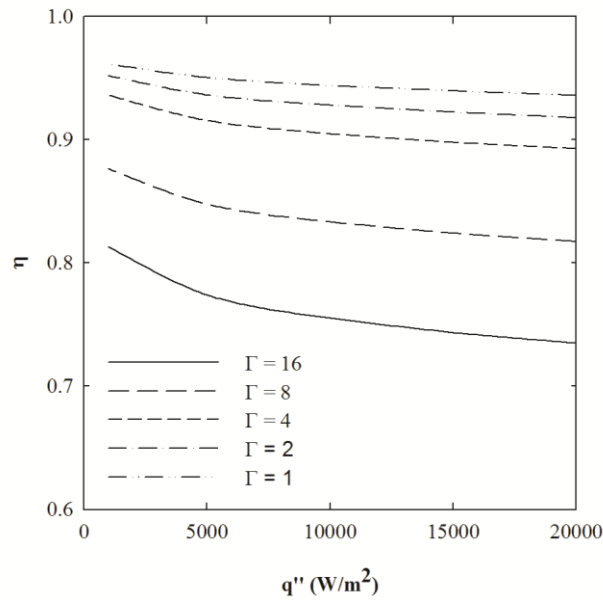


Figure 4.18. Fin Efficiency with Varying Width-to-Thickness Ratio for the 90 ° Tree-Like Fin

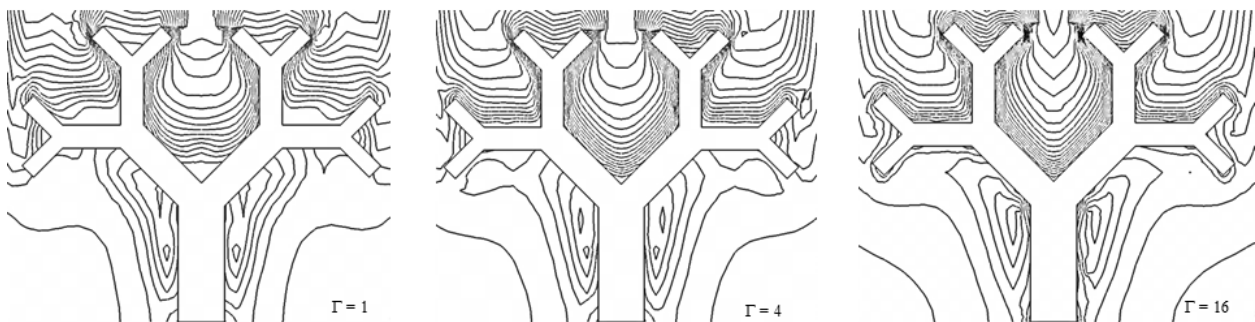


Figure 4.19. Tree-Like Fin Fluid Velocity Isolines with Varying Width-to-Thickness Ratio

Natural convective cells were found to become more prominent with increasing fin thickness. Flow separation around the edges of the fin increases with thickness as the fluid traveling along the face of the fin moves inward following the first bifurcation.

Fin efficiency as a function of scale for the 90° tree-like fin can be seen in Figure 4.20. The microscale, mesoscale, and macroscale 90° tree-like fins had average Grashof numbers of $6.20 \cdot 10^1$, $2.14 \cdot 10^5$, and $3.77 \cdot 10^8$ respectively. Fluid velocity isolines for the scaled 90° tree-like fins can be seen in Figure 4.21.

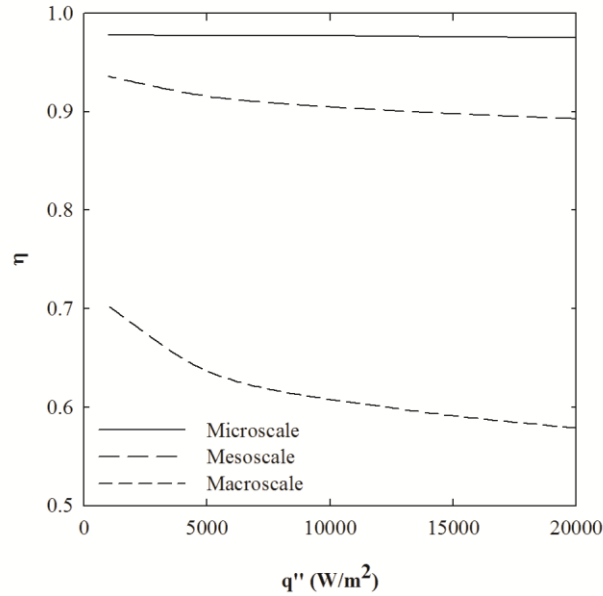


Figure 4.20. Fin Efficiency with Varying Scales for the 90° Tree-Like Fin

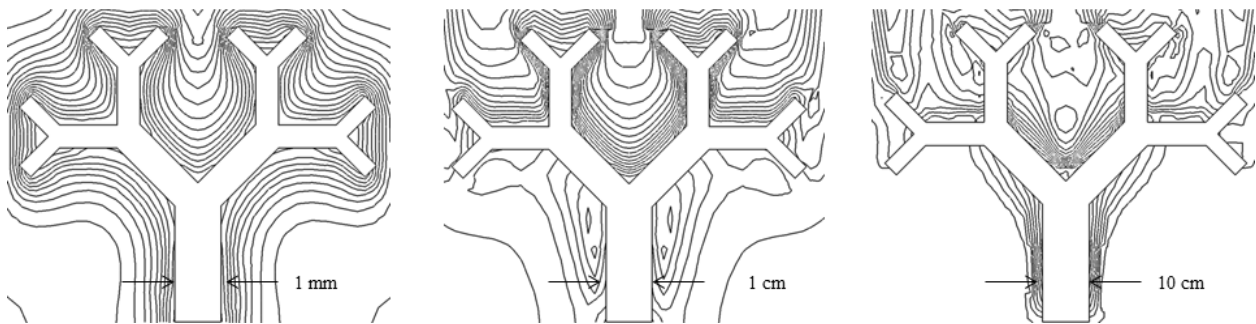


Figure 4.21 Scaled Tree-Like Fin Fluid Velocity Isolines

The microscale tree-like fin exhibits orderly flow behavior as viscous effects are dominant. The mesoscale tree-like fin exhibits similar flow behavior at the center of the fin as well as at the tips of the $k = 3c$, $3d$, $3e$, and $3f$ branches (please refer to Figure 4.1). The flow can more easily

escape through the center of the mesoscale tree-like fin due to the increase in gap size between the innermost branches. The mesoscale tree-like fin displays vortex shedding at the corners of the $k = 3a, 3b, 3g,$ and $3h$ branches. The macroscale tree-like fin exhibits vortex shedding at all fin tips and also displays natural convective cells between branch levels which are most prominent at the center and tips of the fin.

The-tree like fins previously analyzed had constant length and width scale ratios of $\beta = \gamma = 2^{-1/2}$. Holding the length scale ratio constant and varying the width scale ratio from its original value of $2^{-1/2}$ to $2^{-1/4}$ and $2^{-1/3}$ results in an increase in surface area of 22.51 and 14.04 % respectively. Similarly, holding the length scale ratio constant and varying the width scale ratio from its original value of $2^{-1/2}$ to $2^{-2/3}$ and $2^{-3/4}$ results in a decrease in surface area of 10.84 and 15.29 % respectively. Holding the width scale ratio constant and varying the length scale ratio from its original value of $2^{-1/2}$ to $2^{-1/4}$ and $2^{-1/3}$ results in an increase in surface area of 32.41 and 20.04 % respectively. Similarly, holding the width scale ratio constant and varying the length scale ratio from its original value of $2^{-1/2}$ to $2^{-2/3}$ and $2^{-3/4}$ results in a decrease in surface area of 15.19 and 21.35 % respectively. The 90° tree-like fin with a length scale ratio of $2^{-1/2}$ and width scale ratios of $2^{-1/4}, 2^{-1/3}, 2^{-1/2}, 2^{-2/3},$ and $2^{-3/4}$ had average Grashof numbers of $2.68 \cdot 10^5, 2.46 \cdot 10^5, 2.14 \cdot 10^5, 1.92 \cdot 10^5,$ and $1.81 \cdot 10^5$ respectively. The 90° tree-like fin with a width scale ratio of $2^{-1/2}$ and length scale ratios of $2^{-1/4}, 2^{-1/3}, 2^{-1/2}, 2^{-2/3},$ and $2^{-3/4}$ had average Grashof numbers of $2.54 \cdot 10^5, 2.40 \cdot 10^5, 2.14 \cdot 10^5, 1.92 \cdot 10^5,$ and $1.82 \cdot 10^5$ respectively. Fin efficiency as a function of length and width scale ratio for the 90° tree-like fin can be seen in Figures 4.22 and 4.23. As the length or width scale ratio increases fin efficiency increases.

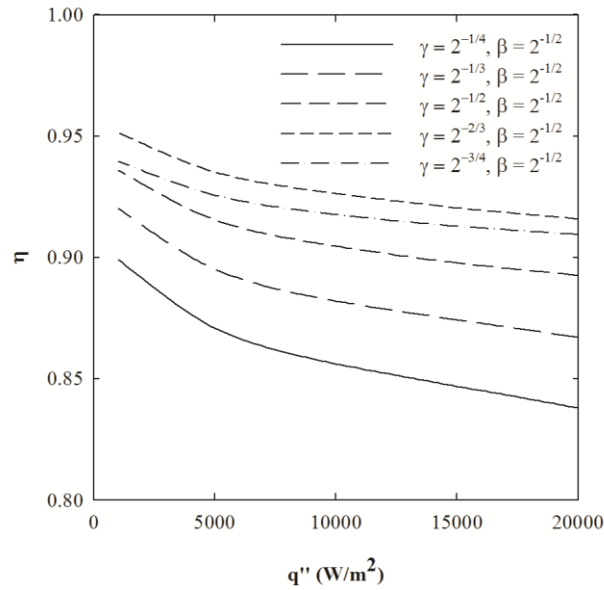


Figure 4.22. Fin Efficiency as a Function of Length Scale Ratio for The 90 ° Tree-Like Fin

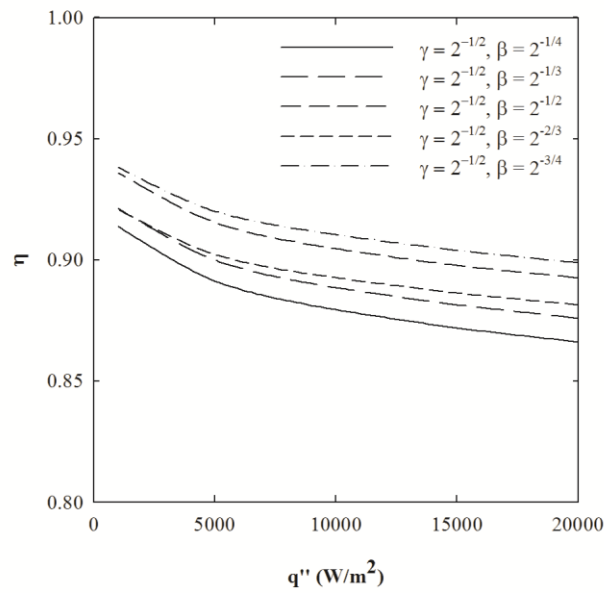


Figure 4.23. Fin Efficiency as a Function of Length Scale Ratio for the 90 ° Tree-Like Fin

The tree-like and rectangular fin base temperatures as a function of heat flux can be seen in Figure 4.24. Base temperatures, regardless of bifurcation angle and surface emissivity, are lower for the tree-like fins when compared to the rectangular fins. Though the tree-like and

rectangular fins have equal base areas as they have the same width and thickness, the tree-like fins have more surface area which results in lower base temperatures. The 90 ° tree-like fin had lower base temperatures at all heat fluxes when compared with the 60 ° and 30 ° tree-like fins as well as the rectangular fins.

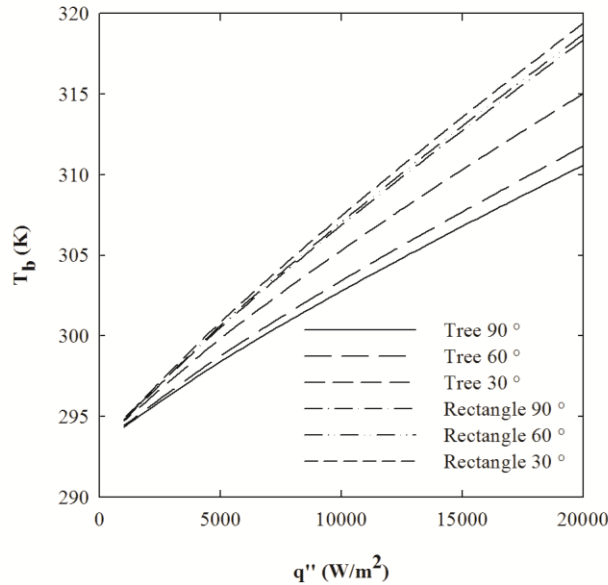


Figure 4.24. Fin Base Temperatures with Varying Heat Flux

Base temperatures as a function of heat flux and fin material for the 90 ° tree-like fins can be seen in Figure 4.25. Silver and copper had the lowest base temperatures attributed to their relatively high thermal conductivities when compared with the other materials studied. The fin base temperatures for the 90 ° tree-like fin with varying width-to-thickness ratio can be seen in Figure 4.26. The 90 ° tree-like fin with a width-to-thickness ratio of 16 had the highest base temperatures while the fin with a width-to-thickness ratio of 1 has the lowest base temperatures. The increase in base temperature with increasing width-to-thickness ratio is attributed to decreasing fin base surface area.

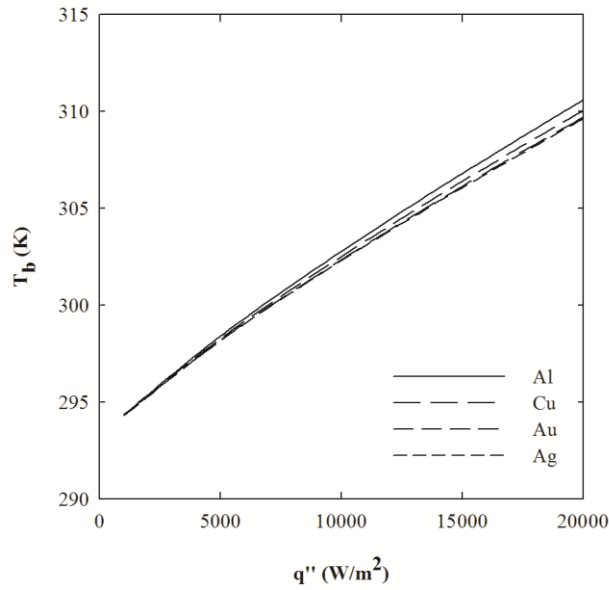


Figure 4.25. Fin Base Temperature for Varying Fin Material for the 90 ° Tree-Like Fin

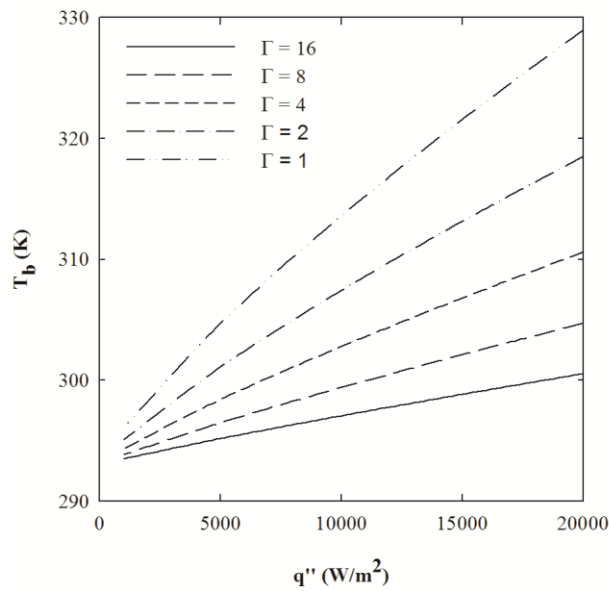


Figure 4.26. Fin Base Temperature for Varying Width-to-Thickness Ratio for the 90 ° Tree-Like Fin

Base temperatures as a function of heat flux for the microscale, mesoscale, and macroscale 90 ° tree-like fins can be seen in Figure 4.27. The microscale fin was found to have lower base

temperatures when compared to the mesoscale and macroscale fins. The microscale fin has a smaller thermal capacitance than the mesoscale and macroscale fins. The microscale fin's volume decreases by three orders of magnitude while the surface area decreases by two orders of magnitude when compared with the mesoscale fin which results in less thermal energy stored and thus lower solid temperatures.

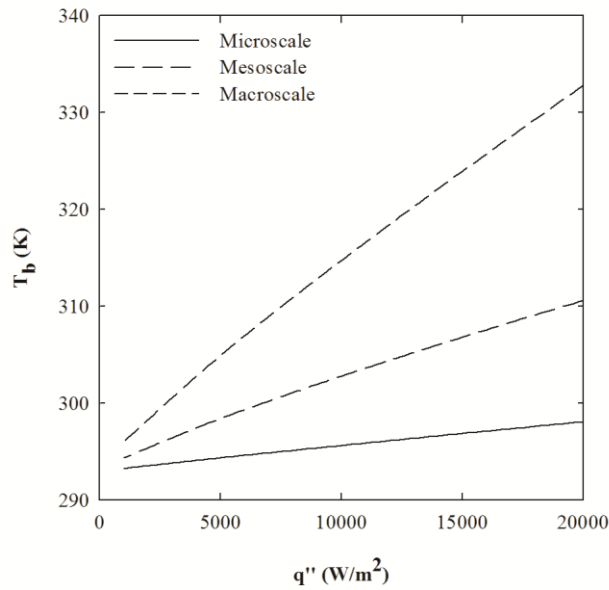


Figure 4.27. Fin Effectiveness with Varying Scales for the 90 ° Tree-Like Fin

Fin base temperatures as a function of length and width scale ratio can be seen in Figures 4.28 and 4.29. Varying the length scale ratio of the 90 ° tree-like fin has a greater impact on fin base temperature when compared with varying width scale ratio due to larger increases in fin surface area.

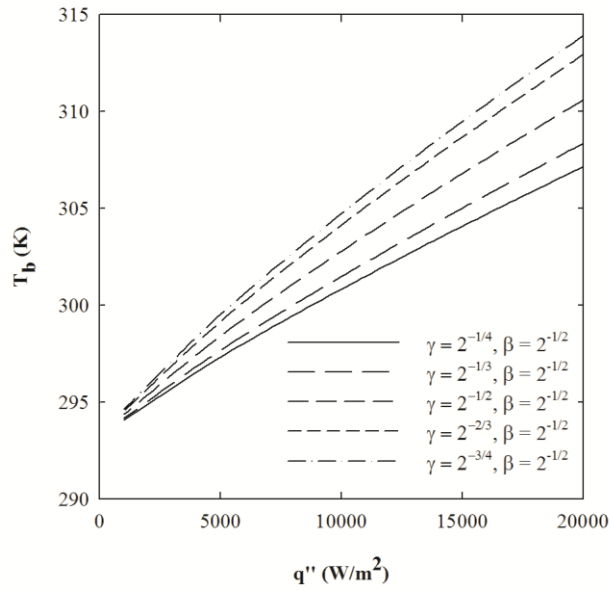


Figure 4.28. Fin Base Temperature as a Function of Length Scale Ratio for the 90 ° Tree-Like Fin

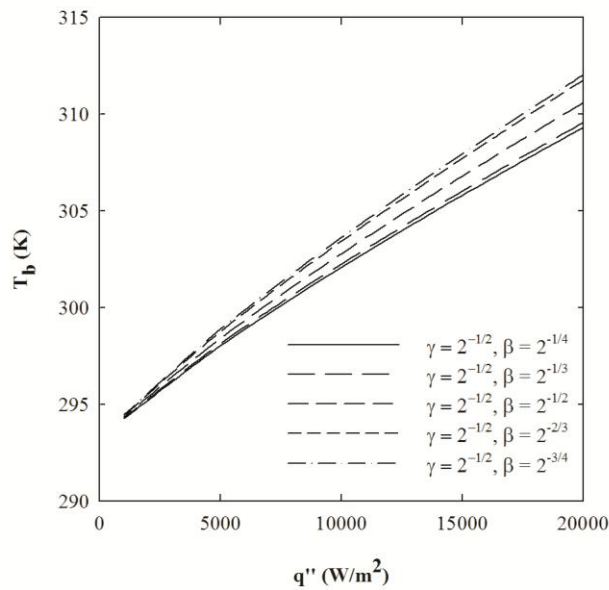


Figure 4.29. Fin Efficiency as a Function of Width Scale Ratio for the 90 ° Tree-Like Fin

Correlation

A computational correlation was employed in order to better quantify the performance of the tree-like fins. Four dimensionless groups, obtained using the Buckingham Pi Theorem [4.38], were used to correlate tree-like fin effectiveness. The dimensionless temperature ratio is defined as,

$$\phi = \frac{T_b - T_t}{T_b - T_\infty} \quad (4.13)$$

The ratio of the face surface area of the tree-like fin divided by the side surface area, which incorporates the fin thickness, is defined as,

$$\Lambda = \frac{A_f}{A_s} \quad (4.14)$$

The dimensionless bifurcation angle is defined as,

$$\theta = \text{rad}(\theta^\circ) \quad (4.15)$$

The constants were established through a minimization of the average error between the predicted fin effectiveness and the computational model fin effectiveness. The four aforementioned dimensionless parameters used to correlate the effectiveness of the tree-like fins can be seen in Equation 4.16.

$$\varepsilon = 69.754 \phi^{-0.671} \Lambda^{0.980} \theta^{0.150} \gamma^{1.73} \quad (4.16)$$

The correlation that can be seen in Figure 4.30 resulted in an average error of 0.91 % and a maximum error of 3.09 %. The correlation for fin effectiveness is largely a function of tree-like fin geometry. The Biot number, which is the ratio of the heat transferred by the fluid to the heat stored by the solid, and the Grashof number did not have an impact on the curve fitting utilized in the development of the correlation for fin effectiveness. Fin effectiveness is inversely proportional to, and a nonlinear function of, the dimensionless temperature ratio. Fin effectiveness is linearly proportional to the dimensionless surface area ratio as expected. The

dimensionless surface area ratio, by definition, incorporates the varying width-to-thickness ratios and scales. The correlation for fin effectiveness was found to be a weak function of bifurcation angle and width scale ratio but a strong function of length scale ratio.

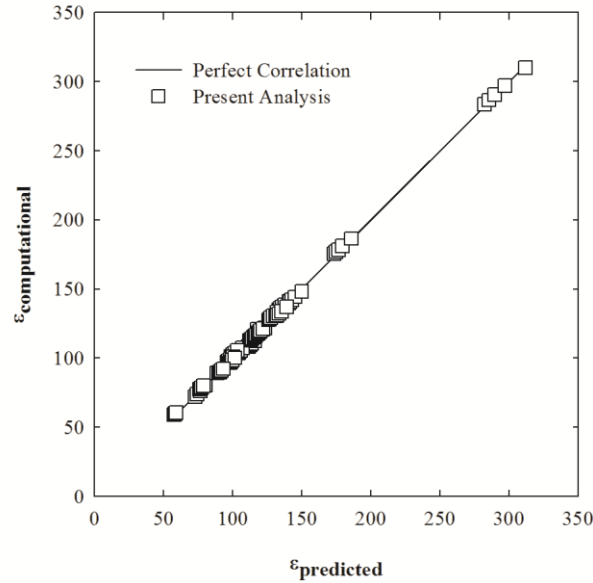


Figure 4.30. Tree-Like Fin Effectiveness Correlation

Conclusion

A validated and verified computational model has been developed to study the effects of fin geometry and scaling on fin effectiveness, efficiency and base temperature. The tree-like fins were found to be more effective than rectangular fins of equal mass, base area, and volume. Fin effectiveness was found to increase for the tree-like fins with bifurcation angle due to increased surface area. Fin effectiveness per unit mass was found to be highly dependent on material density and less dependent on material thermal conductivity. Fin effectiveness was found to be highest for fins with the largest width-to-thickness ratios as fin effectiveness is a function of base area. The microscale tree-like fin was more effective than the mesoscale and macroscale tree-like fins. Fin efficiency was found to decrease for the tree-like fins with bifurcation angle. Fin

efficiency was found to be highest for materials with relatively higher thermal conductivities. Fin efficiency was found to be highest for fins with the smallest width-to-thickness ratios as fin efficiency is a function of surface area. As with fin effectiveness, the microscale tree-like fin had the highest fin efficiency. The tree-like fins were found to have lower base temperatures than rectangular fins of equal mass, base area, and volume. Fin base temperatures were found to decrease with increasing bifurcation angle. Materials with relatively higher thermal conductivities had lower base temperatures. Fins with larger width-to-thickness ratios were found to have lower base temperatures. The microscale tree-like fin had lower base temperatures when compared with the mesoscale and macroscale tree-like fins. A correlation for the effectiveness of the tree-like fins developed which incorporated the various parameters investigated. The correlation had an average error of 1.02 %. The tree-like fins were found to offer greater thermal performance when compared with the rectangular fins of equal base area, mass, and volume as they were more effective at dissipating heat and had lower base temperatures.

Acknowledgements

Portions of this work were funded by the University of Alabama GK-12 Program. The GK-12 Program is supported by the National Science Foundation under grant 0742504.

References

- [4.1] Aziz, A., 1992, "Optimum Dimensions of Extended Surfaces Operating in a Convective Environment," *Applied Mechanics Reviews*, 45(5), pp. 155-173.
- [4.2] Kraus, A. D., 1999, "Developments in the Analysis of Finned Arrays," *International Journal of Transport Phenomenon*, 1, pp. 141-164.
- [4.3] Mikk, I., 1980, "Convective Fin of Minimum Mass," *International Journal of Heat and Mass Transfer*, 23(5), pp. 707-711.
- [4.4] Mao, J., Rooke, S., 1994, "Transient Analysis of Extended Surfaces with Convective Tip," *International Communications in Heat and Mass Transfer*, 32(1), pp. 85-94.
- [4.5] Leong, K. C., Kooi, T. C., 1996, "Natural Convection from a Vertical Rectangular Fin," *Experimental Heat Transfer*, 9(4), pp. 287-303.
- [4.6] Razelos, P., Georgiou, E., 1992, "Two-Dimensional Effects and Design Criteria for Convective Extended Surfaces," *Journal of Heat Transfer Engineering*, 13(3), pp. 36-48.
- [4.7] Thompson, D'A. W., 1942, *On Growth and Form*, Cambridge University Press, Cambridge.
- [4.8] Mandelbrot, B. B., 1982, *The Fractal Geometry of Nature*, Freeman, New York.
- [4.9] Barnsley, M., 1988, *Fractals Everywhere*, Academic Press, San Diego.
- [4.10] Murray, C. D., 1926, "The Physiological Principle of Minimum Work. I. The Vascular System and the Cost of Blood Volume," *Journal of Physiology*, 12(3), pp. 207-214.
- [4.11] Cohn, D. L., 1954, "Optimal Systems: the Vascular System," *Bulletin of Mathematical Biophysics*, 16, pp. 59-74.
- [4.12] Calamas, D., Baker, J., 2012, "Performance of a Biologically-Inspired Heat Exchanger with Hierarchical Bifurcating Flow Passages," *Journal of Thermophysics and Heat Transfer*, Accepted for Publication.
- [4.13] Van Der Vyver, H., 2003, "Validation of a CFD Model of a Three-Dimensional Tube-in-Tube Heat Exchanger," *Proceedings of the Third International Conference on CFD in the Minerals and Process Industries*, CSIRO, Melbourne, Australia, pp. 235-240.
- [4.14] Meyer, J., Van Der Vyver, H., 2005, "Heat Transfer Characteristics of a Quadratic Koch Island Fractal Heat Exchanger," *Heat Transfer Engineering*, 26(9), pp. 22-29.

- [4.15] Bonjour, J., Rocha, L. A. O., Bejan, A., Meunier, F., 2004, "Dendritic Fins Optimization for a Coaxial Two-Stream Heat Exchanger," *International Journal of Heat and Mass Transfer*, 47(1), pp. 111-124.
- [4.16] Lee, D. J., Lin, W. W., 1995, "Second Law Analysis on Fractal-Like Fin under Crossflow," *AIChE Journal*, 41(1), pp. 2314-2317.
- [4.17] Lin, W. W., and Lee, D. J., 1997, "Diffusion-Convection Process in a Branching Fin, *Chemical Engineering Communications*," 158(1), pp. 59-70.
- [4.18] Xu, P., Yu, B., Yun, M., Zou, M., 2006, "Heat Conduction in Fractal Tree-Like Branched Networks," *International Journal of Heat and Mass Transfer*, 49, pp. 3746-3751.
- [4.19] Plawsky, J. L., 1993, "Transport in Branched Systems I: Steady-State Response," *Chemical Engineering Communications*, 123(1), pp. 71-86.
- [4.20] Plawsky, J. L., 1993, "Transport in Branched Systems II: Transient response," *Chemical Engineering Communications*, 123(1), pp. 87-109.
- [4.21] Bejan, A., 1997, "Constructal-Theory Network of Conducting Paths for Cooling a Heat Generating Volume," *International Journal of Heat and Mass Transfer*, 40(4), pp. 799-816.
- [4.22] Bejan, A., Lorente, S., 2010, "The Constructal Law of Design and Evolution in Nature," *Philosophical Transactions of the Royal Society B*, 365(1545), pp. 1335-1347.
- [4.23] Bejan, A., Lorente, S., 2006, "Constructal Theory of Generation of Configuration in Nature and Engineering," *Journal of Applied Physics*, 100(4).
- [4.24] Almogbel, M. A., 2005, "Constructal Tree-Shaped Fins," *International Journal of Thermal Sciences*, 44(4), pp. 342-348.
- [4.25] Lorenzini, G., Rocha, L. A. O., 2006, "Constructal Design of Y-Shaped Assembly of Fins," *International Journal of Heat and Mass Transfer*, 49(23-24), pp. 4552-4557.
- [4.26] Bejan, A., Dan, N., 1999, "Two Constructal Routes to Minimal Heat Flow Resistance via Greater Internal Complexity," *Journal of Heat Transfer*, 121(1).
- [4.27] Calamas, D., Baker, J., 2012, "Behavior of Thermally Radiating Tree-Like Fins," *Journal of Heat Transfer*, Accepted for Publication.
- [4.28] Reid, R. C., Prausnitz, J. M., Poling, B. E., 1987, *The Properties of Gases and Liquids*, 2nd ed., McGraw-Hill, New York.

- [4.29] Glowinski, R., Le Tallec, P., 1989, Augmented Lagrangian Methods and Operator-Splitting Methods in Nonlinear Mechanics, SIAM, Philadelphia.
- [4.30] Marchuk, G. I., 1982, Methods of Numerical Mathematics, Springer-Verlag, Berlin.
- [4.31] Samarskii, A. A., 1989, Theory of Difference Schemes, Nauka, Moscow.
- [4.32] Roach, P. J., 1998, Technical Reference of Computational Fluid Dynamics, Hermosa Publishers, Albuquerque.
- [4.33] Hirsch, C., 1988, Numerical Computation of Internal and External Flows, John Wiley and Sons, Chichester.
- [4.34] Patankar, S. V., 1980, Numerical Heat Transfer and Fluid Flow, Hemisphere, Washington D.C.
- [4.35] Kern, D. Q., and Kraus, A. D., 1972, Extended Surface Heat Transfer, McGraw-Hill, New York, pp. 203-211.
- [4.36] Fox, R. W., and McDonald, A. T., 1992, Introduction to Fluid Mechanics, 4th ed., John Wiley & Sons, New York.

CHAPTER 5

EXPERIMENTAL PERFORMANCE OF A SOLID HEAT EXCHANGER WITH TREE-LIKE FLOW PASSAGES*

Abstract

System performance of a solid single fluid compact heat exchanger with tree-like flow passages has been experimentally examined. The results, presented in the form of commonly defined dimensionless parameters, demonstrate that system performance can be characterized in a mode similar to traditional compact heat exchanger designs. Pressure forces were found to dominate inertia forces at low Reynolds numbers. Correlations of the Euler number, Nusselt number, Colburn factor, and friction factor as a function of Reynolds number were utilized in order to compare system performance to traditional two fluid compact heat exchangers.

Introduction

Utilizing biologically-inspired solutions for engineering applications is known as biomimetics. In biological systems, tree-like flow passages produce space-filling flow networks, minimize flow resistance, and enhance surface area to volume ratios. Biologically-inspired flow passages could thus yield improved system performance when utilized in compact heat exchangers. Tree-like flow networks have many advantages when compared to traditional parallel flow networks. Tree-like flow networks have greater surface area for heat transfer per unit volume when compared with traditional parallel flow compact heat exchangers. Additional

* Note. This chapter is based on Calamas, D., and Baker, J., 2013, "Experimental Performance of a Solid Heat Exchanger with Tree-Like Flow Passages," *Experimental Heat Transfer* (Submitted for Publication).

advantages of tree-like flow networks when compared to parallel flow networks consist of lower total pressure drop as well as lower, more uniform, maximum wall temperatures.

Murray [5.1] investigated the principle of minimum work in the human vascular system and concluded there is an optimal change in hydraulic diameter at bifurcations in bifurcating flow networks that minimizes flow resistance. When Murray's Law is obeyed, parent and daughter branches are connected in a way that theoretically provides bulk fluid transport for the least amount of work. West et al. [5.2-5.4] developed scaling laws for fluid transport through space-filling tree-like networks based on three assumptions: a tree-like branching network is required to supply an entire volume, the final branch level is size invariant, and the energy required to supply the flow network is minimized. Bejan [5.5] developed a solution for optimizing conducting paths for application in cooling a heat generating volume and found the paths form a tree-like network. Bejan's optimization technique, known as "constructal theory," states that finite-volume systems evolve to afford easier access to the imposed currents that flow through it which explains the natural tendency of flow systems to evolve toward greater flow access [5.6, 5.7]. Bejan's constructal theory, extended to fins in convection heat transfer, was found to result in increased thermal performance when compared to traditionally employed extended surfaces [5.8-5.11]. Calamas and Baker [5.12] investigated the thermal performance of tree-like fins in a naturally convecting environment and found the tree-like fins were more effective when compared with rectangular fins of equal mass, volume, and base area. Similarly, Calamas and Baker [5.13] investigated the performance of tree-like fins thermally radiating to free space and concluded the tree-like fins were more effective than rectangular fins of equal mass, volume, and base area.

Tuckerman and Pease [5.14] first proposed the use of high-performance microchannel heat sinks with high surface area to volume ratios for the cooling of planar circuits and concluded the use of microscale channels were advantageous for laminar flow as the heat transfer coefficient scales inversely with channel width. Pence [5.15] compared a microscale heat sink with a tree-like-like flow network to a heat sink with a parallel channel flow network of equal surface area, pumping power, and flow rate. Pence concluded the tree-like-like network resulted in lower total pressure drop and maximum wall temperatures. Pence [5.16] compared a square shaped heat sink with a parallel channel flow network to a disk shaped heat sink with a tree-like-like branching flow network of equal surface area for heat transfer and found the tree-like-like flow network resulted in increased thermal efficiency. Alharbi et al. [5.17] found that tree-like-like flow networks result in a lower total pressure drop when compared to parallel channel flow networks due to local pressure recovery at bifurcations that result from an increase in flow area. Alharbi et al. [5.18] similarly found that a tree-like-like flow network resulted in a more uniform surface temperature when compared with a parallel channel flow network for the same maximum wall temperature. Wang et al. [5.19] found that an increased number of parent channels emanating from the center of a disk shaped heat sink and an increased number of branch levels resulted in increased temperature uniformity. Senn and Poulikakos [5.20] found a tree-like branching flow network with six branch levels offered almost half the total pressure drop when compared with a serpentine flow pattern of equal surface area and inlet Reynolds number. Calamas and Baker [5.21] investigated the effect of scaling on microscale tree-like flow networks and found mesoscale tree-like flow networks offered similar thermal performance while also resulting in reduced pressure drop.

Incorporating hierarchical bifurcating flow passages in heat exchangers is a relatively new topic that has not been studied extensively in the past. Bejan [5.22] utilized constructal theory in the design of a dendritic heat exchanger with the objective of minimizing pumping power and maximizing thermal performance and found the tree-like heat exchanger resulted in increased system performance when compared with traditional parallel channel heat exchangers. Similarly, da Silva et al. [5.23] and Zimparov et al. [5.24] utilized constructal theory in the design of heat exchangers. da Silva and Bejan [5.23] experimentally investigated the hydraulic and thermal behavior of a dendritic counterflow heat exchanger. da Silva and Bejan concluded that as the flow rate increased the effect of asymmetric bifurcations on flow division also increased which resulted in decreased temperature uniformity. Zimparov et al. [5.24] presented a geometric optimization of constructal tree-shaped parallel flow heat exchangers with several different configurations and levels of complexity. Zimparov et al. concluded as the level of complexity increases the performance curves of different flow structures will eventually converge. Azad and Amidpour [5.25] employed constructal theory in the economic optimization of a shell and tube heat exchanger and concluded the constructal design resulted in a 50% reduction in total cost when compared with the traditional method of design. Raja et al. [5.26] utilized constructal theory in the design of a multi-block heat exchanger and concluded the constructal heat exchangers were 20% more effective when compared to conventional crossflow heat exchangers. Zhang et al. [5.27] presented the conditions where tree vascularization offered smaller global thermal resistance when compared with conventional parallel channels in counterflow heat exchangers. Zhang et al. found fluid outlet temperature uniformity decreased as the level of complexity increased. Zamfirescu and Bejan [5.28] presented optimized flow structures for constructal tree-shaped networks with an evaporating refrigerant as the working

fluid. Bonjour et al. [5.29] compared branched and radial fins in a coaxial two-stream heat exchanger and concluded the benefit of branched fins was highly dependent on the size of the heat exchanger cross-section.

The purpose of this paper is to assess the system performance of a single fluid compact heat exchanger with tree-like flow passages. Due to the design of the tree-like flow passages the working fluid will be transported through both expanding and contracting tree-like flow networks. It is hypothesized the use of the tree-like flow passages will offer improved system performance when compared with traditional compact heat exchangers.

Experimental Investigation

In this study tree-like disks were used to transport the working fluid through tree-like flow networks in a solid heat exchanger. Each tree-like disk is characterized by 4 tree-like flow networks located on both sides of the disk as can be seen in Figure 5.1.

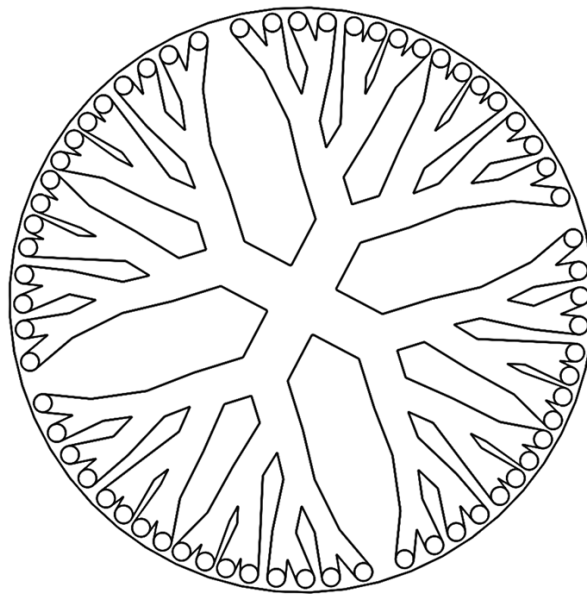


Figure 5.1. Single Tree-Like Disk

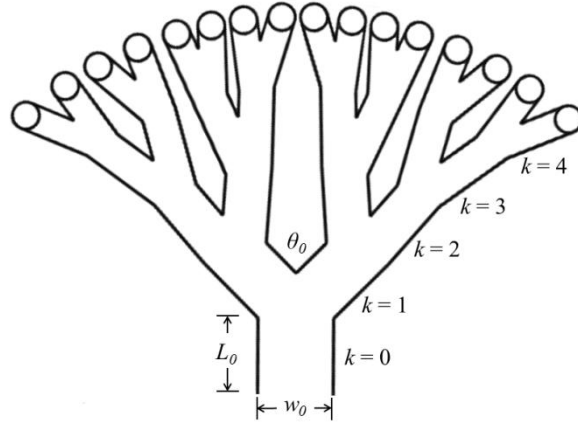


Figure 5.2. Nomenclature Describing Tree-Like Flow Passages

The following branch scale ratios were utilized as recommended by West et al. [5.3] and Alharbi et al. [5.14] to describe the tree-like branching flow networks inside the tree-like disks,

$$\gamma = \frac{L_{k+1}}{L_k} \quad (5.1)$$

$$\beta = \frac{W_{k+1}}{W_k} \quad (5.2)$$

The nomenclature describing the tree-like internal flow networks can be seen in Figure 5.2. The first branch stemming from the inlet plenum at the center of the disk is defined as the zeroth-order branch, where $k = 0$, and the last branch is defined as the fourth-order branch, where $k = 4$. In the present analysis, $n = 2$ as each parent channel bifurcates into 2 daughter channels. The tree-like channels bifurcate symmetrically at all branch levels. The bifurcation angle is denoted as the angle between two branches at the same branch level. The dimensions that describe the branching for a single tree-like disk can be seen in Table 5.1. Due to machining tolerances the bifurcation angles presented are an average of the bifurcation angles at each branch level. The tree-like disks have a radius of 5.08 cm and a thickness of 1.27 cm.

Table 5.1. Heat Exchanger Tree-Like Disk Geometry

k	n	w (mm)	β	L (mm)	γ	H (mm)	θ ($^{\circ}$)
0	4	8.80	0.78	8.98	0.99	6.35	-
1	8	6.82	0.77	8.91	1.00	6.35	90.00
2	16	5.29	0.78	8.88	1.09	6.35	45.00
3	32	4.10	0.77	9.71	0.85	6.35	32.48
4	64	3.18	-	8.30	-	6.35	30.16

The heat exchanger is composed of several critical components, an exploded view of which can be seen in Figure 5.3. The heat exchanger consists of 4 aluminum tree-like disks, 3 aluminum spacer disks, an aluminum cylindrical enclosure, and 2 aluminum end caps. Each tree-like disk is separated by a single spacer disk. Each spacer disk has an integrated o-ring which ensured a proper seal with the inside of the cylindrical enclosure and a 0.635 cm inlet plenum.

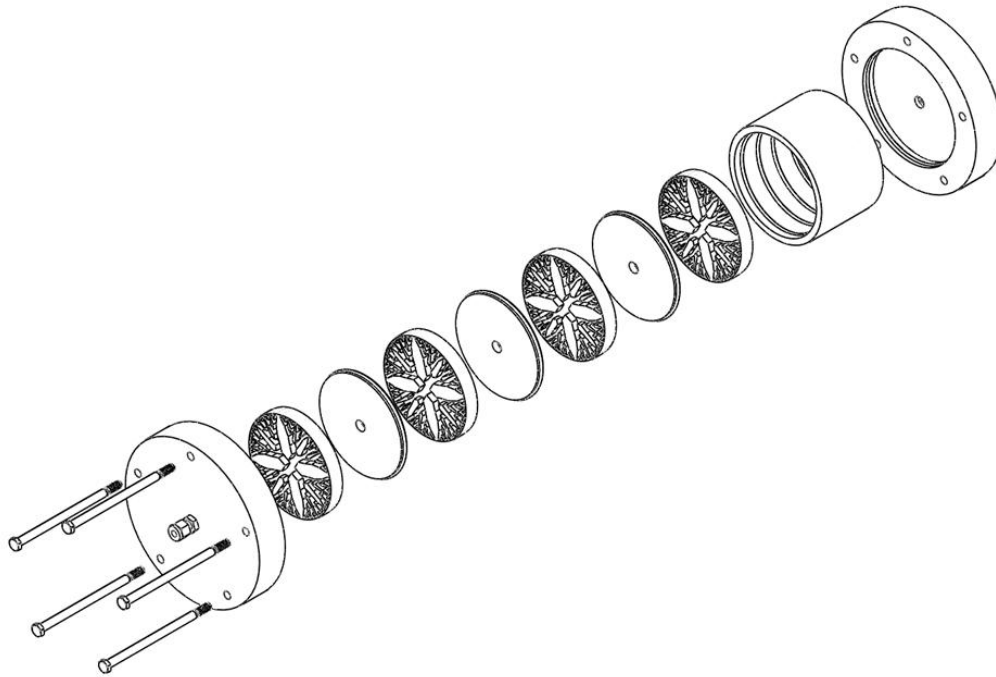


Figure 5.3. Exploded View of Heat Exchanger

The tree-like and spacer disks are enclosed by the cylindrical aluminum shell. The 2 end caps, which also incorporate o-rings that ensure a proper seal with the outside of the cylindrical enclosure, are fastened together using heavy hex bolts. Each end cap has an integrated Swagelok fitting for inflow and outflow. The fluid temperature and pressure drop were measured at the inlet and outlet of the heat exchanger.

The working fluid, water, initially enters the heat exchanger through the fitting located at the center of the first end cap. The fluid enters the center of the first tree-like disk through the inlet plenum located on the end cap. The fluid flows radially outward from the $k = 0$ branch level to the $k = 4$ branch level. The fluid then passes through the tree-like disk and flows radially inward from the $k = 4$ branch level to the $k = 0$ branch level. The flow passes through the inlet plenum of the first spacer disk and subsequently flows radially outward through the second tree-like disk. This process is repeated until the fluid has travelled radially outward and then back inward through the four tree-like disks after which the fluid exits through the last Swagelok fitting located on the second end cap.

As a second separate experiment, the pressure drop across a single tree-like disk was measured. A single aluminum tree-like disk was enclosed by two acrylic end caps and an acrylic cylindrical enclosure as can be seen in Figure 5.4. The enclosure was secured with hex bolts and the fluid was transported to and from the assembly through Swagelok fittings located on the acrylic end caps. When performing the second experiment, the single tree-like disk assembly in Figure 5.4 is substituted for the heat exchanger assembly in Figure 5.3 utilized in the first experiment. All other experimental equipment remains constant.

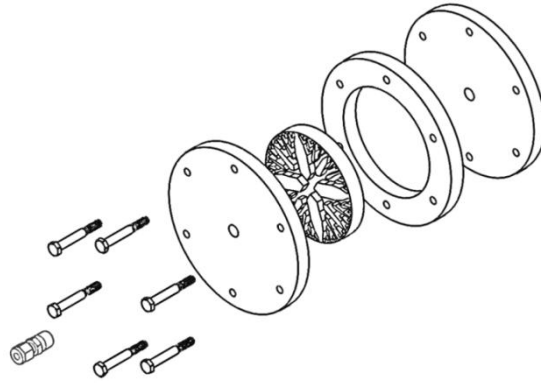
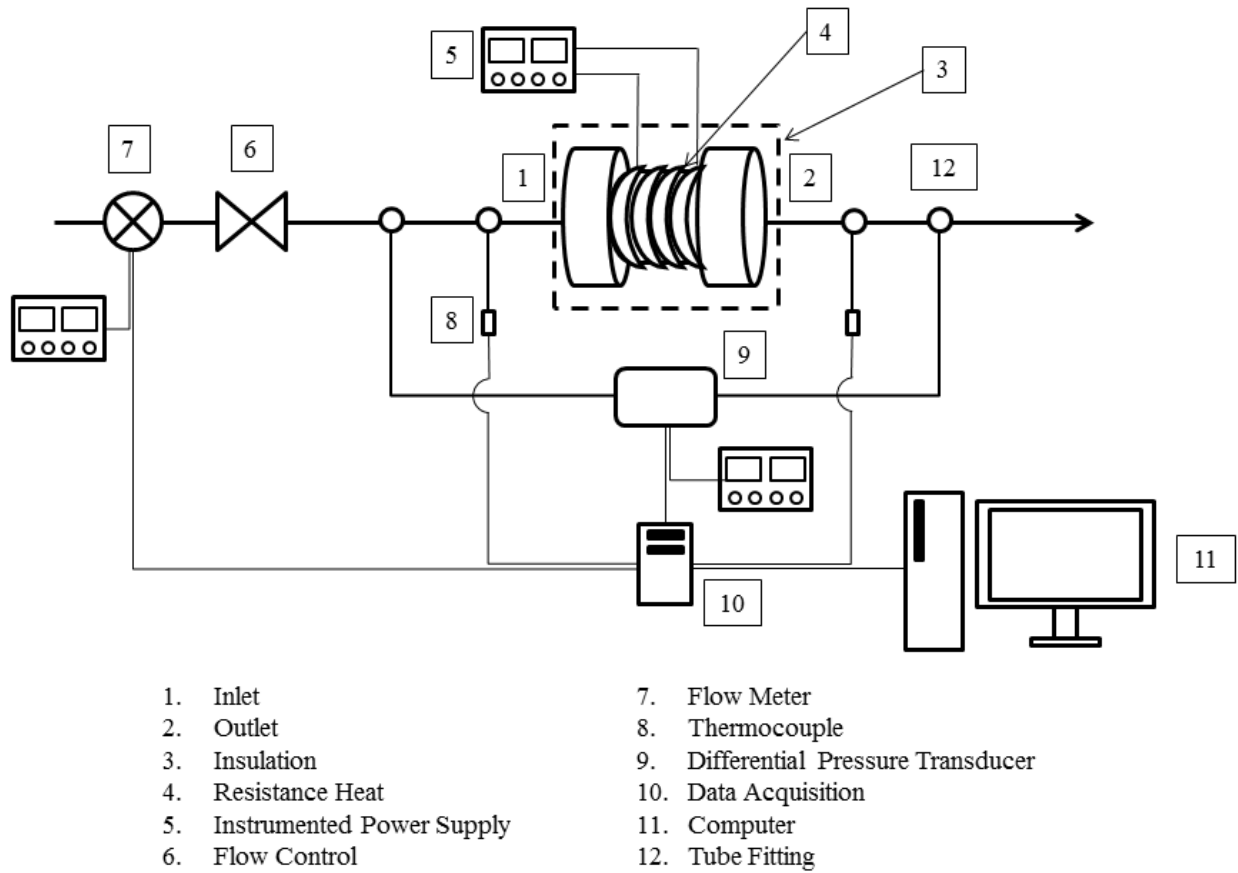


Figure 5.4. Exploded View of Single Disk Enclosure

Experimental Methods

A schematic of the experimental setup can be seen in Figure 5.5.



- | | |
|------------------------------|-------------------------------------|
| 1. Inlet | 7. Flow Meter |
| 2. Outlet | 8. Thermocouple |
| 3. Insulation | 9. Differential Pressure Transducer |
| 4. Resistance Heat | 10. Data Acquisition |
| 5. Instrumented Power Supply | 11. Computer |
| 6. Flow Control | 12. Tube Fitting |

Figure 5.5. Experimental Schematic

For this experiment, 0.635 cm PVC and stainless steel tubing were used to transport water, the working fluid. The inflow passed through an Omega FLR1013 Series flow meter. The flow meter was connected to an Omega FLR1000-PW 115 VAC dual power supply. A Swagelok NUPRO needle valve was used to adjust the flow rate. An Omega PX157 Series differential pressure transducer was connected to a Murr Elektronik MCS10-115-230/24 Power⁺ Series single phase switch mode power supply to measure the fluid's pressure drop across the heat exchanger. Inlet and outlet fluid temperatures were measured with Omega T-type thermocouples. The Omega PX157 Series differential pressure transducer and the Omega T-type thermocouples utilized Swagelok T unions set inline at the inlet and outlet of the heat exchanger as can be seen in Figure. 5.5. A National Instruments NI cDAQ-9174 compact data acquisition system was used to record measurements from the two type T thermocouples as well as the Omega FLR1013 Series flow meter and the Omega PX157 differential pressure transducer. National Instruments LabVIEW 2011 was the system design software utilized to interface with the computer and the data acquisition system. An Omega SRT101-100 522 W 120 VAC silicone rubber heater tape was used to supply a heat rate to the heat exchanger. The heat rate was adjusted using a Staco Energy Products 120 V variable transformer. As previously mentioned, the heat exchanger itself is composed of four disks with hierarchical bifurcating patterns on each side. Three spacer disks with 0.635 cm holes through their centers separate the four tree-like disks. The four tree-like and three spacer disks were enclosed in a cylindrical aluminum enclosure wrapped with Omega SRT101-100 silicone rubber heater tape and secured with two aluminum end caps. Frost King FV15H pipe wrap insulation encased the entire heat exchanger and was secured using Nashua 322 foil tape.

The solid heat exchanger was experimentally tested at 5 different flow rates: 1, 1.5, 2, 2.5, and 3 lpm. The solid heat exchanger was also experimentally tested for 4 different heat rates: 200, 300, 400, and 500 W. Each flow rate and corresponding heat rate was experimentally tested 5 times to measure and record experimental uncertainty. The fluid volume for each tree-like disk was calculated by enclosing a randomly chosen tree-like disk with a spacer disk on each side. The inlet plenum for one spacer disk was closed off. A syringe was used to fill the tree-like disk with water. The fluid volume was measured and the process was repeated 10 times. The average fluid volume of a tree-like disk was found to be 57.7 cm^3 .

Experimental Uncertainty

A statistical analysis was utilized to calculate the sample standard deviation and mean of the experimental data for various performance characteristics. The sample standard deviation for a performance characteristic was dependent upon its mean value as well as the number of samples. A Student's t distribution was utilized to provide the probability density function as the number of samples was less than 30. A 95% confidence interval was subsequently calculated for the various heat exchanger performance characteristics as recommended by Wheeler and Ganji [5.30]. The accuracy of the FLR1013 flow meter is $\pm 1 \%$ full scale. The accuracy of the PX157 differential pressure transducer is $\pm 0.75 \%$ full scale. The maximum uncertainty in the differential pressure experimental measurements was found to be 4.9 %. The standard limit of error for the Type T thermocouples is 0.75 %. The maximum uncertainty in the fluid temperature experimental measurements was found to be 2.7 %. The uncertainty in the fluid volume measurement of a single tree-like disk was found to be 1.0 %.

Calculations

For a sufficient analysis of the mesoscale tree-like heat exchanger's performance it was necessary to quantify the results in a manner that could be easily compared to traditional compact heat exchangers. Fluid properties, assumed to be constant in all calculations, were evaluated at 293 K. The inlet Reynolds number is the ratio of inertia to viscous forces and was calculated as follows,

$$Re = \frac{uD}{\nu} \quad (5.3)$$

The diameter, D , in the Reynolds number equation was the diameter of the tube connection on the flow meter. The velocity in the Reynolds number equation was similarly calculated by taking the flow rate measured by the flow meter and dividing by the area of the flow meter's tube connection. The pressure drop was recorded by the Omega PX157 Series differential pressure transducer and when coupled with the inlet fluid velocity and density allowed the Euler number, which is the ratio of pressure to inertia forces, to be calculated as seen in Equation 5.4.

$$Eu = \frac{\Delta P}{\rho u^2} \quad (5.4)$$

The inlet and exit fluid temperatures were measured by the Omega T-type thermocouples located in the Swagelok T unions set inline at the inlet and exit of the solid heat exchanger. The surface area for heat transfer was defined as the square root of the total fluid volume of the 4 tree-like disks. The characteristic length of the solid heat exchanger was similarly defined as the cubed root of the total fluid volume of the 4 tree-like disks.

$$A = V^{2/3} = 37.6 \text{ cm}^2 \quad (5.5)$$

$$L_c = \sqrt[3]{V} = 6.13 \text{ cm} \quad (5.6)$$

The heat transfer coefficient could then be calculated as follows,

$$h = \frac{q}{A\Delta T} \quad (5.7)$$

The Nusselt number is the ratio of convection to conduction heat transfer and was calculated as,

$$Nu = \frac{hL_c}{k} \quad (5.8)$$

The heat rate was nondimensionalized as,

$$\Omega = \frac{q}{kT_iL_c} \quad (5.9)$$

The Prandtl number is the ratio of momentum to thermal diffusivity and was assumed to be constant.

$$Pr = \frac{c_p\mu}{k} = 6.82 \quad (5.10)$$

The Stanton number is the ratio of the heat transferred to the fluid to the heat exported by the fluid and was calculated as,

$$St = \frac{h}{\rho c_p u} = \frac{Nu}{Re \cdot Pr} \quad (5.11)$$

The Colburn factor was calculated as,

$$j = St \cdot Pr^{2/3} \quad (5.12)$$

The final performance characteristic, the friction factor, is defined as,

$$f = \frac{d}{L_c} 2\rho \frac{\Delta P}{4G^2} \quad (5.13)$$

Results and Discussion

The experimental data points presented in the following results are an average over the 5 different test runs due to the relatively low uncertainty in the measurements. The pressure drop across the heat exchanger and a single tree-like disk were found to increase with increasing inlet volumetric flow rate as can be seen in Figures 5.6 and 5.7. As the flow rate increased from 1 to 1.5, 2, 2.5, and 3 lpm there was a 114.82, 70.40, 52.63, and 41.10 % increase in pressure drop across the heat exchanger respectively. Similarly, as the flow rate increased from 1 to 1.5, 2, 2.5, and 3 lpm there was a 107.01, 69.91, 50.78, and 42.09 % increase in pressure drop across a

single tree-like disk respectively. As expected, pressure drop was not found to be a function of heat rate.

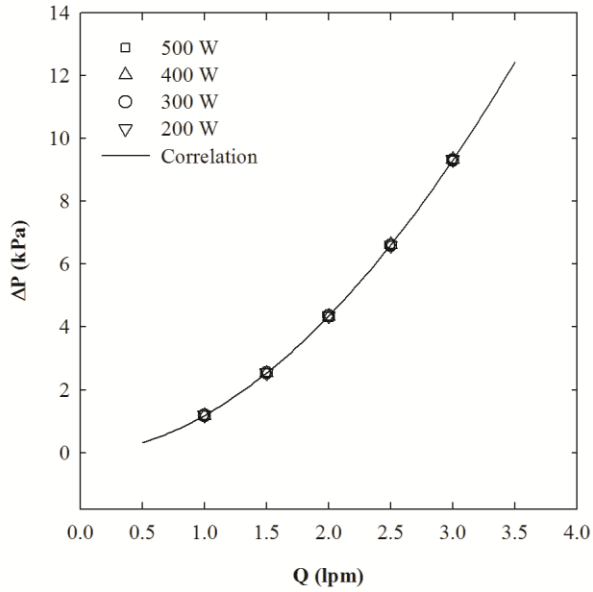


Figure 5.6. Pressure Drop across Heat Exchanger (4 tree-like disks)

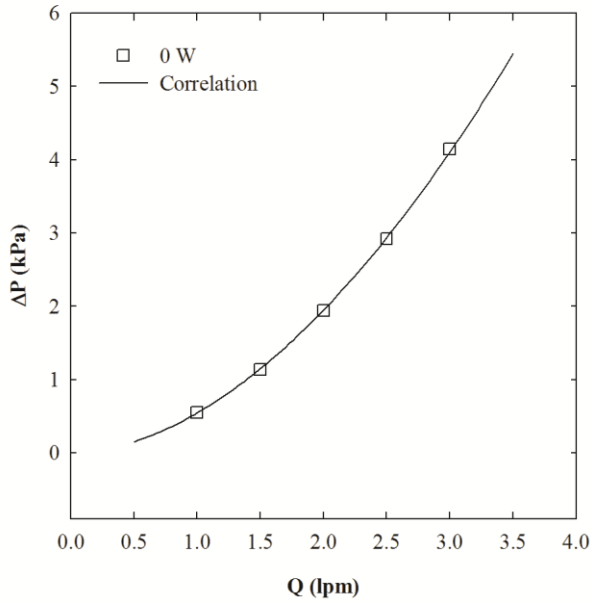


Figure 5.7. Pressure Drop across Single Tree-Like Disk

The correlation in Figure 5.6 shows the pressure drop across the heat exchanger as a function of flow rate and has the functional form of a power law. The correlation can be seen in Equation 5.14 and has a coefficient of determination, R^2 , of 1.0. Similarly, the correlation in Figure 5.7 shows the pressure drop across a single tree-like disk as a function of flow rate. The correlation can be seen in Equation 5.15 and has a R^2 value of 0.999.

$$\Delta P = 1.185Q^{1.876} \quad (5.14)$$

$$\Delta P = 0.546Q^{1.836} \quad (5.15)$$

The pressure drop and flow rate experimental data were non-dimensionalized using the Euler number and Reynolds number respectively. The non-dimensionalized results can be seen in Figures 5.8 and 5.9. As can be seen in Figures 5.8 and 5.9 pressure forces are more dominant than inertial forces at lower flow rates.

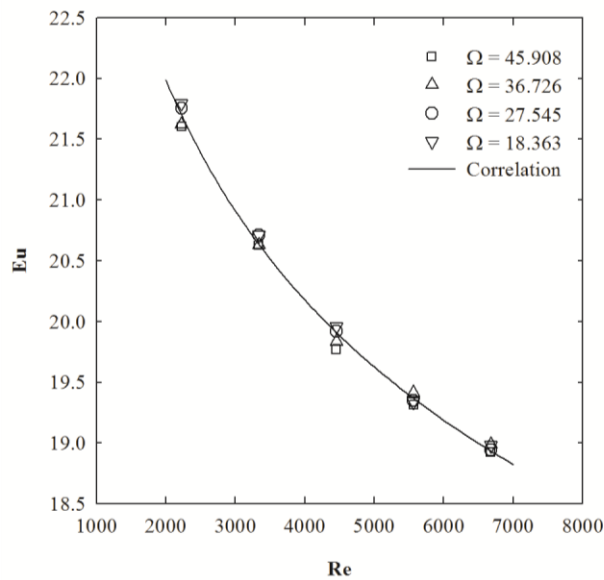


Figure 5.8. Heat Exchanger Euler Number (4 tree-like disks)

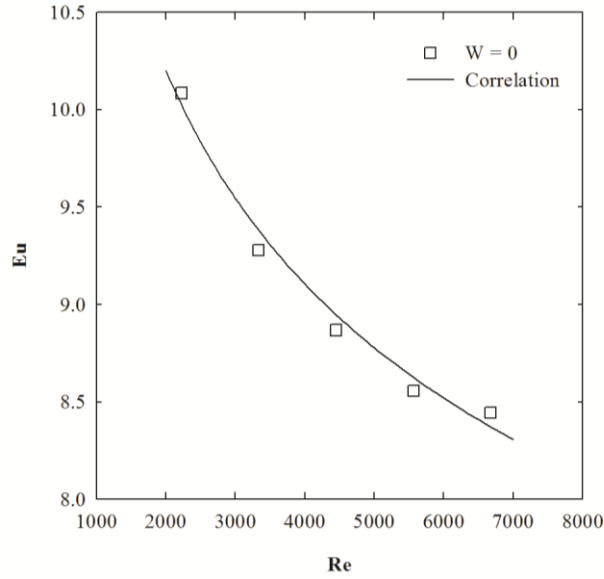


Figure 5.9. Single Tree-Like Disk Euler Number

As the Reynolds number increased from approximately 2300 to 7000 there was a 4.52, 4.15, 2.31, and 2.02 decrease in the Euler number across the heat exchanger. Similarly, as the Reynolds number increased from approximately 2300 to 7000 there was a 7.99, 4.43, 3.50, and 1.32 % decrease in the Euler number across a single tree-like disk. The correlation in Figure 5.8 shows the Euler number across the heat exchanger as a function of the Reynolds number and has the functional form of a power law. The correlation can be seen in Equation 5.16 and has a R^2 value of 0.996. Similarly, the correlation in Figure 5.9 shows the pressure drop across a single tree-like disk as a function of flow rate. The correlation can be seen in Equation 5.17 and has a R^2 value of 0.984.

$$Eu = 56.431Re^{-0.124} \quad (5.16)$$

$$Eu = 35.484Re^{-0.164} \quad (5.17)$$

The fluid temperature increase across the heat exchanger as a function of flow rate can be seen in Figure 5.10. The temperature difference across the heat exchanger was found to decrease

with increasing volumetric flow rate. The ratio of convection to conduction heat transfer was found to increase with Reynolds number as evidenced in the Nusselt number plot in Figure 5.11.

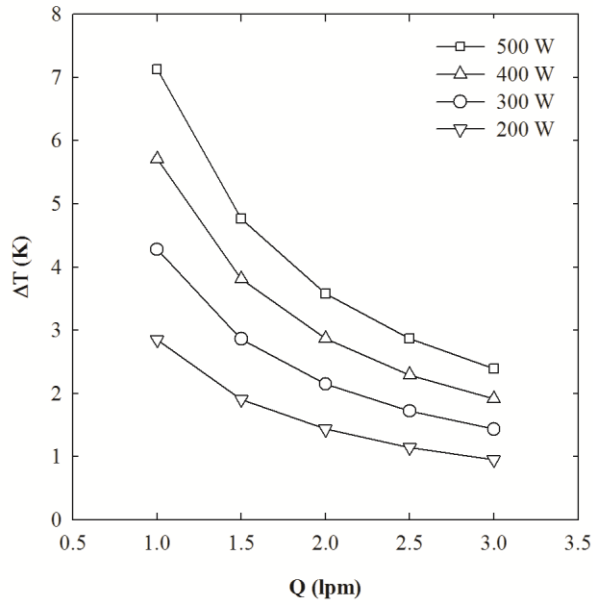


Figure 5.10. Heat Exchanger Temperature Increase (4 tree-like disks)

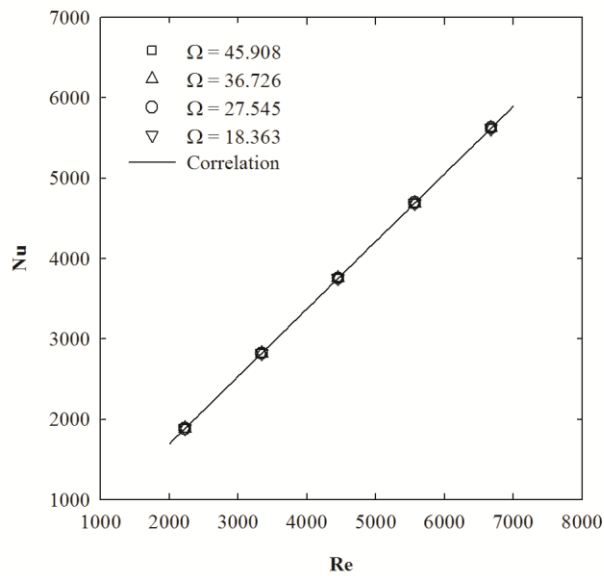


Figure 5.11. Heat Exchanger Nusselt Number (4 tree-like disks)

As the heat rate increases from 200 to 300, 400, and 500 W there is an average temperature increase across all flow rates of 1.66, 2.49, 3.32, and 4.15 K respectively. As the Reynolds number increased from approximately 2300 to 7000 there was a 49.57, 33.19, 24.83, and 19.90 % increase in the Nusselt number across the heat exchanger. The Nusselt number was found to be a linear function of the Reynolds number. The correlation in Figure 5.11 shows the Nusselt number as a function of the Reynolds number. The correlation can be seen in Equation 5.18 and has a R^2 value of 1.0

$$Nu = 0.839Re + 18.468 \quad (18)$$

In order to characterize the thermal performance of the heat exchanger the Colburn factor was utilized as recommended by Kays and London [5.31] for compact heat exchangers. As can be seen in Figure 5.12 more heat is exported by the fluid than transferred to the fluid as the Reynolds number is increased. The friction factor was found to decrease with increasing Reynolds number and can be seen in Figure 5.13.

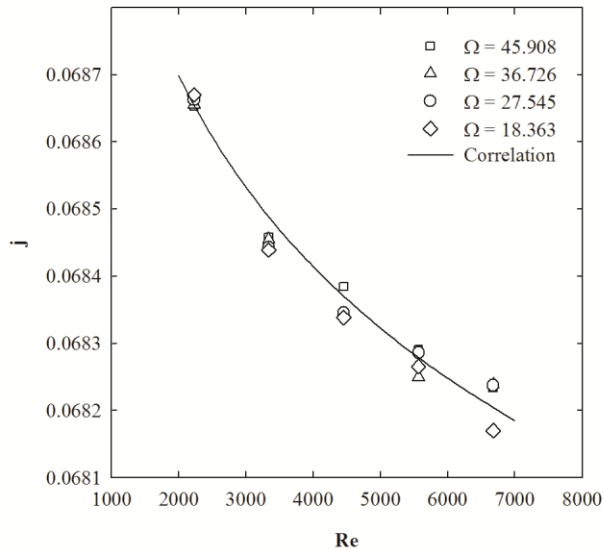


Figure 5.12. Heat Exchanger Colburn Factor (4 tree-like disks)

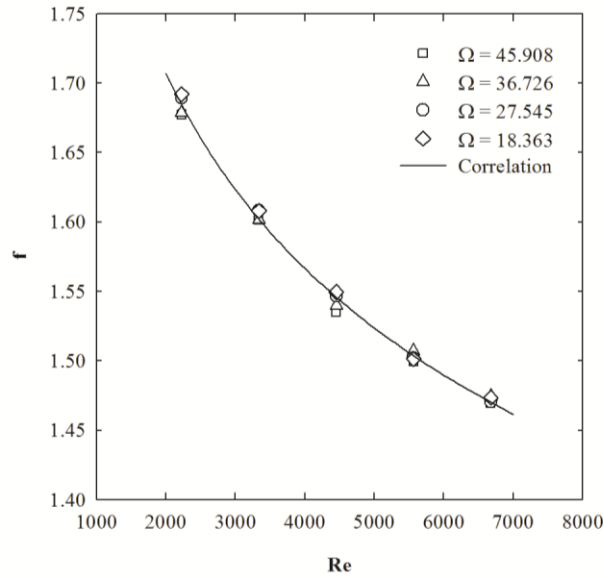


Figure 5.13. Heat Exchanger Friction Factor (4 tree-like disks)

As the Reynolds number increased from approximately 2300 to 7000 there was a 0.28, 0.11, 0.14, and 0.08 % decrease in the Colburn factor. As the Reynolds number increased from approximately 2300 to 7000 there was a 4.52, 4.15, 2.31, and 2.01% decrease in the friction factor. The correlation in Figure 5.12 shows the Colburn factor as a function of the Reynolds number. The correlation can be seen in Equation 5.19 and has a R^2 value of 0.973. The correlation in Figure 5.13 shows the friction factor as a function of the Reynolds number. The correlation can be seen in Equation 5.20 and has a R^2 value of 0.996.

$$j = 0.072Re^{-0.006} \quad (5.19)$$

$$f = 4.381Re^{-0.124} \quad (5.20)$$

Conclusions

The system performance of a biologically-inspired single fluid compact heat exchanger has been experimentally examined. Results were cast in terms of commonly defined dimensionless parameters that allow the single fluid compact heat exchanger with tree-like flow passages to be compared to traditional two fluid compact heat exchangers. The pressure drop

across the heat exchanger was found to increase with the flow rate while pressure forces dominate inertial forces at low Reynolds numbers. The temperature increase across the heat exchanger was found to decrease with increasing flow rate while convection heat transfer was found to dominate conduction heat transfer as the Reynolds number increases. As the Reynolds number decreases the ratio of the heat transferred to the fluid to the heat exported by the fluid decreases. As the Reynolds number, and thus the flow-stream mass velocity, increases the friction factor decreases. Correlations for the Euler number, Colburn factor, and friction factor as a function of the Reynolds number were developed and found to have the functional form of a power law while the Nusselt number was found to be a linear function of the Reynolds number.

Acknowledgements

Portions of this work were funded by the von Braun Center for Science and Innovation and The University of Alabama GK-12 Program. The GK-12 Program is supported by the National Science Foundation under grant 0742504. The authors would also like to thank Kenny Mahan and Hunter Corum for their assistance in the design of the experiment and in collecting data.

References

- [5.1] Murray, C. D., 1926, "The Physiological Principle of Minimum Work. I. The Vascular System and the Cost of Blood Volume", *Journal of Physiology*, 12, pp. 207-214.
- [5.2] West, G. B., Brown, J. H., and Enquist, B. J., 1997, "A General Model for the Origin of Allometric Scaling Laws in Biology", *Science*, 276, pp. 122-126.
- [5.3] West, G. B., Brown, J. H., and Enquist, B. J., 1999, "The Fourth Dimension of Life: Tree-like Geometry and Allometric Scaling of Organisms", *Science*, 284, pp. 1677-1679.
- [5.4] West, G. B., 1999, "The Origin of Universal Scaling Laws in Biology", *Physica A*, 263, pp. 104-113.
- [5.5] Bejan, A., 1997, "Constructal-Theory Network of Conducting Paths for Cooling a Heat Generating Volume", *International Journal of Heat and Mass Transfer*, 40, pp. 799-816.
- [5.6] Bejan, A., and Lorente, S., 2010, "The Constructal Law of Design and Evolution in Nature", *Philosophical Transactions of the Royal Society B*, 365, pp. 1335-1347.
- [5.7] Bejan, A., and Lorente, S., 2006, "Constructal Theory of Generation of Configuration in Nature and Engineering", *J. Applied Physics*, 100.
- [5.8] Alebrahim, A., and Bejan, A., 1999, "Constructal Trees of Circular Fins for Conductive and Convective Heat Transfer", *Intl. J. of Heat and Mass Transfer*, 42, pp. 3585-3597.
- [5.9] Bejan, A., Almogbel, M., 2000, "Constructal T-Shaped Fins", *Intl. J. of Heat and Mass Transfer*, 43, pp. 2101-2115.
- [5.10] Almogbel, M., and Bejan, A., 2000, "Cylindrical Trees of Pin Fins", *Intl. J. of Heat and Mass Transfer*, 43, pp. 4285-4297.
- [5.11] Almogbel, A., Bejan, A., 2001, "Constructal Optimization of Nonuniformly Distributed Tree-Shaped Flow Structures for Conduction", *Intl. J. of Heat and Mass Transfer*, 44, pp. 4185-4195.
- [5.12] Calamas, D., and Baker, J., 2013, "Tree-Like Branching Fins: Performance and Natural Convective Heat Transfer Behavior", *Intl. J. of Heat and Mass Transfer*, Accepted for Publication.
- [5.13] Calamas, D., and Baker, J., 2013, "Behavior of Thermally Radiating Tree-Like Fins", *J. of Heat Transfer*, Accepted for Publication.
- [5.14] Tuckerman, B. B., and Pease, R. F. W., 1981, "High-Performance Heat Sinking for VLSI", *IEEE Electron Device Letters*, 2, pp. 126-129.

- [5.15] Pence, D. V., 2002, "Reduced Pumping Power and Wall Temperature in Microchannel Heat Sinks with Tree-like-Like Branching Channel Networks", *Microscale Thermophysical Engineering*, 6, pp. 319-330.
- [5.16] Pence, D. V., 2000, "Improved Thermal Efficiency and Temperature Uniformity Using Tree-like-Like Branching Channel Networks", *Proc. Intl. Conference on Heat Transfer and Transport Phenomena in Microscale*, pp. 142-148.
- [5.17] Alharbi, A. Y., Pence, D. V., and Cullion, R. N., 2004, "Fluid Flow Through Microscale Tree-like-Like Branching Channel Networks", *J. of Fluids Engineering*, 125, pp. 1051-1057.
- [5.18] Alharbi, A. Y., Pence, D. V., and Cullion, R. N., 2004, "Thermal Characteristics of Microscale Tree-like-Like Branching Channels", *J. of Heat Transfer*, 126, pp. 744-755.
- [5.19] Wang, X. Q., Mujumdar, A. S., and Yap, C., 2006, "Thermal Characteristics of Tree-Shaped Microchannel Nets for Cooling of a Rectangular Heat Sink", *Intl. J. of Thermal Sciences*, 45, pp. 1103-1112.
- [5.20] Senn, S. M., and Poulikakos, D., 2004, "Laminar Mixing, Heat Transfer and Pressure Drop in Tree-Like Microchannel Nets and Their Application for Thermal Management in Polymer Electrolyte Fuel Cells", *J. of Power Sources*, 130, pp. 178-191.
- [5.21] Calamas, D., and Baker, J., 2013, "Performance of a Biologically-Inspired Heat Exchanger with Hierarchical Bifurcating Flow Passages", *J. of Thermophysics and Heat Transfer*, Accepted for Publication.
- [5.22] Bejan, A., 2002, "Dendritic Constructal Heat Exchanger with Small-Scale Crossflows and Larger-Scales Counterflows", *Intl. J. of Heat and Mass Transfer*, 45, pp. 4607-4620.
- [5.23] da Silva, A. K., and Bejan, A., 2006, "Dendritic Counterflow Heat Exchanger Experiments", *Intl. J. of Thermal Sciences*, 45, pp. 860-869.
- [5.24] Zimparov, V. D., da Silva, A. K., and Bejan, A., 2006, "Constructal Tree-Shaped Parallel Flow Heat Exchangers", *Intl. J. of Heat and Mass Transfer*, 49, pp. 4558-4566.
- [5.25] Azad, A. V., and Amidpour, M., 2011, "Economic Optimization of Shell and Tube Heat Exchanger Based on Constructal Theory", *Energy*, 26, pp. 1087-1096.
- [5.26] Raja, V. A. P., Basak, T., and Das, S. K., 2008, "Thermal Performance of a Multi-Block Heat Exchanger Designed on the Basis of Bejan's Constructal Theory", *Intl. J. of Heat and Mass Transfer*, 51, pp. 3582-3594.

- [5.27] Zhang, H., Lorente, S., and Bejan, A., 2009, "Vascularization with Line-to-Line Trees in Counterflow Heat Exchange", *Intl. J. of Heat and Mass Transfer*, 52, pp. 4372-4342.
- [5.28] Zamfirescu, C., and Bejan, A., 2003, "Constructal Tree-Shaped Two-Phase Flow for Cooling a Surface", *Intl. J. of Heat Transfer*, 46, pp. 2785-2797.
- [5.29] Bonjour, J., Rocha, L. A. O., Bejan, A., and Meunier, F., 2004, "Dendritic Fins Optimization for a Coaxial Two-Stream Heat Exchanger", *Intl. J. of Heat and Mass Transfer*, 47, pp. 111-124.
- [5.30] Wheeler, A. J., and Ganji, A. R., 2004, *Introduction to Engineering Experimentation*, 2nd ed., Pearson Prentice Hall, Upper Saddle River, NJ.
- [5.31] Kays, W. M., and London, A. L., 1984, *Compact Heat Exchangers*, 2nd ed., McGraw-Hill, New York.

CHAPTER 6

FLOW BEHAVIOR AND PRESSURE DROP IN POROUS DISKS WITH BIFURCATING FLOW PASSAGES*

Abstract

The performance of a porous disk with hierarchical bifurcating flow passages has been examined. The hierarchical bifurcating flow passages in the heat exchanger mimic those seen in the vascular systems of plants and animals. The effect of bifurcation angle, porosity, and pore size on the pressure drop across a porous disk was examined computationally. The pressure drop across the porous disk was found to increase as the pore size decreased. As the bifurcation angle increased the pressure drop also increased. At high porosities the bifurcation angles did not have an impact on the pressure drop across the porous disk due to flow behavior. Similarly, the effect of bifurcation angle on pressure drop decreased as the pore size increased.

Introduction

Flow systems have a natural propensity to advance toward greater flow access. This phenomenon can easily be seen in rivers and in the veins of tree leaves. Similarly, the human circulatory system features bifurcating flow passages similar to the fluid transport systems found in nature. The human lungs have a surface area to volume ratio an order of magnitude larger when compared with traditional compact heat exchangers. Systems with biologically inspired flow passages produce space-filling flow networks, minimize flow resistance, and enhance surface area to volume ratios. These biologically-inspired, or tree-like, flow networks have

* Note. This chapter is based on Calamas, D., Baker, J., and Sharif, M., 2013, "Flow Behavior and Pressure Drop in Porous Disks with Bifurcating Flow Passages," Journal of Fluids Engineering (Submitted for Publication).

several advantages when compared to traditional parallel-flow networks. These advantages include lower pressure drop, increased surface temperature uniformity and increased surface area per volume for heat transfer. Looking again to nature, mangrove trees have been found to offer excellent carbon capturing, salt filtration and even close the pores on their leaves to reduce sun exposure as well as absorb heat to prevent evaporation of the shallow water that makes up their habitat. Porous materials can thus also be utilized to increase surface area per volume while simultaneously reducing system mass.

Tuckerman and Pease [6.1] first proposed the use of microchannel heat sinks with large surface area to volume ratios for the thermal management of planar circuits. Tuckerman and Pease concluded that microscale channels were advantageous for laminar flow due to the heat transfer coefficient scaling inversely with channel width. West et al. [6.2-6.4] established scaling laws for fluid transport through space-filling, tree-like, flow networks based on three assumptions: a tree-like branching network is necessary to supply an entire systems' volume, the final branch level is size invariant, and finally the energy needed to supply the flow network should be minimized. Bejan [6.2] first proposed universal geometries that could theoretically unite transport systems found in engineering and nature and recommended their application to the design of engineered systems. Bejan [6.6] established a solution for optimizing conducting paths for application in cooling a heat generating volume and concluded the paths form a tree-like network. Bejan's "Constructal Theory," explains the natural affinity of flow systems to progress toward greater flow access [6.7, 6.8]. Bejan and Errera [6.9] considered convection heat transfer and concluded the fluid channels similarly formed a volume filling tree-like flow network. Calamas and Baker [6.10] investigated the thermal performance of tree-like fins in a naturally convecting environment and found the tree-like fins were more effective when

compared with rectangular fins of equal mass, volume, and base area. Similarly, Calamas and Baker [6.11] investigated the performance of tree-like fins thermally radiating to free space and concluded the tree-like fins were more effective than rectangular fins of equal mass, volume, and base area. Murray [6.12] considered the principle of minimum work in the human circulatory system and concluded there is an optimal change in hydraulic diameter at bifurcations that minimizes flow resistance. Murray found parent and daughter branches can thus be connected in a way that theoretically provides maximum bulk fluid transport for the lowest amount of required pumping power.

Pence [6.13] compared a heat sink with a fractal-like flow network to a heat sink with a parallel flow network of equal surface area, pumping power, and flow rate and found the fractal-like network resulted in lower pressure drop as well as reduced maximum wall temperatures. Pence [6.14] compared a square shaped parallel channel heat sink to a disk shaped branching channel heat sink of equal surface area and found the fractal-like flow network resulted in increased thermal efficiency. Alharbi et al. [6.15] concluded the one-dimensional model developed by Pence [6.13] should include temperature dependent fluid properties. Alharbi et al. [6.15] found assuming constant fluid properties resulted in an overestimation of pressure drop. Alharbi et al. also observed local pressure recovery at bifurcations were a result of an increase in flow area and subsequent flow deceleration. Alharbi et al. [6.16] concluded fractal-like flow network resulted in increased surface temperature uniformity when compared with parallel channel flow networks for the same maximum wall temperature. Calamas and Baker [6.17] examined the effect of scaling on the microscale fractal-like flow network employed by Alharbi et al. [6.16] and concluded microscale and mesoscale flow networks offer similar thermal performance while mesoscale flow networks have the additional advantage of reduced pressure

drop. Wang et al. [6.18] similarly concluded tree-like microchannel flow networks resulted in improved temperature uniformity when compared with parallel channel flow networks. Wang et al. [6.18, 6.19] observed tree-like flow networks reduced the effect of channel blockage when compared with parallel channel flow networks. Wang et al. [6.19] also found increasing the number of parent channels emanating from the inlet plenum at the center of a disk shaped heat sink and increasing the number of branch levels resulted in increased surface temperature uniformity. Chen and Cheng [6.20] found increasing the number of branch levels resulted in a higher heat transfer capability and lower total pressure drop. Chen and Cheng [6.21] experimentally concluded that heat sinks with fractal-like flow networks were more thermally efficient than heat sinks with parallel channel flow networks by holding the heat transfer rate, temperature difference, and inlet velocity constant. Senn and Poulikakos [6.22] found a tree-like branching flow network with six branch levels had almost half the total pressure drop when compared with a parallel channel flow network of equal surface area and inlet Reynolds number. Senn and Poulikakos observed transverse vortices created recirculation at bifurcations that resulted in hot spots at the inner corners of bifurcations Senn and Poulikakos also observed longitudinal vortices after bifurcations resulted in enhanced thermal mixing and thus reduced the required flow rate for heat transfer. Wang et al. [6.23] similarly concluded that the total pressure drop increased and surface temperature uniformity decreased as the bifurcation angle increased due to flow recirculation after bifurcations.

The use of porous media to enhance heat transfer in heat exchangers has also been studied in the past. Allouache and Chikh [6.24] investigated the effect of porous layer thickness, permeability, and effective thermal conductivity on the performance of an annular heat exchanger. Allouache and Chikh recommended criteria for porous media to minimize pressure

drop and enhance heat transfer. Al-Salem et al. [6.25] experimentally investigated the effects of porosity and thickness of porous sheets over a heated cylinder in cross flow. The addition of the porous layers enhanced heat transfer and was not found to increase the pressure drop across the system. Lan and Khodadadi [6.26] performed a theoretical study of fluid flow and heat transfer through a porous media filled channel with permeable walls and presented Nusselt and Peclet numbers as a function of inlet Reynolds number. Mohamad [6.27] investigated the heat transfer enhancement due to porous media in a pipe and found partially filling the pipe enhanced the rate of heat transfer and resulted in less pressure drop when compared with a pipe completely filled with porous media. Narasimhan and Raju [6.28] numerically studied porous medium inter-connectors in a compact heat exchanger and concluded the tube-to-tube inter-connectors enhanced the heat transfer from the tubes to the working fluid. Odabae and Hooman [6.29] performed a numerical study on a heat exchanger composed of aluminum tubes wrapped by porous metal foam in crossflow. The porous metal foam resulted in an increase in the area goodness factor when compared with a traditional finned-tube heat exchanger. Pavel and Mohamad [6.30] utilized porous inserts in a heat transfer pipe and found the inserts resulted in a higher heat transfer rate but also increased the pressure drop. Targui and Kahalerras [6.31] performed a numerical study on flow and heat transfer characteristics in a double pipe heat exchanger with porous inserts. Targui and Kahalerras found staggering the inserts in both cylinders yielded the highest heat transfer rates. Yang and Hwang [6.32] investigated turbulent heat transfer enhancement in a heat exchanger pipe filled with porous media and found the porous media improved the heat transfer performance of fluid channels but also increased the pressure drop. Yang and Hwang, like Mohamad [6.27], recommended partially filling conduits with porous media to mitigate the increase in pressure drop. Zhao and Song [6.33] found that for

forced convection in porous media heated by a permeable wall the Nusselt number equals the Peclet number. The purpose of this paper is to assess the effect of porosity, pore size, and bifurcation angle on the fluid behavior and pressure drop for flow networks with hierarchical bifurcating flow passages in porous materials.

Utilizing biologically-inspired solutions for engineering applications is known as biomimetics. In biological systems, tree-like flow passages produce space-filling flow networks, minimize flow resistance, and enhance surface area to volume ratios. Biologically-inspired flow passages could thus yield improved system performance when utilized in compact heat exchangers. Tree-like flow networks have many advantages when compared to traditional parallel flow networks. Tree-like flow networks have greater surface area for heat transfer per unit volume when compared with traditional parallel flow compact heat exchangers. Additional advantages of tree-like flow networks when compared to parallel flow networks consist of lower total pressure drop as well as lower, more uniform, maximum wall temperatures.

Method of Analysis

The nomenclature and coordinate system used to describe the tree-like flow networks utilized in the present analysis can be seen in Figure 6.1. The first branch emanating from the inlet plenum is defined as the zeroth-order branch, where $k = 0$, and the last branch is defined as the fourth-order branch, where $k = 4$. Following West et al. [6.2] and Pence [6.14] the following branch scale ratios were utilized,

$$\beta = \frac{d_{k+1}}{d_k} = n^{-1/3} \quad (6.1)$$

$$\gamma = \frac{L_{k+1}}{L_k} = n^{-1/2} \quad (6.2)$$

For this analysis, $n = 2$ as each parent channel splits into 2 daughter channels. The dimensions of the tree-like flow networks located in the porous disks employed in the present analysis are provided in Table 6.1.

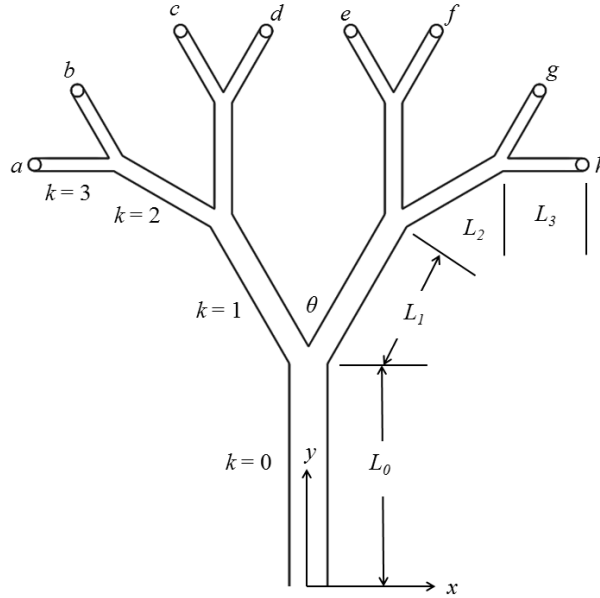


Figure 6.1. Nomenclature and Coordinate System for Branching Flow Networks

Table 6.1. Disk Geometry

k	H_k (cm)	w_k (cm)	d_k (cm)	L_k (cm)
0	0.3	0.300	0.300	1.750
1	0.3	0.197	0.238	1.237
2	0.3	0.138	0.189	0.875
3	0.3	0.100	0.150	0.619

The porous tree-like disks have a radius of 10 cm and a thickness of 0.8 cm. The geometry of the flow networks utilized in the present analysis was designed so that the third order branch levels, $k = 3$, would be on the verge of microscale. Six different bifurcation angles will be utilized in order to assess the effect of bifurcation angle on the pressure drop and flow behavior of the porous tree-like disks. The six different porous tree-like disks can be seen in Figure 6.2. Each

porous disk has 4 tree-like flow networks stemming from the inlet plenum. While the porous tree-like disks with 15, 30, 45, and 60 ° bifurcation angles are not space filling the number of tree-like flow networks stemming from the inlet plenum was held constant to assess the effect of bifurcation angle on the pressure drop across the porous disks.

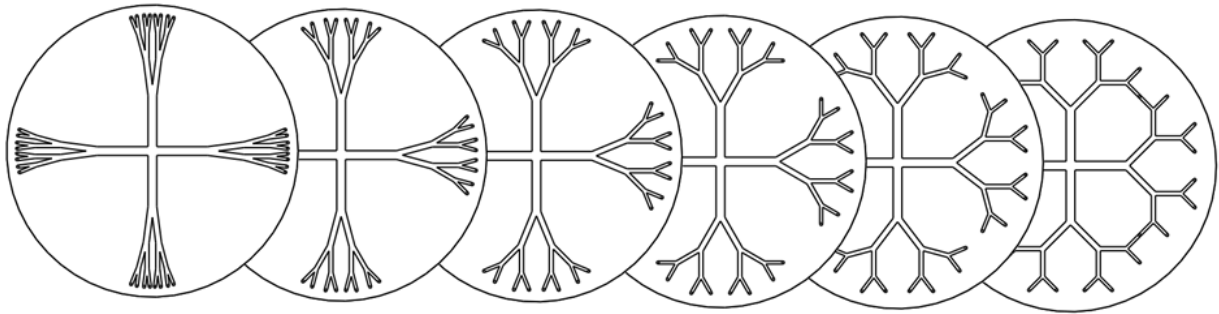


Figure 6.2. 15, 30, 45, 60, 75, and 90 ° Porous Disks.

Six different bifurcation angles will be utilized in the present analysis, 15, 30, 45, 60, 75, and 90 °. The disks will be composed of a porous material with three different pore sizes, or pores per inch (PPI), as well as five different porosities, or relative densities. The pore sizes utilized are 10, 20, and 40 PPI and the porosities are 0.3, 0.25, 0.5, 0.75, and 0.97.

The fluid enters the tree-like flow network through an inlet plenum perpendicular to the flow network at the entrance of the $k = 0$ branch level and travels radially outward. The fluid passes through the disk at the exit of the $k = 3$ branch level and travels radially inward on the other side of the porous disk where it exits the flow network through an exit plenum perpendicular to the flow network. At the inlet of the $k = 0$ branch the fluid temperature is fixed at 293 K and a uniform velocity profile is assumed. The velocity profile was assumed to be uniform as in Alharbi et al. [6.13]. Five different volumetric flow rates, 1.0, 1.5, 2.0, 2.5, and 3.0 lpm will be utilized. The fluid exits the $k = 0$ branch level at environmental pressure. The pressure drop across the tree-like flow network is defined as the static pressure difference

between the fluid inlet at the entrance of the $k = 0$ branch and the fluid discharge at the exit plenum. An exploded view of the computational model can be seen in Figure 6.3. The computational model assembly is composed of the porous disk with embedded tree-like flow networks, an enclosure, and two end caps where the inlet and exit plenums are located. The inlet and exit plenums have a diameter of 0.42 cm.

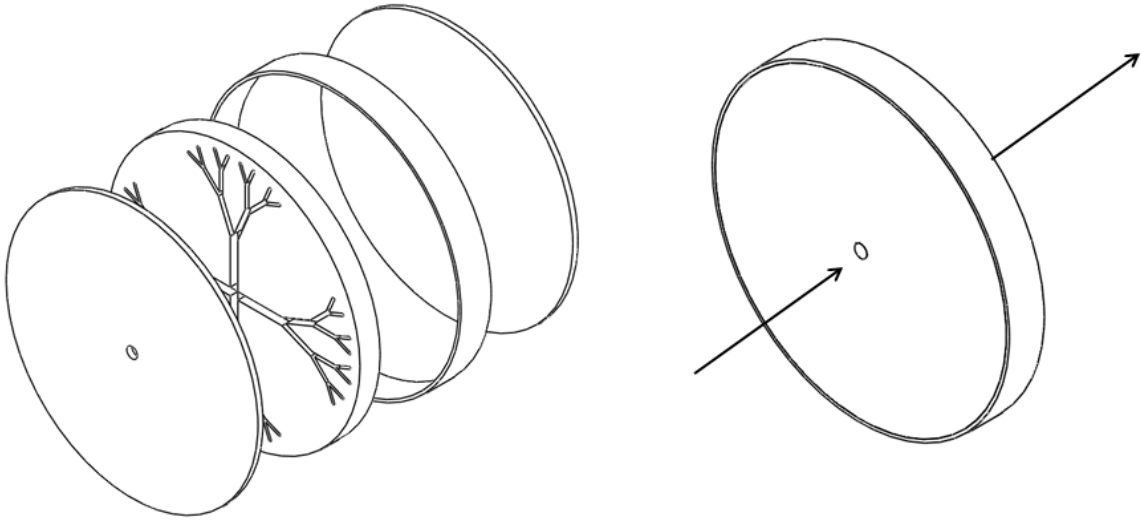


Figure 6.3. Computational Model Exploded View and Assembly

Computational Methods

The computational fluid dynamic simulations were performed using commercially available computational fluid dynamics software, employing the finite volume method. The three-dimensional continuity and Navier-Stokes equations evaluated at steady-state are as follows:

$$\frac{\partial}{\partial x_i} (\rho u_i) = 0 \quad (6.3)$$

$$\frac{\partial}{\partial x_j} (\rho u_i u_j) + \frac{\partial P}{\partial x_i} = \frac{\partial}{\partial x_j} (\tau_{ij} + \tau_{ij}^R) + S_i \quad (6.4)$$

The working fluid, water, was assumed to be incompressible and the problem was evaluated at steady-state. The viscous shear stress tensor and the Reynolds stress tensor are defined as:

$$\tau_{ij} = \mu \left(\frac{\partial u_i}{\partial x_j} + \frac{\partial u_j}{\partial x_i} - \frac{2}{3} \delta_{ij} \frac{\partial u_k}{\partial x_k} \right) \quad (6.5)$$

$$\tau_{ij}^R = \mu_T \left(\frac{\partial u_i}{\partial x_j} + \frac{\partial u_j}{\partial x_i} - \frac{2}{3} \delta_{ij} \frac{\partial u_k}{\partial x_k} \right) - \frac{2}{3} \rho k \delta_{ij} \quad (6.6)$$

The Navier-Stokes equations are accompanied by fluid state equations which define the nature of the fluid as well as by empirical temperature dependencies of fluid properties [6.34]. Buoyancy effects in the momentum equation were assumed to be negligible by confirming that the Grashoff number divided by the Reynolds number squared was much less than 1. To predict turbulent flows, the Favre-averaged Navier-Stokes equations are utilized. Through this procedure, Reynolds stresses appear in the governing equations. To close the system of equations the transport equations for the turbulent kinetic energy and its dissipation rate, or the k - ε model, were utilized [6.35]. The turbulent eddy viscosity coefficient is defined as:

$$\mu_t = \frac{c_\mu \rho k^2}{\varepsilon} \quad (6.7)$$

To take into account laminar-turbulent transition the turbulent viscosity factor is defined by the expression:

$$f_\mu = [1 - e^{-0.025R_y}]^2 \cdot \left(1 + \frac{20,5}{R_T} \right) \quad (6.8)$$

where

$$R_T = \frac{\rho k^2}{\mu \varepsilon} \quad (6.9)$$

$$R_y = \frac{\rho\sqrt{k}y}{\mu} \quad (6.10)$$

The two additional transport equations used to describe the turbulent kinetic energy and dissipation are:

$$\frac{\partial \rho k}{\partial t} + \frac{\partial}{\partial x_i} (\rho u_i k) = \frac{\partial}{\partial x_i} \left(\left(\mu + \frac{\mu_t}{\sigma_k} \right) \frac{\partial k}{\partial x_i} \right) + S_k \quad (6.11)$$

$$\frac{\partial \rho k}{\partial t} + \frac{\partial}{\partial x_i} (\rho u_i k) = \frac{\partial}{\partial x_i} \left(\left(\mu + \frac{\mu_t}{\sigma_k} \right) \frac{\partial k}{\partial x_i} \right) + S_\varepsilon \quad (6.12)$$

where

$$S_k = \tau_{ij}^R \frac{\partial u_i}{\partial x_j} - \rho \varepsilon + \mu_t P_B \quad (6.13)$$

$$S_\varepsilon = C_{\varepsilon 1} \frac{\varepsilon}{k} \left(f_1 \tau_{ij}^R \frac{\partial u_i}{\partial x_j} - C_{\varepsilon 2} f_2 \frac{\rho \varepsilon^2}{k} \right) \quad (6.14)$$

$$f_1 = 1 + \left(\frac{0.05}{f_\mu} \right)^3 \quad (6.15)$$

$$f_2 = 1 - e^{-R_T^2} \quad (6.16)$$

The constants, defined empirically are: $C_\mu = 0.09$, $C_{\varepsilon 1} = 1.44$, $C_{\varepsilon 2} = 1.92$, $\sigma_\varepsilon = 1.3$, and $\sigma_k = 1$. A laminar/turbulent boundary layer model is used to describe flows in near-wall regions. The model is based on the Modified Wall Functions approach. This model is employed to characterize laminar and turbulent flows near the walls, and to describe transitions from laminar to turbulent flow or turbulent to laminar flow. The modified wall function uses a Van Driest's profile as opposed to a logarithmic profile [6.36]. If the size of the mesh cell near the wall is more than the boundary layer thickness the integral boundary layer technology is used.

The mass-distributed external force per unit mass due to a porous media's resistance is defined as:

$$S_i = -k\delta_{ij}\rho u_j \quad (6.17)$$

Density of the solid material is calculated based on the imputed porosity. The porous materials permeability was assumed to be independent of direction, or isotropic. Pressure drop through the porous material was assumed to be strictly a function of pore size, or pores per inch (PPI). The porous medium's resistance to fluid flow is thus defined as:

$$k = \frac{\mu}{\rho} D^2 \quad (6.18)$$

The governing equations are solved with the finite volume method on a spatially rectangular computational mesh with the planes orthogonal to the Cartesian coordinate system axes and refined locally at the solid/fluid interface and in the fluid region. At the solid/fluid interface additional boundary faces and corresponding mass and heat fluxes that take into account boundary conditions and model geometry are introduced. The governing equations are discretized in a conservative form. The numerical model is spatially second-order accurate. The governing equations are integrated over a control volume and then approximated with cell-centered values of the basic variables [6.37-6.39]. Second-order upwind approximations of fluxes are based on the implicitly treated modified Leonard's QUICK (Quadratic Upstream Interpolation for Convective Kinematics) [6.40] approximations and the TVD (Total Variation Diminishing) [6.41] method. An elliptic type discrete pressure equation is derived by algebraic transformations of the derived discrete governing equations and incorporates velocity boundary conditions using the SIMPLE (Semi-Implicit Method for Pressure Linked Equations) [6.42] method.

Validation and Verification

Two validations will be performed. The first will validate the geometry while the second will validate the porous model. Calamas and Baker [6.43] experimentally examined flow through a solid aluminum disk with hierarchical bifurcating flow passages. The working fluid was assumed to be water and the inlet velocity profile was assumed to be uniform. The fluid was assumed to exit at environmental pressure. The number of cells in the three-dimensional computational model of the aluminum disk with hierarchical bifurcating flow passages was successfully doubled until grid independence was achieved. The grid was refined seven times. The verified computational mesh consisted of approximately 3,000,000 cells, corresponding to the fifth level of grid refinement, proved to be sufficient for the analysis. The error between the computational model and the experimental data was found to be less than 10.4 % at all flow rates utilized in the analysis. The experimental data and subsequently validated and verified computational data can be seen in Figure 6.4.

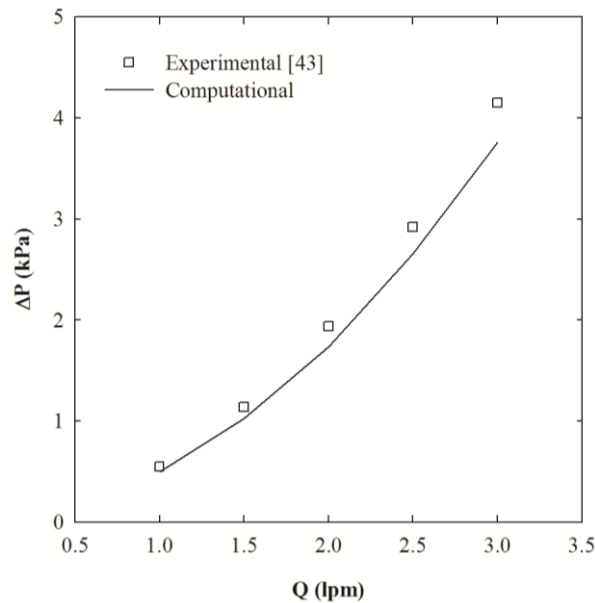


Figure 6.4. Computational Model Geometry Validation

Dukhan and Patal [6.44] experimentally examined pressure drop across several porous foams with varying porosities and pore sizes in an open-loop wind tunnel. A uniform inlet velocity profile was assumed for the working fluid, air as the authors utilized methods to reduce entrance effects and straighten the flow. The porous material was assumed to have an isotropic permeability and the resistance to flow through the porous material was assumed to be dependent on the reference pore size alone. Two different pore sizes corresponding to 10 and 20 PPI as well as two different porosities were utilized in the computational model validation. The number of cells in the three-dimensional computational model of the rectangular porous foam block was successfully doubled until grid independence was achieved. The verified computational mesh consisted of approximately 200,000 cells, corresponding to the third level of grid refinement, proved to be sufficient for the analysis. The average error between the computational model and the experimental data was found to be less than 6.2 %. The experimental data and subsequently validated and verified computational data can be seen in Figure 6.5.

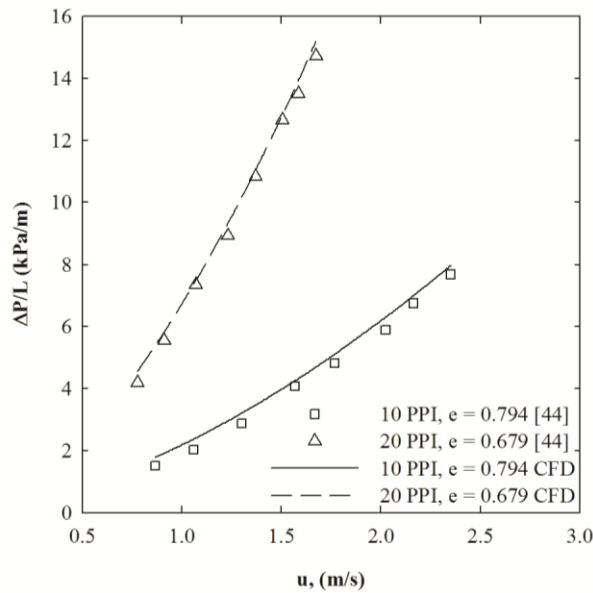


Figure 6.5. Computational Model Porous Material Validation

Results and Discussions

As previously mentioned, six different bifurcation angles, 15, 30, 45, 60, 75, and 90 °, three different pore sizes, 10, 20, and 40 PPI, and five different porosities, 0.3, 0.25, 0.5, 0.75, and 0.97 will be utilized in the computational analysis. The effect of bifurcation angle on pressure drop was found to decrease as the number of pores per inch decreased. The average pressure drop across the 90 ° tree-like porous disk is 20.78, 12.29, and 2.83 % higher than across the 15 ° tree-like porous disk with 40, 20, and 10 PPI respectively. Due to the definition of the bifurcation angles (as can be seen in Figure 6.1) the surface area of the porous disks increases as the bifurcation angle increases. The increase in surface area contributes to the increase in pressure drop. The graphs of pressure drop as a function of flow rate, bifurcation angle, and pore size have almost completely collapsed at 10 PPI as can be seen in Figure 6.6. As the number of pores per inch decreases the pore size increases. The increase in pore size results in the bifurcation angles having almost no impact on the pressure drop as the fluid is flowing through the disk as opposed to through the tree-like channels. The pressure drop was found to increase as the bifurcation angle increased for relatively lower porosities as the fluid flows through the channels as opposed to immediately through the porous disk. The pressure drop across the porous tree-like disks was found to increase as the number of pores per inch increased due to increased flow resistance.

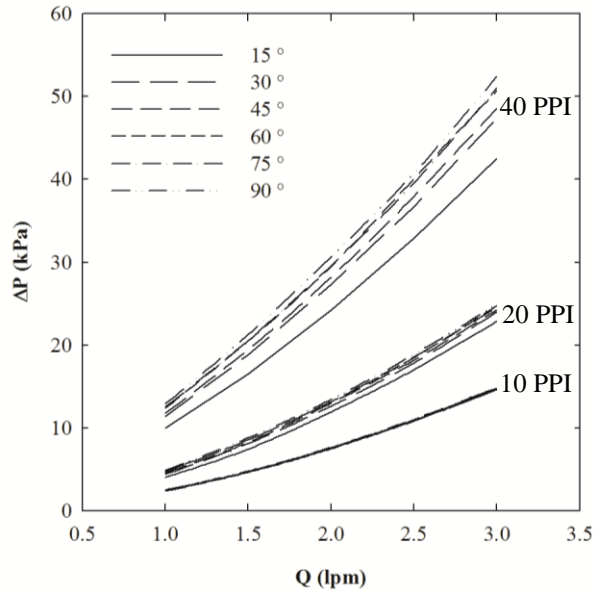


Figure 6.6. Pressure Drop as a Function of Bifurcation Angle and Pore size ($\varepsilon = 0.03$)

Pressure drop as a function of flow rate, bifurcation angle, and pore size for the 25 % porous tree-like disks can be seen in Figure 6.7. Unlike at a porosity of 3 %, as the number of pores per inch is decreased from 40 to 20 the lines corresponding to pressure drop as a function of flow rate and bifurcation angle have already collapsed. The effect of bifurcation angle on pressure drop across the tree-like porous disks thus decreases as the porosity increases due to the fluid passing through the disk. At a porosity of 25 % the 90 ° tree-like disk with 40 PPI has an average pressure drop 6.71 % higher when compared with the 15 ° tree-like disk with 40 PPI. As the number of pores per inch is reduced from 40 to 20 the 90 ° tree-like disk has an average pressure drop only 1.15 % higher than the 15 ° porous tree-like disk.

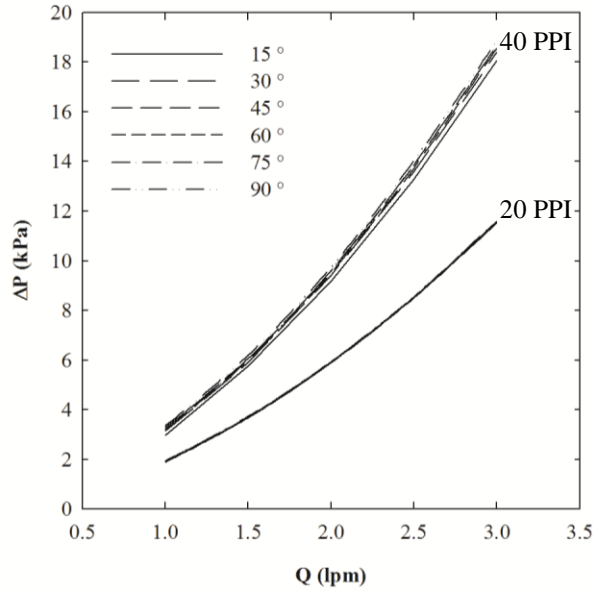


Figure 6.7. Pressure Drop as a Function of Bifurcation Angle, and Pore Size ($\epsilon = 0.25$)

Pressure drop as a function of flow rate and bifurcation angle for the 50 % porous tree-like disks can be seen in Figure 6.8 with 40 PPI.

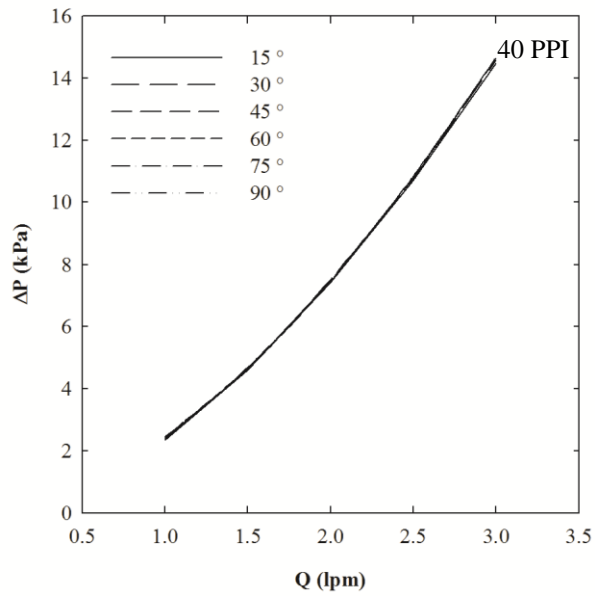


Figure 6.8. Pressure Drop as a Function of Flow Rate and Bifurcation Angle ($\epsilon = 0.5$, 40 PPI)

Unlike at a porosity of 25 %, with 40 PPI the pressure drop as a function of flow rate and bifurcation angle graph lines in Figure 6.7 have already collapsed. At a porosity of 50 % the 90 ° tree-like disk with 40 PPI has an average pressure drop 1.96 % higher when compared with the 15 ° tree-like disk with 40 PPI.

Pressure drop as a function of flow rate and pore size for the 3 and 25 % porous 45 ° tree-like disks can be seen in Figure 6.9. Other bifurcation angles are not presented as the results are not qualitatively distinguishable from the 45 ° tree-like disk. The average pressure drop across the 3 % porous 45 ° tree-like disk with 40 PPI is 286.71 % higher when compared with the same tree-like disk with 10 PPI. The average pressure drop across the 25 % porous 45 ° tree-like disk with 40 PPI is 140.04 % higher when compared with the same porous tree-like disk with 10 PPI.

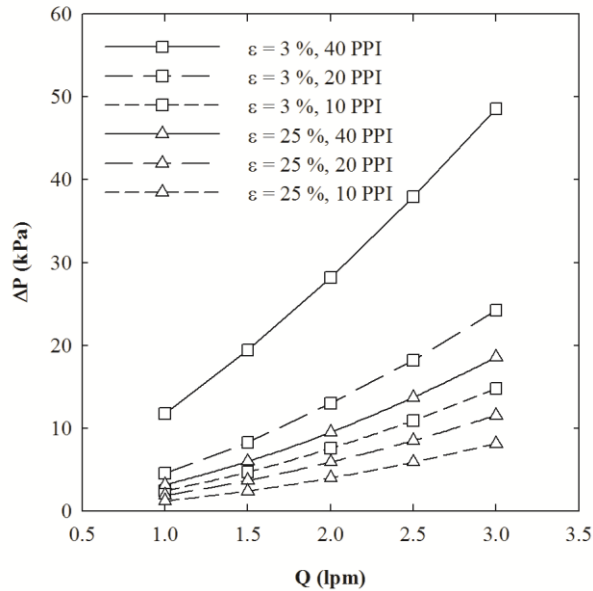


Figure 6.9. Pressure Drop as a Function of Flow Rate and Pore Size ($\epsilon = 0.03, 0.25, \theta = 45^\circ$)

Pressure drop as a function of flow rate and pore size for the 50 and 75 % porous 45 ° tree-like disks can be seen in Figure 6.10. The average pressure drop across the 50 % porous 45 ° tree-like disk with 40 PPI is 122.24 % higher when compared with the same tree-like disk with 10 PPI.

The average pressure drop across the 75 % porous 45 ° tree-like disk with 40 PPI is 118.96 % higher when compared with the same tree-like disk with 10 PPI. Pressure drop as a function of flow rate and pore size for the 97 % porous 45 ° tree-like disk can be seen in Figure 6.11. As with the 50 % porous tree-like disks, the pressure drop across the 75 and 97 % porous tree-like disks is already qualitatively indistinguishable at 40 PPI regardless of bifurcation angle. The average pressure drop across the 97 % porous 45 ° tree-like disk with 40 PPI is 119.49 % higher when compared with the same tree-like disk with 10 PPI. The bifurcation angles did not impact the pressure drop across the 75 and 97 % porous tree-like disks due to their relatively high porosities. At porosities of 50 and 75 % the flow would only travel through the $k = 0$ branch level before it passed through the disk regardless of bifurcation angle. The geometry of the flow networks are only distinguishable after the first bifurcation, or the start of the first order, $k = 1$, branch level where the bifurcation angles first change.

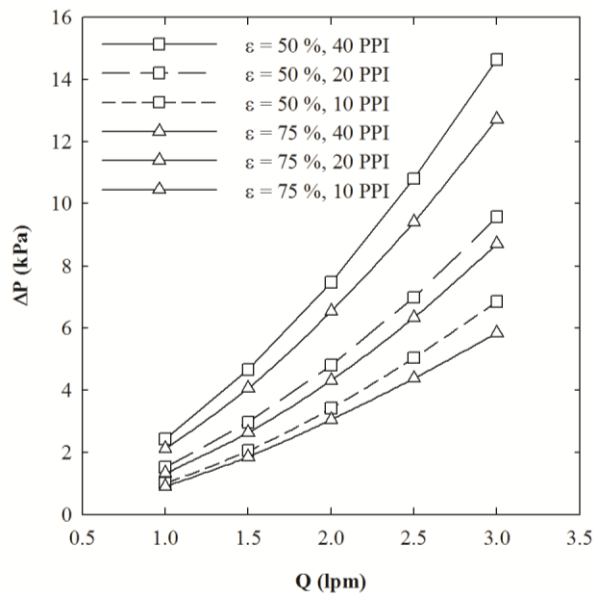


Figure 6.10. Pressure Drop as a Function of Flow Rate and Pore Size ($\varepsilon = 0.5, 75 \theta = 45^\circ$)

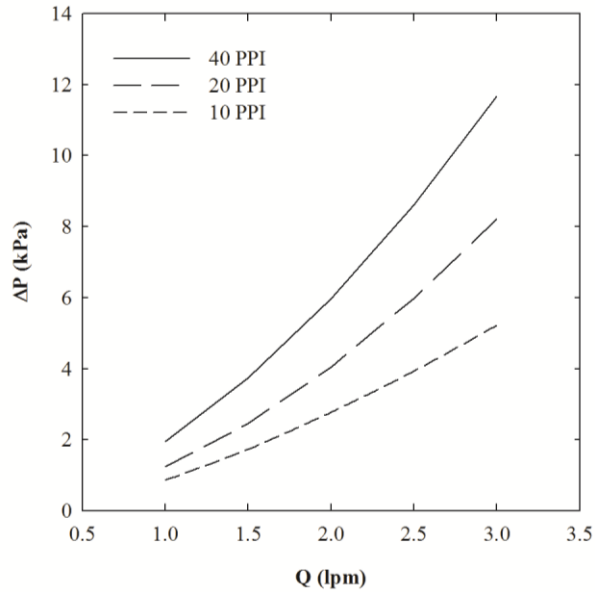


Figure 6.11. Pressure Drop as a Function of Flow Rate and Pore Size ($\varepsilon = 0.97$, $\theta = 45^\circ$)

Pressure drop as a function of flow rate and porosity for the 45° tree-like disk with 40, 20, and 10 PPI can be seen in Figures 6.12-6.14 respectively. As previously mentioned, the remaining five bifurcation angles will not be presented as their results are not qualitatively distinguishable from the 45° tree-like fin. As can be seen in Figures 6.12-6.14 the pressure drop across the porous tree-like disks increases as the porosity decreases. For example, the 3% porous 45° tree-like disk with 40 PPI has an average pressure drop 390.08% higher when compared with the 97% porous tree-like disk. As can be seen in Figures 6.12-6.14 as the number of pores per inch decreases the pressure drop across the porous tree-like disks also decreases. For example, the 50% porous 45° tree-like disk with 40 PPI has an average pressure drop 122.24% higher than the same porous tree-like disk with 10 PPI.

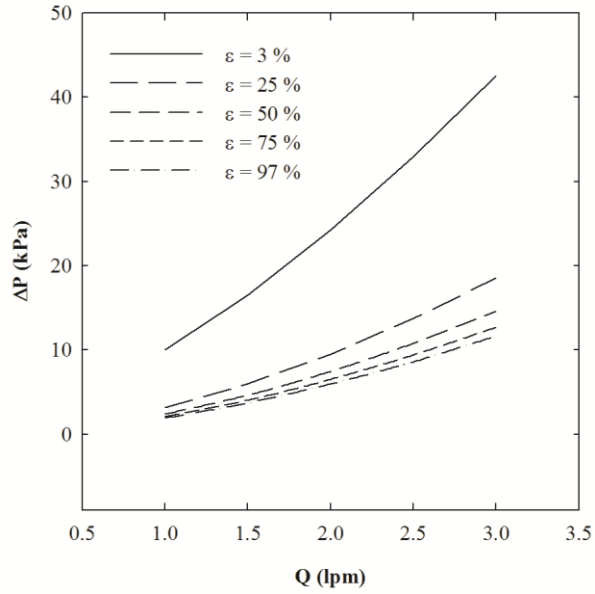


Figure 6.12. Pressure Drop as a Function of Flow Rate and Porosity ($\theta = 45^\circ$, 40 PPI)

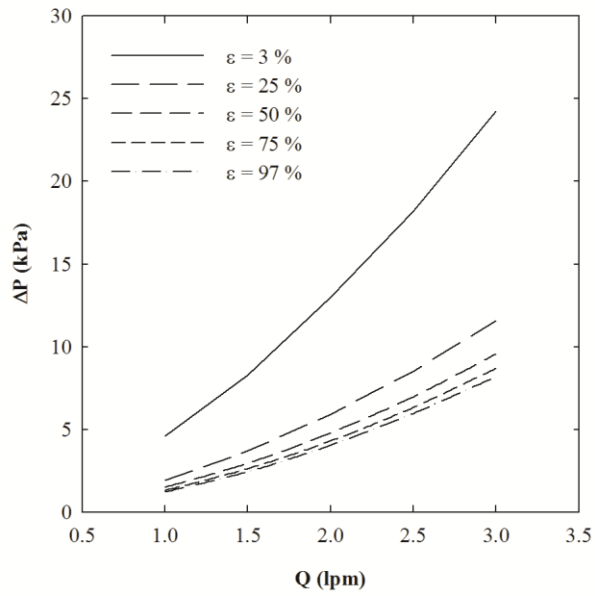


Figure 6.13. Pressure Drop as a Function of Flow Rate and Porosity ($\theta = 45^\circ$, 20 PPI)

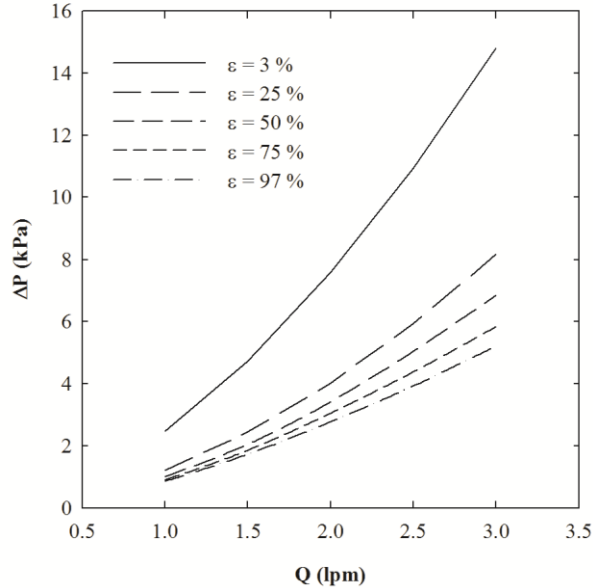


Figure 6.14. Pressure Drop as a Function of Flow Rate and Porosity ($\theta = 45^\circ$, 10 PPI)

The bifurcation angles have a large impact on fluid transport through the tree-like flow networks in the porous disks at relatively low porosities. As previously mentioned, at a porosity of 97 % the fluid has passed through the porous disk before the flow reaches the $k = 1$ branch level, regardless of bifurcation angle. At a porosity of 3 % however, the amount of fluid that reaches the $k = 3$ branch level before passing through the porous disk increases as the bifurcation angle decreases. This, along with a decrease in surface area, results in the pressure drop across the porous disk decreasing with bifurcation angle. This phenomenon can be seen when comparing the fluid pressure and velocity magnitude isolines for the porous tree-like disks with bifurcation angles of 15° and 90° as seen in Figures 6.15 and 6.16. The fluid pressure and velocity isolines are shown on a plane located at the bottom of the channel walls on the inlet side of the porous disks. As can be seen in Figure 6.16, the fluid velocity magnitudes are concentrated at the $k = 0$ and 1 branch levels for the porous disk with 90° bifurcations while the fluid velocity magnitudes are more uniformly distributed across all branch levels for the porous disk with 15°

bifurcations. This means that more fluid is travelling through the entire tree-like flow networks at relatively lower bifurcation angles before passing through the porous disk. It should be noted that due to the definition of the bifurcation angles in Figure 6.1 four exit plenums, located where $k = 3a$ and $3h$, are shared for the 90° tree-like disk. Only the 90° tree-like porous disk has space filling flow passages. A 15° tree-like porous disk that is space filling would have 12 branches emanating from the inlet plenum as opposed to 4 as is the case with the 90° tree-like porous disk. An increase in the number of tree-like networks emanating from the inlet plenum would result in an increase in surface area which would be advantageous if the porous tree-like disks were utilized to increase heat transfer. This was not studied as it would prevent a direct comparison of the effect of bifurcation angle on pressure drop.

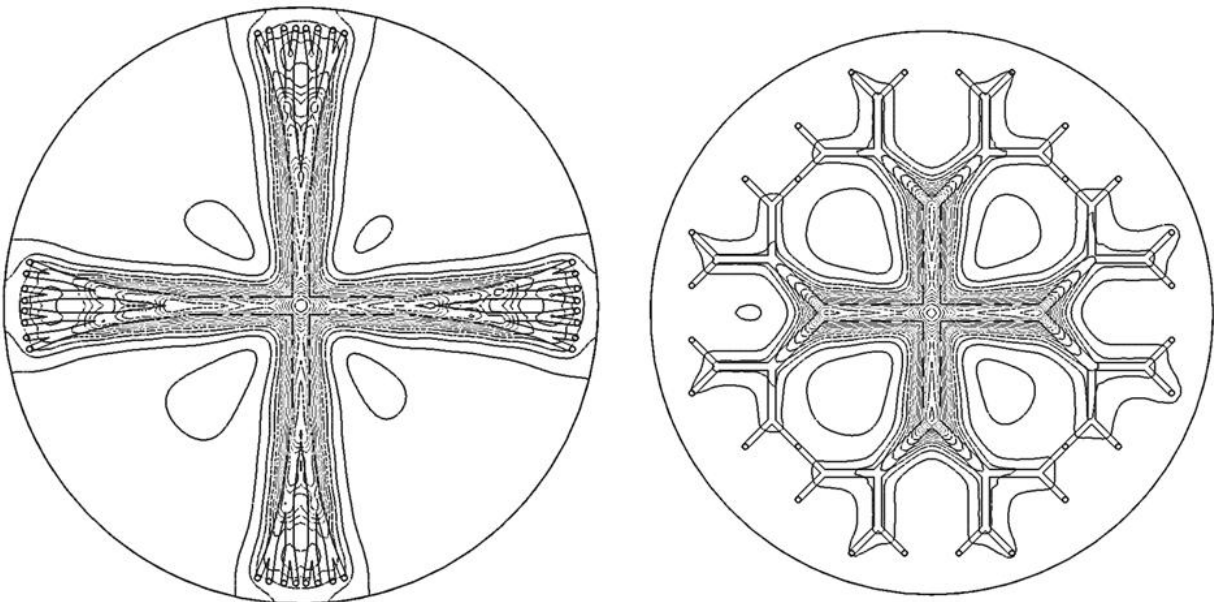


Figure 6.15. Fluid Pressure Isolines for the 15 (left) and 90 (right) $^\circ$ Porous Disks ($\epsilon = 0.03$, 40 PPI, $Q = 3$ lpm)

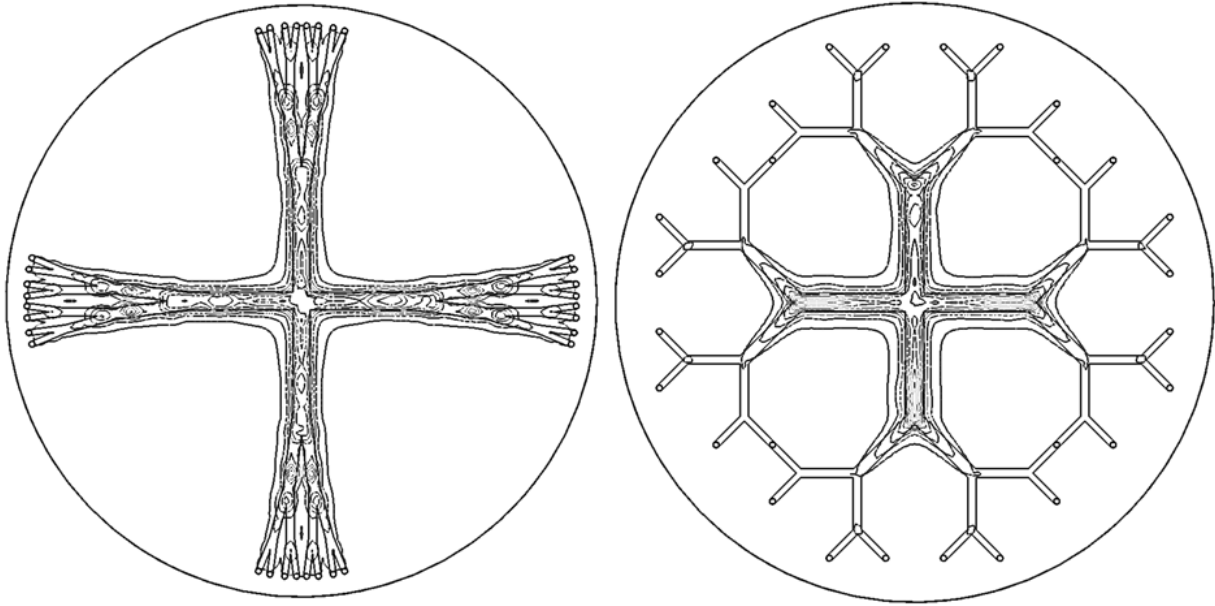


Figure 6.16. Fluid Pressure Isolines for the 15 (left) and 90 (right) ° Porous Disks ($\epsilon = 0.03$, 40 PPI, $Q = 3$ lpm)

Conclusion

A computational model has been developed to study the effects of porosity, pore size, and bifurcation angle on the pressure drop across and the flow behavior inside a porous disk with hierarchical bifurcating flow passages. A porous disk, with third-order branch level channel widths on the verge of microscale, was created to observe these effects. The effect of bifurcation angle on pressure drop was found to be highly dependent on porosity and pore size. As the porosity of the disks decreased the effect of bifurcation angle on pressure drop increased. Similarly, as the porosity decreased the pressure drop increased, regardless of bifurcation angle. The pressure drop increased, regardless of bifurcation angle, as the number of pores per inch increased. The bifurcation angles had the greatest impact on pressure drop at low porosities and small pore sizes. Tree-like flow passages thus only influence the flow through porous disks at relatively lower bifurcation angles and porosities. The amount of fluid that travels through the tree-like networks before passing through the porous disks is highly dependent on bifurcation

angle. Similarly, very little fluid travels through the entire tree-like flow networks before passing through the porous disks at high porosities and large pore sizes.

Acknowledgements

Portions of this work were funded by The University of Alabama GK-12 Program. The GK-12 Program is supported by the National Science Foundation under grant 0742504.

References

- [6.1] Tuckerman, B. B., and Pease, R. F. W., 1981, "High-Performance Heat Sinking for VLSI," *IEEE Electron Device Letters*, 2(5), pp. 126-129.
- [6.2] West, G. B., Brown, J. H., and Enquist, B. J., 1997, "A General Model for the Origin of Allometric Scaling Laws in Biology," *Science*, 276, pp. 122-126.
- [6.3] West, G. B., Brown, J. H., and Enquist, B. J., 1999, "The Fourth Dimension of Life: Fractal Geometry and Allometric Scaling of Organisms," *Science*, 284, pp. 1677-1679.
- [6.4] West, G. B., 1999, "The Origin of Universal Scaling Laws in Biology," *Physica A*, 263, pp. 104-113.
- [6.5] Bejan, A., 2000, *Shape and Structure, From Engineering to Nature*, Cambridge, Cambridge University Press.
- [6.6] Bejan, A., 1997, "Constructal-Theory Network of Conducting Paths for Cooling a Heat Generating Volume," *International Journal of Heat and Mass Transfer*, 40(4), pp. 799-816.
- [6.7] Bejan, A., and Lorente, S., 2010, "The Constructal Law of Design and Evolution in Nature," *Philosophical Transactions of the Royal Society B*, 35(1545), pp. 1335-1347.
- [6.8] Bejan, A., and Lorente, S., 2006, "Constructal Theory of Generation of Configuration in Nature and Engineering," *Journal of Applied Physics*, 100(4).
- [6.9] Bejan, A., and Errera, M. R., 2000, "Convective Trees of Fluid Channels for Volumetric Cooling," *International Journal of Heat and Mass Transfer*, 43, pp. 3105-3118.
- [6.10] Calamas, D., and Baker, J., 2013, "Tree-Like Branching Fins: Performance and Natural Convective Heat Transfer Behavior," *International Journal of Heat and Mass Transfer*, Accepted for Publication.
- [6.11] Calamas, D., and Baker, J., 2013, "Behavior of Thermally Radiating Tree-Like Fins," *Journal of Heat Transfer*, Accepted for Publication.
- [6.12] Murray, C. D., 1926, "The Physiological Principle of Minimum Work. I. The Vascular System and the Cost of Blood Volume," *Journal of Physiology*, 12(3), pp. 207-214.
- [6.13] Pence, D. V., 2002, "Reduced Pumping Power and Wall Temperature in Microchannel Heat Sinks with Fractal-Like Branching Channel Networks," *Microscale Thermophysical Engineering*, 6, pp. 319-330.

- [6.14] Pence, D. V., 2000, "Improved Thermal Efficiency and Temperature Uniformity Using Fractal-Like Branching Channel Networks," Proc. International Conference on Heat Transfer and Transport Phenomena in Microscale, New York, pp. 142-148.
- [6.15] Alharbi, A. Y., Pence, D. V., and Cullion, R. N., 2004, "Fluid Flow through Microscale Fractal-Like Branching Channel Networks," Journal of Fluids Engineering, 125(6), pp. 1051-1057.
- [6.16] Alharbi, A. Y., Pence, D. V., and Cullion, R. N., 2004, "Thermal Characteristics of Microscale Fractal-Like Branching Channels," Journal of Heat Transfer, 126(5), pp. 744-755.
- [6.17] Calamas, D., and Baker, J., 2013, "Performance of a Biologically-Inspired Heat Exchanger with Hierarchical Bifurcating Flow Passages," Journal of Thermophysics and Heat Transfer, 27(80-90).
- [6.18] Wang, X. Q., Mujumdar, A. S., and Yap, C., 2006, "Thermal Characteristics of Tree-Shaped Microchannel Nets for Cooling of a Rectangular Heat Sink," International Journal of Thermal Sciences, 45(11), pp. 1103-1112.
- [6.19] Wang, X. Q., Mujumdar, A. S., and Yap, C., 2006, "Numerical Analysis of Blockage and Optimization of Heat Transfer Performance of Fractal-Like Microchannel Nets," Journal of Electronic Packaging, 128(1), pp. 38-45.
- [6.20] Chen, Y., and Cheng, P., 2002, "Heat Transfer and Pressure Drop in Fractal Tree-Like Microchannel Nets," International Journal of Heat and Mass Transfer, 45(13), pp. 2643-2648.
- [6.21] Chen, Y., and Cheng, P., 2005, "An Experimental Investigation on the Thermal Efficiency of Fractal Tree-Like Microchannel Nets," International Communications in Heat and Mass Transfer, 32(7), pp. 931-938.
- [6.22] Senn, S. M., and Poulikakos, D., 2004, "Laminar Mixing, Heat Transfer and Pressure Drop in Tree-Like Microchannel Nets and Their Application for Thermal Management in Polymer Electrolyte Fuel Cells," Journal of Power Sources, 130(1-2), pp. 178-191.
- [6.23] Wang, X. Q., Mujumdar, A. S., and Yap, C., 2007, "Effect of Bifurcation Angle in Tree-Shaped Microchannel Networks," Journal of Applied Physics, 102(7).
- [6.24] Allouache, N., Chikh, S., 2004, "Entropy Generation in a Partly Porous Heat Exchanger," Computer Aided Chemical Engineering, 18, pp. 139-144.
- [6.25] Al-Salem, K., Oztop, H. F., and Kiwan, S., 2011, "Effects of Porosity and Thickness of Porous Sheets on Heat Transfer Enhancement in a Cross Flow Over Heat Cylinder," International Communications in Heat and Mass Transfer, 38, pp. 1279-1282.

- [6.26] Lan, X. K., and Khodadadi, J. M., 1993, "Fluid Flow and Heat Transfer through a Porous Medium Channel with Permeable Walls," *International Journal of Heat and Mass Transfer*, 36(8), pp. 2242-2245.
- [6.27] Mohamad, A. A., 2003, "Heat Transfer Enhancements in Heat Exchangers Fitted with Porous Media Part I: Constant Wall Temperature," *International Journal of Thermal Sciences*, 42, pp. 385-395.
- [6.28] Narasimhan, A., Raju, K. S., 2007, "Effect of Variable Permeability Porous Medium Inter-Connectors on the Thermo-Hydraulics of Heat Exchanger Modeled as Porous Media," *International Journal of Heat and Mass Transfer*, 50, pp. 4052-4062.
- [6.29] Odabae, M., and Hooman, K., 2012, "Metal Foam Heat Exchangers for Heat Transfer Augmentation from a Tube Bank," *Applied Thermal Engineering*, 36, pp. 456-463.
- [6.30] Pavel, B. I., and Mohamad, A. A., 2004, "An Experimental and Numerical Study on Heat Transfer Enhancement for Gas Heat Exchangers Fitted with Porous Media," *International Journal of Heat and Mass Transfer*, 47, pp. 4939-4952.
- [6.31] Targui, N., and Kahalerras, H., 2008, "Analysis of Fluid Flow and Heat Transfer in a Double Pipe Heat Exchanger with Porous Structures," *Energy Conversion and Management*, 49, pp. 3217-3229.
- [6.32] Yang, Y., and Hwang, M., 2009, "Numerical Simulation of Turbulent Fluid Flow and Heat Transfer Characteristics in Heat Exchangers Fitted with Porous Media," *International Journal of Heat and Mass Transfer*, 52, pp. 2956-2965.
- [6.33] Zhao, T. S., and Song, Y. J., 2001, "Forced Convection in a Porous Medium Heated by a Permeable Wall Perpendicular to Flow Direction: Analyses and Measurements," *International Journal of Heat and Mass Transfer*, 44, pp. 1031-1037.
- [6.34] R. C. Reid, J. M. Prausnitz, B. E., Poling, 1987, *The Properties of Gases and Liquids*, 2nd ed., McGraw-Hill, New York.
- [6.35] Launder, B. E., and Sharma, B. I., "Application of the Energy Dissipation Model of Turbulence to the Calculation of Flow Near a Spinning Disc," *Letters in Heat and Mass Transfer*, 1(1), pp. 131-138.
- [6.36] von Karman, T., 1930, "Mechanische Ahnlichkeit und Turbulenz," *Nachrichten von der Gesellschaft der Wissenschaften zu Gottingen*, 5, pp. 58-76.
- [6.37] R. Glowinski, P. Le Tallec, 1989, *Augmented Lagrangian Methods and Operator-Splitting Methods in Nonlinear Mechanics*, SIAM, Philadelphia.

- [6.38] G. I. Marchuk, 1982, *Methods of Numerical Mathematics*, Springer-Verlag, Berlin.
- [6.39] A. A. Samarskii, 1989, *Theory of Difference Schemes*, Nauka, Moscow.
- [6.40] P. J., Roach, 1998, *Technical Reference of Computational Fluid Dynamics*, Hermosa Publishers, Albuquerque.
- [6.41] C. Hirsch, 1998, *Numerical Computation of Internal and External Flows*, John Wiley and Sons, Chichester.
- [6.42] S. V. Patankar, 1980, *Numerical Heat Transfer and Fluid Flow*, Hemisphere, Washington D.C.
- [6.43] Calamas, D., and Baker, J., 2013, "Performance Characteristics of a Biologically-Inspired Solid-Liquid Heat Exchanger," *Experimental Heat Transfer*, Submitted for Publication.
- [6.44] Dukhan, N., and Patel, P., 2008, "Equivalent Particle Diameter and Length Scale for Pressure Drop in Porous Metals," *Experimental Thermal and Fluid Science*, 32, pp. 1059-1067.

CHAPTER 7

CONCLUSION

For the first investigation, a computational model was developed to study the effects of scaling on a microscale tree-like flow network's fluid flow and heat transfer characteristics. A mesoscale model, with fourth-order branch channel widths on the order of microscale, was created to observe these effects. Results were cast in terms of commonly defined dimensionless parameters that allow the branching flow networks to be compared to traditional compact heat exchangers. Mesoscale tree-like flow networks exhibit qualitatively similar centerline pressure and wall temperature distributions as microscale tree-like flow networks under the conditions studied. While the microscale flow network had two orders of magnitude greater local pressure recovery at bifurcations the benefit of local pressure recovery at bifurcations is still present in the mesoscale flow network. The microscale flow network studied had a total pressure drop two orders of magnitude greater than the mesoscale flow network. Bifurcation angles, at all scales, have a significant impact on local pressure recovery and wall temperature distributions due to flow separation and zones of recirculation. Wall temperature uniformity can be increased by minimizing flow separation that results in hot spots at walls immediately downstream of bifurcations. Flow separation results in outer walls with higher maximum wall temperatures when compared with inner walls. The microscale and mesoscale flow networks exhibit similar thermal performance at all branch levels. The mesoscale flow network had an order of magnitude larger increase in bulk fluid temperature across the flow network. Knowledge obtained when

studying microscale tree-like flow networks can be utilized in the design of mesoscale tree-like flow networks.

For the second investigation, a validated and verified computational model was developed to study the effects of fin geometry on fin effectiveness, efficiency and base temperature of thermally radiating tree-like fins. The tree-like fins were found to be more effective than rectangular fins of equal mass, base area, and volume. Fin effectiveness was found to increase for the tree-like fins with bifurcation angle due to increased surface area and decreased projected areas between branches for thermal radiation interactions. Fin effectiveness per unit mass was found to be highly dependent on material density and less dependent on material thermal conductivity. For example, while the silver and copper fins had the highest effectiveness the aluminum fin had the greatest effectiveness on a per unit mass basis. Fin effectiveness was found to be highest for fins with the largest width-to-thickness ratios as fin effectiveness is a function of base area. The thinner fins also result in decreased projected areas between branches and consequently less thermal radiation interaction. The tree-like fins were found to be more efficient than rectangular fins of equal mass, base area, and volume for heat rates of 5, 10, 15, 20, and 25 W and less efficient for an applied heat rate of 1 W. Fin efficiency was found to increase for the tree-like fins with bifurcation angle as fin temperature uniformity increased. Fin efficiency was found to be highest for materials with relatively higher thermal conductivities. Fin efficiency was found to be highest for fins with the smallest width-to-thickness ratios as fin efficiency is a function of surface area. The tree-like fins were found to have lower base temperatures than rectangular fins of equal mass, base area, and volume. Fin base temperatures were found to decrease with increasing bifurcation angle. Materials with relatively higher thermal conductivities had lower base temperatures. Fins with larger width-to-

thickness ratios were found to have high base temperatures due to decreased base surface areas. A correlation for the effectiveness of the tree-like fins was also developed which incorporated the various parameters investigated. The correlation had an average error of 1.50 %. The thermal performance of the tree-like fins was found to be greater than that of the rectangular fins as they were found to be more effective, efficient and had lower base temperatures under the conditions studied.

For the third investigation, a validated and verified computational model was developed to study the effects of fin geometry and scaling on fin effectiveness, efficiency and base temperature for tree-like fins in a naturally convecting environment. The tree-like fins were found to be more effective than rectangular fins of equal mass, base area, and volume. Fin effectiveness was found to increase for the tree-like fins with bifurcation angle due to increased surface area. Fin effectiveness per unit mass was found to be highly dependent on material density and less dependent on material thermal conductivity. Fin effectiveness was found to be highest for fins with the largest width-to-thickness ratios as fin effectiveness is a function of base area. The microscale tree-like fin was more effective than the mesoscale and macroscale tree-like fins. Fin efficiency was found to decrease for the tree-like fins with bifurcation angle. Fin efficiency was found to be highest for materials with relatively higher thermal conductivities. Fin efficiency was found to be highest for fins with the smallest width-to-thickness ratios as fin efficiency is a function of surface area. As with fin effectiveness, the microscale tree-like fin had the highest fin efficiency. The tree-like fins were found to have lower base temperatures than rectangular fins of equal mass, base area, and volume. Fin base temperatures were found to decrease with increasing bifurcation angle. Materials with relatively higher thermal conductivities had lower base temperatures. Fins with larger width-to-thickness ratios were

found to have lower base temperatures. The microscale tree-like fin had lower base temperatures when compared with the mesoscale and macroscale tree-like fins. A correlation for the effectiveness of the tree-like fins developed which incorporated the various parameters investigated. The correlation had an average error of 1.02 %. The tree-like fins were found to offer greater thermal performance when compared with the rectangular fins of equal base area, mass, and volume as they were more effective at dissipating heat and had lower base temperatures.

For a fourth investigation, the system performance of a biologically-inspired single fluid compact heat exchanger was experimentally examined. Results were cast in terms of commonly defined dimensionless parameters that allow the single fluid compact heat exchanger with tree-like flow passages to be compared to traditional two fluid compact heat exchangers. The pressure drop across the heat exchanger was found to increase with the flow rate while pressure forces dominate inertial forces at low Reynolds numbers. The temperature increase across the heat exchanger was found to decrease with increasing flow rate while convection heat transfer was found to dominate conduction heat transfer as the Reynolds number increases. As the Reynolds number decreases the ratio of the heat transferred to the fluid to the heat exported by the fluid decreases. As the Reynolds number, and thus the flow-stream mass velocity, increases the friction factor decreases. Correlations for the Euler number, Colburn factor, and friction factor as a function of the Reynolds number were developed and found to have the functional form of a power law while the Nusselt number was found to be a linear function of the Reynolds number.

For the final investigation, a computational model was developed to study the effects of porosity, pore size, and bifurcation angle on the pressure drop across and the flow behavior inside a porous disk with hierarchical bifurcating flow passages. A porous disk, with third-order

branch level channel widths on the verge of microscale, was created to observe these effects. The effect of bifurcation angle on pressure drop was found to be highly dependent on porosity and pore size. As the porosity of the disks decreased the effect of bifurcation angle on pressure drop increased. Similarly, as the porosity decreased the pressure drop increased, regardless of bifurcation angle. The pressure drop increased, regardless of bifurcation angle, as the number of pores per inch increased. The bifurcation angles had the greatest impact on pressure drop at low porosities and small pore sizes. Tree-like flow passages thus only influence the flow through porous disks at relatively lower bifurcation angles and porosities. The amount of fluid that travels through the tree-like networks before passing through the porous disks is highly dependent on bifurcation angle. Similarly, very little fluid travels through the entire tree-like flow networks before passing through the porous disks at high porosities and large pore sizes.